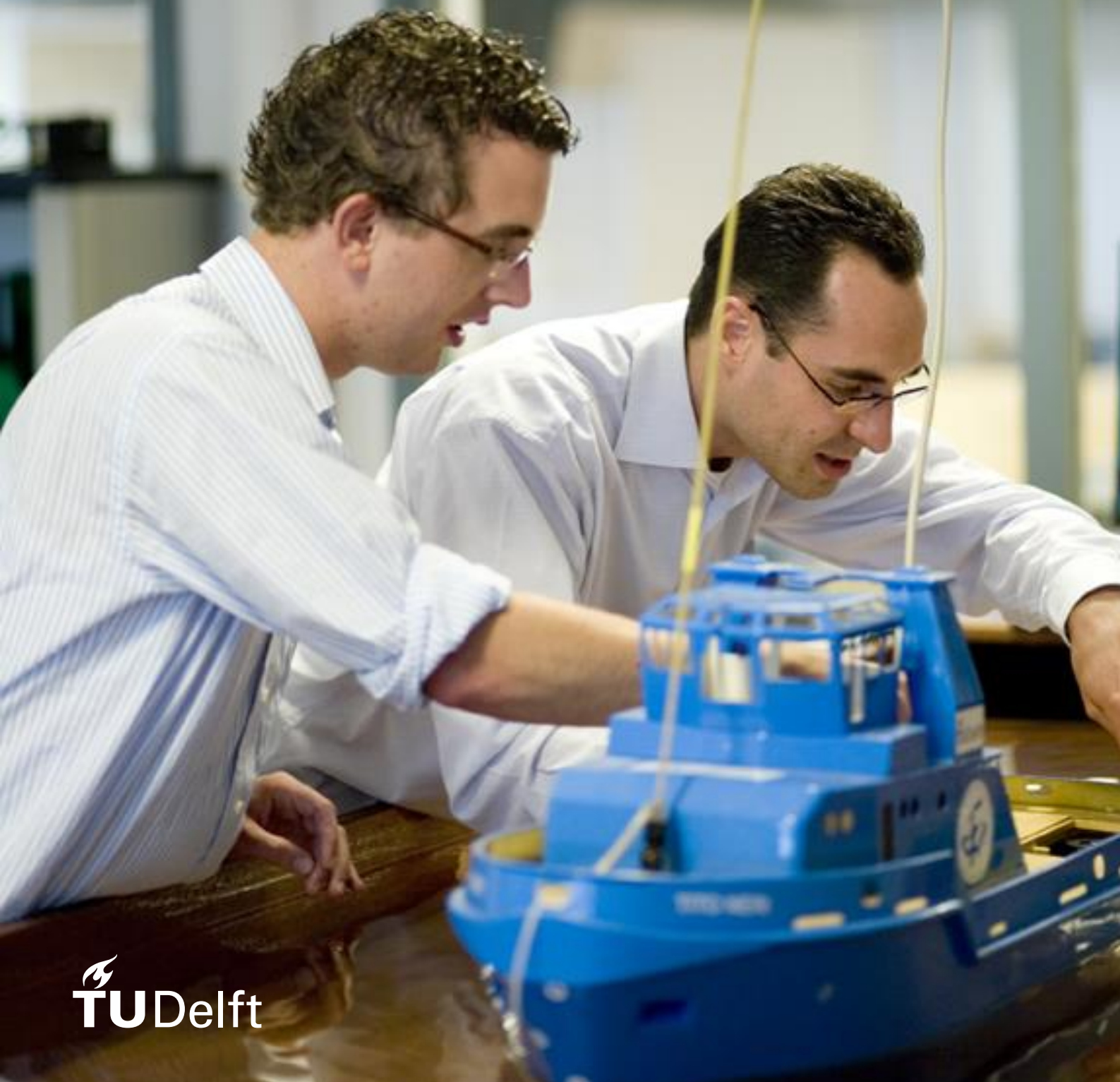


Ahmed H. Al Ayesh

Optimal SAG Design in Heterogeneous Reservoirs

Effect of Permeability on Foam Diversion



Optimal SAG Design in Heterogeneous Reservoirs

Effect of Permeability on Foam Diversion

By

Ahmed Hussain Al Ayesh

in partial fulfilment of the requirements for the degree of

Master of Science
in Applied Earth Sciences
Petroleum Engineering and Geosciences

at the Delft University of Technology,
to be defended publicly on Monday January 25, 2016 at 14:30 P.M.

Supervisor:	Prof. dr. W. R. (William) Rossen	
Thesis committee:	Dr. P.J. (Philip) Vardon,	TU Delft
	R. (Rodrigo) Salazar, MSc.	TU Delft.
	J.M. (Jakolien) van der Meer, MSc.	TU Delft

An electronic version of this thesis is available at <http://repository.tudelft.nl/>.

Preface

Many questions regarding fundamentals of foam behaviour are still open in physics, mathematics, and chemistry. Seeking knowledge in this multidisciplinary subject is both thrilling and fascinating. I was lucky to work with one of the leaders in academia in the area of foam enhanced oil recovery (EOR). My interest grew as I discovered the potential of foam applications in the oil industry. I hope you find this read interesting.

*Ahmed Al Ayesh
Delft, January 2016*

Contents

Abstract	9
Acknowledgements	9
1 Introduction & Problem Statement	11
1.1. Introduction	11
1.2. Problem Statement	14
2 Methodology	15
2.1. Introduction	15
2.2. Geometry of Flow	15
2.3. Darcy's Law	16
2.3.1. Darcy's Law for Single-Phase	16
2.3.1. Darcy's Law for Multiphase Flow	17
2.4. Corey Relative Permeabilities	17
2.5. Mobility	18
2.6. Pressure Difference	19
2.6.1. Pressure Difference for Single-Phase Flow	19
2.6.2. Pressure Difference for Multiphase Flow	19
2.7. Fractional-Flow Theory	20
2.7.1. Introduction and Assumptions	20
2.7.2. Water Fractional-Flow Notation	20
2.7.3. Mass Balance	20
2.7.4. Dimensionless Parameters	21
2.7.4.1. Dimensionless Position	21
2.7.4.2. Dimensionless Time	22
2.7.4.3. Dimensionless Pressure	22
2.7.5. FFT in Dimensionless Notations	22
2.8. Solution Method	23
2.8.1. For Gas Injection in a Single-Layer Reservoir	23
2.8.2. For Gas Injection in a Multi-Layer Reservoir	25
2.8.2.1. Relative Time Derivation	27
2.8.3. For SAG Using Single Surfactant-Slug	28
2.8.4. Modification of F_w by Namdar Zanganeh et al.	30
2.8.5. For SAG Using Different Surfactant Slug Sizes	30
2.9. Pseudo Algorithm	32
2.10. Validity of the Model	37
3 Results	39
I. Base Case: Gas Injection without Surfactant	40
II. Surfactant-Saturated Reservoir (A.STARS Model)	41
II. Surfactant-Saturated Reservoir (B. Namdar Zanganeh et al. Modified Model)	42
III. Discrete Surfactant Slug Sizes (A. STARS Model)	43
III. Discrete Surfactant Slug Sizes (B. Namdar Zanganeh et al. Modified Model)	49
IV. No Surfactant Injection into Bandera Gray (A. Other Layers are Surfactant-Saturated i. STARS Model)	55
IV. No Surfactant Injection into Bandera Gray (A. Other Layers are Surfactant-Saturated ii. Namdar Zanganeh et al. Modified Model)	56
IV. No Surfactant Injection into Bandera Gray (B. Discrete Surfactant Slugs ii. STARS Model)	57
IV. No Surfactant Injection into Bandera Gray (B. Discrete Surfactant Slugs ii. Namdar Zanganeh et al. Modified Model)	63

4 Discussion	69
5 Conclusion and Recommendations	73
5.1. Conclusion	73
5.2. Recommendations	73
Nomenclature	74
Bibliography.....	75
Appendix A: Tables	80
Appendix B: Diagrams.....	83
Appendix C: Matlab Code	92

Abstract

Foam can divert flow from higher- to lower-permeability layers and thereby improve vertical sweep efficiency in gas-injection enhanced oil recovery. Recently, Kapetas et al. (2015) measured foam properties in cores from four sandstone formations ranging in permeability from 6 to 1900 md, and presented parameter values for a foam-model fit to those data. Permeability affects the limiting capillary pressure at which foam collapses in the "high-quality regime". Kapetas et al. showed how foam would divert injection between layers of these formations if all layers were full of foam at a given quality (gas fractional flow). Here we examine the effects of SAG (surfactant-alternating-gas) injection method on diversion in a dynamic foam process using fractional-flow modelling and the model parameters derived by Kapetas et al. We consider a hypothetical reservoir containing non-communicating layers with the properties of the four formations in that study.

The effectiveness of diversion varies greatly with injection method. In a SAG process, diversion of the first slug of gas depends on foam behaviour at high foam quality. Foam mobility in the foam bank during gas injection depends on the nature of a shock front that bypasses most foam qualities usually studied in the laboratory. The foam with the lowest mobility at fixed foam quality does not necessarily give the lowest mobility in a SAG process. In particular, diversion depends on how and whether foam collapses at low water saturation; this property varies greatly among the foams reported by Kapetas et al. Moreover, diversion depends on the size of the surfactant slug received by each layer before gas injection. This of course favours diversion away from high-permeability layers that receive a large surfactant slug, but there is an optimum surfactant slug size: too little surfactant and diversion from high-permeability layers is not effective; too much and mobility is reduced in low-permeability layers, too. Using a model based directly on laboratory data, this study shows how diversion between layers differs with injection method.

Acknowledgements

I would like to express my sincere gratitude for professor Rossen. He was always a source of wisdom and guidance throughout this journey. I would also like to thank Dr. Eftekhari for the various discussions we had in regard to modelling foam flow. His knowledge and support highly improved the quality of this work. I would also like to extend my thanks to Rodrigo Salazar, Dr. Sian Jones, Dr. Sébastien Vincent-Bonnieu, and the entire foam research group for their contributions and countless discussions. I would also like to thank my wife, parents and siblings for providing me with the motivation needed to complete my studies and earn my degree. Thank you all.

1 Introduction & Problem Statement

1.1. Introduction

Foam as technique for gas diversion has been proven useful in several enhanced oil recovery (EOR) practices (Rossen and Wang, 1999; Cheng et al., 2001). There are many economic and technical challenges in gas flooding EOR processes. Economic challenges mainly include matching an affordable, convenient source of gas with a viable candidate field. Although gas can displace oil efficiently wherever it sweeps (good micro displacement), many technical challenges arise due to its poor volumetric sweep efficiency caused by reservoir heterogeneities, viscous instabilities, and gravity override (Lake et al., 2014). Foam can tackle the technical challenges in order to improve sweep efficiency by reducing gas mobility (Schramm, 1994; Kovsky and Radke, 1994; Rossen, 1996). The variation of permeabilities in layered reservoirs causes the displacing fluid to advance faster in zones of higher permeability, resulting in an earlier breakthrough into those layers. Once preferential paths have formed, little sweep improvement is expected in an immiscible displacement. In this paper, we show that SAG is superior to preformed foam injection in minimizing the effect of reservoir heterogeneity in terms of permeability contrast in non-communicating layered reservoirs (i.e. better diversion).

Foam is a dispersion of gas bubbles in a continuous liquid medium where bubbles are separated by thin films called lamellae. Foam dramatically reduces the mobility of the gas phase. Foam quality is the gas volume percentage at a specified pressure and temperature. In the absence of oil, steady-state strong foam exists in two flow regimes: low-quality and high-quality (Osterloh and Jante, 1992; Alvarez and Rossen, 2001). In the low-quality regime, foam has relatively fixed bubble size and is strongly shear-thinning; as foam quality f_g increases, foam mobility decreases, because the more viscous gas occupies a larger fraction of total flow, up to the transition foam quality f_g^* . The transition marks the start of the high quality regime that describes the effect of foam coalescence at the limiting capillary pressure, P_c^* that corresponds to the limiting water saturation, S_w^* , as foam quality increases (Khatib et al., 1988, Zhou et al., 1995). The limiting capillary pressure is a function of surfactant formulation and concentration, gas velocity, permeability of the porous medium, and presence of oil (Khatib et al., 1988). In the high-quality regime, foam can be moderately shear-thinning, shear-thickening, or Newtonian (Hirasaki and Lawson, 1985; Falls et al., 1989; Alvarez et al., 2001; Xu and Rossen, 2003; Tang and Kovsky, 2006). Foams tend to promote larger mobility reductions in high-permeability porous media, as compared to lower-permeability porous media, mainly due to foam's sensitivity to capillary pressure (Khatib et al., 1988). The higher capillary pressure in low-permeability layers tends to destabilize foam and slow its generation.

There are two common approaches for modelling foam flow in porous media: population balance (PB) (mechanistic) models and implicit-texture (IT) (empirical) models (sometimes called local-equilibrium (LE) models). The local equilibrium models assume that foam processes occur very quickly compared to the timescale of the overall displacement. The two types of models represent the reduction of gas mobility due to the presence of foam differently. PB models reduce gas mobility based on the evolution of foam texture (i.e. bubble size, number of lamella, etc.). The model takes into account the dynamic processes involved such as lamella generation and destruction (Falls et al., 1988; Patzek, 1988; Kovsky et al., 1995; Kovsky et al., 1995; Bertin, 2000; Zitha, 2006; Kam et al., 2007; Chen et al., 2010). The model might seem complete in theory, but the main challenge is obtaining the parameters needed. The IT approach represents the effect of

foam implicitly through gas mobility-reduction factor that is a function of saturations, superficial velocities, etc. (Law et al., 1989; Patzek and Myhill, 1989; Kular et al., 1989; Fisher et al., 1990; Islam and Farouq-Ali, 1990; Mohammadi and Coombe, 1992; Cheng et al., 2000). In principle, the IT models are simpler and can fit steady-state data. Furthermore, the two models are generally in good agreement (Kam et al., 2007; Chen et al., 2010) even in fitting dynamic foam displacements except in at the entrance region of a porous medium and any shock fronts (Ettinger and Radke, 1992; Chen et al., 2010; Ashoori et al., 2011). More details about the different approaches used to model foam flow in porous media could be found in a recent review by Ma et al. (2015).

A widely used application of the IT model is the STARS model (CMG, 2012). The model can fit both steady-state strong foam regimes using parameters such as $fmmob$, $fmdry$, $epdry$, $epcap$ (Alvarez and Rossen, 2001). $fmmob$ is the reference mobility reduction factor, i.e., the maximum reduction in gas mobility at full foam strength. $fmdry$ represents water saturation around which foam weakens or collapses, i.e. S_w^* . $epdry$ governs how abruptly foam collapses in vicinity of $S_w = fmdry$. $epcap$ governs non-Newtonian behaviour in the low-quality regime. However, the model does not represent non-Newtonian behaviour in the high-quality regime. Additionally, despite the high capillary pressure at residual water saturation (S_{wr}), the STARS model does not allow for complete foam collapse at $S_w=S_{wr}$. Therefore, Namdar Zanaganeh et al. (2011) proposed a simple modification to the STARS model to allow for complete foam collapse at S_{wr} .

There are three different methods for foam injection that are used depending on the intended purpose:

- Sequential injection: alternating slugs of surfactant and gas, commonly known as SAG, (Kibodeaux and Rossen, 1997).
- Co-injection: co-injection of surfactant solution with gas (Stone, 2004; Rossen et al., 2010).
- Dissolved surfactants injected with supercritical CO₂. The foam forms as the CO₂ meets formation water (Le et al., 2008; Ashoori et al., 2010).

However, due to the substantial effective viscosities of preformed foams and the associated poor injectivity, and corrosion issues, SAG is preferred in field applications.

Recently, Kapetas et al. (2015) fitted the STARS foam model parameters to measured data for pressure gradient (∇P) vs. foam quality for cores from four sandstone formations ranging in permeability from 6 to 1900 md using the least-squares method of Eftekhari as shown in **Figure 150**. The least-square method is summarized in Farajzadeh et al. (2015). The formations are Bentheimer, Berea, Sister Berea, and Bandera Gray with permeabilities of 1900, 90, 160, and 6 md respectively. They also fitted the water and gas relative permeabilities to measured lab data using Corey parameters. The parameters for the foam model and Corey relative permeabilities can be found in **Table 1** and **Table 2** in Appendix A. In their paper, Kapetas et al. (2015) represented hypothetical scenarios for foam diversion at different qualities f_g into three non-communicating layers as shown in **Figure 1**. It should be noted that the y-axis is logarithmic, because superficial velocities in the different layers vary greatly in magnitude. Also, the diversion behaviour varies significantly for different pressure gradients due to the difference in the extent of shear-thinning behaviour among the three formations. The graph shows that in all cases (varying ∇P & f_g), foam flows at larger velocity in the highest-permeability layer (Bentheimer) with varying degrees of diversion. The highest diversion occurs when foam reaches its strongest condition at a critical foam quality of $f_g^*=95\%$ in the Bentheimer layer.

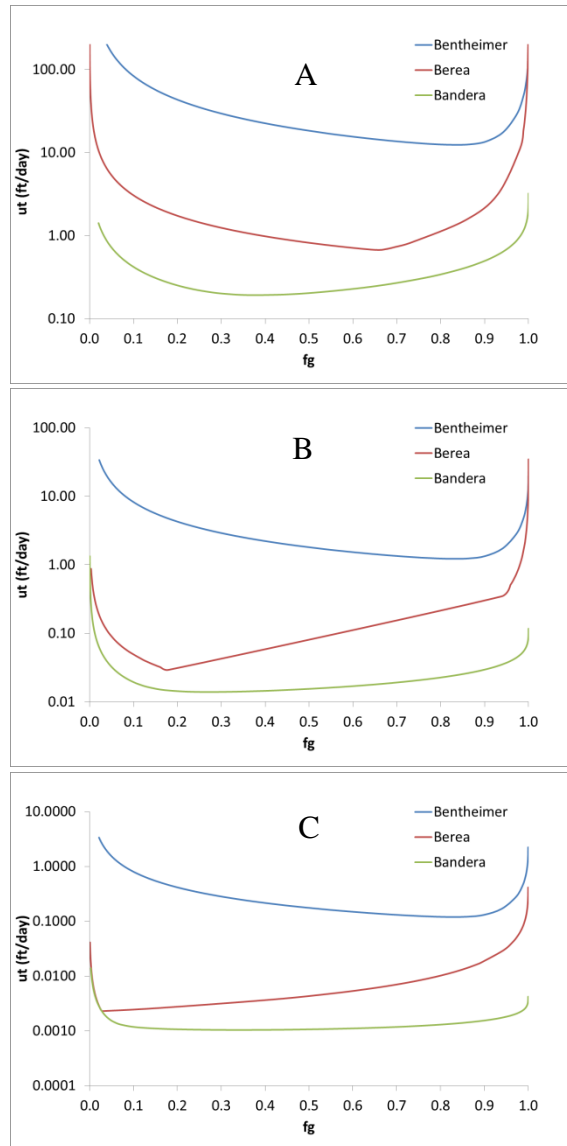


Figure 1: Total Superficial Velocity at Different Foam Qualities for Bentheimer, Berea and Bandera Gray for Pressure Gradients of (A) 400 bar/m, (B) 40 bar/m and (C) 4 bar/m.

In this paper, we evaluate the magnitude of diversion using the SAG injection scheme. Fractional-flow theory is used to predict SAG performance. Details about the method can be found in Chapter 2. The low-quality regime is not experienced during SAG injection, and since shear-thinning is mainly important in describing the low-quality regime, it is ignored in this paper.

In order to predict injectivity in a SAG process, it is crucial to predict mobilities near the injection wellbore (Kibodeaux and Rossen, 1997; Leefink et al, 2013; Rossen and Boeije, 2015). The mobilities near the wellbore are highly influenced by whether foam completely collapses at high capillary pressures near the wellbore (Namdar Zanaganeh et al., 2011; Rossen and Boeije, 2015). Even though mobility is low at the front of the foam bank, fractional-flow theory predicts that the mobility near the wellbore is high during gas injection, allowing for both mobility control at the flood front and good injectivity (Leefink et al, 2013; Rossen and Boeije, 2015). In idealized circumstances, a single-slug SAG process is predicted to have the best performance since it improves injectivity and minimizes the effects of gravity override (Shan and Rossen, 2004; Faisal et al., 2009; Kloet et al., 2009; Boeije and Rossen, 2014).

In this paper, the model fits of Kapetas et al. (2015) for foam without oil are used to illustrate the diversion of gas in a single-slug SAG process in a hypothetical four-layer reservoir with equal pore volume in each

layer. A one-dimensional fractional-flow model for radial flow is used. Gravity override and viscous fingering are not examined here. The effect of foam on oil displacement is complex in nature and is still unresolved; therefore, it is ignored in this paper. Additionally, it is likely that oil, in the near wellbore region, has already been swept. The fractional-flow approach can be used if there is immobile oil present, but it is not addressed here. Some authors extended the fractional-flow theory to model foam displacements with mobile oil (Ashoori et al., 2010; Namdar Zanganeh et al., 2011).

In this paper, diversion of gas is studied as a function of surfactant slug size, in a single-slug SAG process, using the STARS model and the proposed modification by Namdar Zanganeh et al. (2011). The results show that diversion depends on injection method (SAG vs. preformed foam), surfactant-slug size, and whether foam completely collapses at residual water saturation S_{wr} . In order to illustrate the challenge of diverting flow in the presence of extreme differences in permeability, we also study the effect of sealing off the lowest-permeability layer (Bandera Gray) during surfactant injection prior to gas injection.

Other chemical and physical factors that affect foam are described elsewhere. For example, the effect of liquid and gas composition (Mannhardt et al.1993, Liu et al. 2005, Farajzadeh et al. 2010, Farajzadeh et al. 2012), the effect of oil composition and saturation (Nikolov et al. 1986, Lau et al. 1988, Kuhlman 1990, Simjoo et al. 2009, Simjoo and Zitha 2013), and the effect of miscibility, pressure or temperature (Chabert et al. 2014, Kapetas et al. 2015). Additionally, for communicating layers where cross-flow is possible, Bertin et al. (1998) found that the foam front moves at matching velocities in consolidated and unconsolidated sand medium. The effect of hysteresis is not considered here since a single-cycle SAG flood is modelled.

1.2. Problem Statement

For the reservoir configuration shown in **Figure 2**, we investigate the effect of reservoir heterogeneity, with the intention to estimate injectivity during a single-cycle SAG flood for different surfactant slug sizes to find the optimum volume that favours maximum diversion away from the highest-permeability layer. We use a one-dimensional radial reservoir model with formation properties based on laboratory data for four sandstones measured recently by Kapetas et al. (2015). The model assumes that each layer is homogeneous (isotropic and uniform permeability), uniform in height, and capillary isolated. A vertical injection well that penetrates the entire reservoir interval is assumed. The SAG flood process involves the high-quality regime only; therefore, the dryout function, commonly referred to as F_2 or F_w , in the STARS model and the Namdar Zanganeh et al. (2011) modification are modelled in this paper as discussed in Chapter 2. The layers have equal pore volume, with different heights (**Table 3**); individual and total pore volumes are 7,540 and 30,159 m^3 respectively.

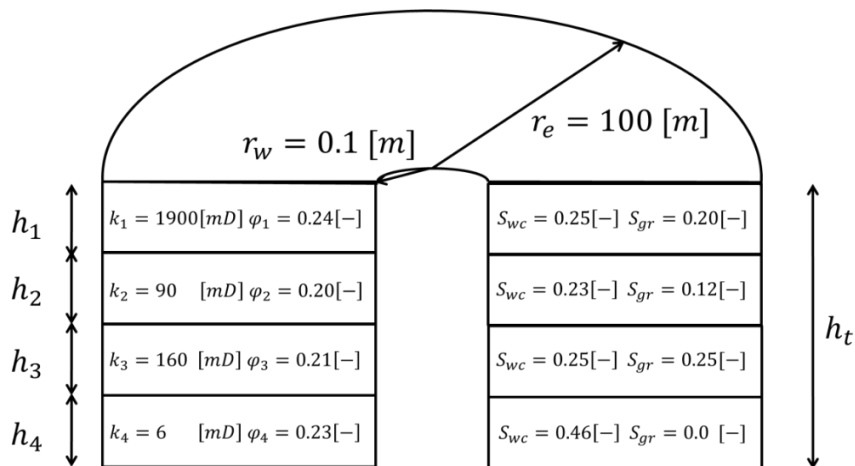


Figure 2: Problem Description

2 Methodology

2.1. Introduction

In reservoir simulation, mathematical models for foam flow are used in order to gain insight on key parameters controlling its flow in porous medium. The mathematical models are based on conservation of mass, momentum, and energy, in addition to an equation of state (EOS) that describes a fluid's reaction to changes in physical parameters. In this paper, isothermal and incompressible flow is assumed. Therefore, the model is simplified by ignoring the conservation of energy and the EOS equations.

In this section, the geometry of flow is described along with important notations including Darcy's law, Corey relative permeabilities, and mobility. The fractional-flow theory (FFT) for gas injection into a 100% water-saturated reservoir is then introduced. In order to simplify the system of equations, the FFT is put in dimensionless form. The solution using the method of characteristics (MOC), which is a mathematical technique for solving first-order partial differential equations (PDE), is then introduced for a single-layered reservoir and extended to a multi-layered reservoir. In addition, the solution of the FFT for a SAG process is introduced. The model is then developed to predict the diversion performance of a single-slug SAG process for various surfactant slug sizes. Cases are run for gas injection without surfactant, SAG in a fully surfactant-saturated reservoir, and SAG with finite slug of surfactant. Calculations are performed by a MATLAB code presented in Appendix B. Finally, details about the model's limitation and range of validity are highlighted.

2.2. Geometry of Flow

Fluid flow through porous media is greatly influenced by geometry. Most analytical models are developed on the basis of simplified flow geometries. The geometries relevant for fluid flow in porous media are:

- *Linear flow*: occurs in core floods and might be a good approximation to flow far from wells.
- *Radial flow*: occurs around most wells.
- *Spherical flow*: occurs near the tips of wells, and near perforations.

Spherical flow is not relevant in our case; therefore a comparison is only made between linear and radial flow. In this study, the drainage area is assumed to be cylindrical; therefore, the flow from an injection wellbore is radial. The main difference between linear and radial flow is that the flow area remains constant in linear flow while it changes as a function of radius in radial flow as shown in **Figure 3**. As a consequence, the pressure dissipates linearly in a linear flow and logarithmically in a radial flow. Because all fluids entering the wellbore have to pass through the narrow area around the wellbore, the highest superficial velocities (therefore highest pressure drop) in the reservoir occur there as shown in **Figure 4**. It is also assumed that the displacement occurs mainly in the radial direction. Therefore, the analysis is narrowed to one-dimensional radial flow.

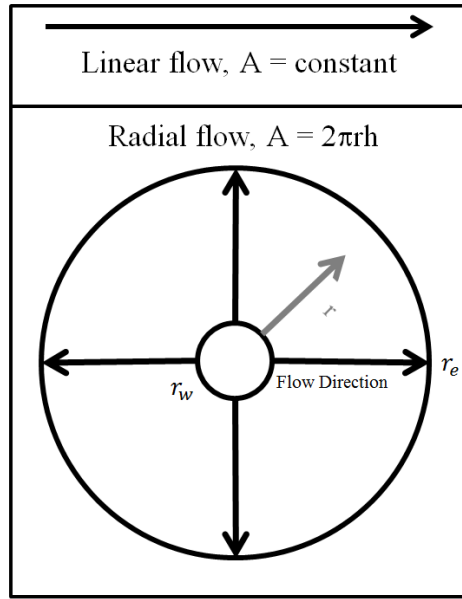


Figure 3: Linear vs. Radial Flow

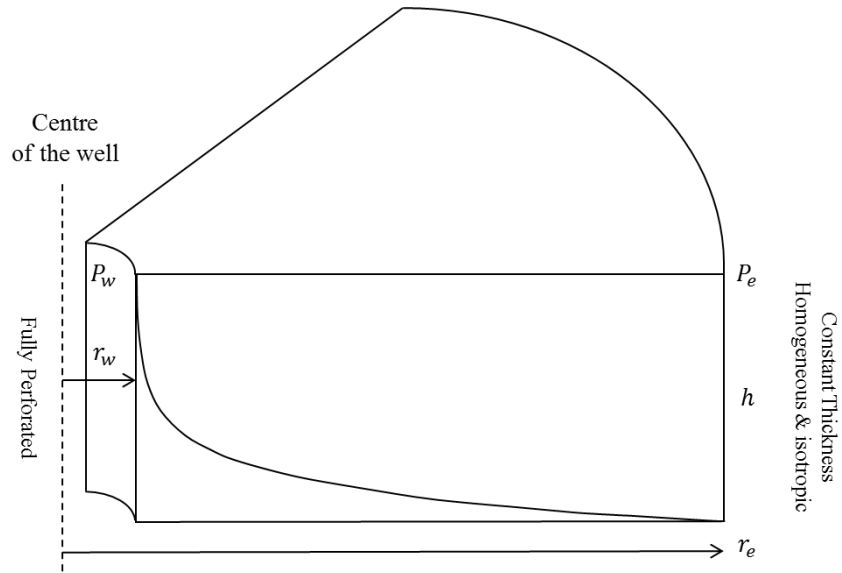


Figure 4: Pressure Dissipation for a Single-Layer Reservoir in Radial Flow

2.3. Darcy's Law

2.3.1. Darcy's Law for Single-Phase

Fluid flow through porous media is often described using Darcy's empirical relationship (Darcy, 1856). Darcy's law in differential form for flow of a single phase α in radial reservoir reads

$$u_{\alpha} = \frac{Q_{\alpha}}{A_r} = -\frac{k}{\mu_{\alpha}} \frac{d\Phi}{dr} = -\frac{k_{\alpha}}{\mu_{\alpha}} \left(\frac{\partial P_{\alpha}}{\partial r} + \rho_{\alpha} g \frac{\partial Z}{\partial r} \right) \quad (0.1)$$

The volumetric flow rate (Q_{α}) divided by the radial flow area (A_r) gives the superficial velocity of a fluid (u_{α}) that is proportional to the fluid's potential gradient ($d\Phi/dr$) and permeability (k) of the medium, and inversely proportional to the fluid's viscosity (μ_{α}). The fluid's potential includes the pressure gradient

(dP/dr) along with the elevation head gradient $(\rho g dP/dr)$, where (ρ_α) is the fluid's density and (g) is the universal gravitational constant. The law is analogous to Fourier's law in the field of heat conduction, Ohm's law in the field of electrical networks, and Fick's law in diffusion theory. If gravity is ignored equation (0.1) reads

$$u_\alpha = \frac{Q_\alpha}{A} = -\frac{k}{\mu_\alpha} \frac{\partial P}{\partial r} \quad (0.2)$$

Darcy's law assumes that viscous forces are dominant (low Reynolds's number), and there is no turbulence. Applying Darcy's law to gas flow in porous media at low pressure is complicated and requires additional modifications.

2.3.1. Darcy's Law for Multiphase Flow

Darcy's law could be extended to describe multiphase flow in porous media as follows

$$u_\alpha = \frac{Q_\alpha}{A_\alpha} = -\frac{kk_{r\alpha}(S_\alpha)}{\mu_\alpha} \frac{\partial P}{\partial r} \quad (0.3)$$

The same notations in equation (0.2) hold for phase α with the introduction of the relative permeability of phase α ($k_{r\alpha}$), which is a function of the phase's saturation (S_α). $k_{r\alpha}$ is a dimensionless term devised to adapt Darcy's law to multiphase flow conditions. It describes the ratio of effective permeability of a particular fluid at a particular saturation to absolute permeability of that fluid at total saturation. Therefore, if a single fluid is present in a rock, its relative permeability is one. Calculation of relative permeability allows comparison of the different abilities of fluids to flow in the presence of each other, since the presence of more than one fluid generally inhibits flow. Relative permeability is generally a nonlinear, path-dependent, function of the phase saturations.

2.4. Corey Relative Permeabilities

Essentially all calculations of EOR process performance are based on the use of relative-permeability functions that describe the local movement of phases based on their saturations. Corey's semi-empirical relations are commonly used to describe the relationship of relative permeability to the given phase saturation. An underlying assumption of Corey's relative permeabilities is that the flow of one phase is only affected by its own saturation and not by the flow of other phases. For two-phase flow, water and gas in our case, the relative permeabilities are described by

$$k_{rw}(S_w) = k_{rwe} \left(\frac{S_w - S_{wr}}{1 - S_{wr} - S_{gr}} \right)^{n_w} \quad S_{wr} \leq S_w \leq 1 - S_{gr} \quad (0.4)$$

$$k_{rg}(S_w) = k_{rge} \left(\frac{1 - S_w - S_{wr}}{1 - S_{wr} - S_{gr}} \right)^{n_g} \quad S_{gr} \leq S_g \leq 1 - S_{wr} \quad (0.5)$$

where k_{rwe} and k_{rge} refer to the end-point relative permeabilities, i.e., the relative permeability of one phase at irreducible saturation of the other phase. S_w , S_{wr} , and S_{gr} refer to the water saturation, residual water saturation, and residual gas saturation respectively. The permeability of a phase increases monotonically with an increase of its saturation. The terms n_w and n_g are the water and gas saturation exponents that define the shape of relative-permeability curves. The higher the saturation exponent, the more non-linear the associated change in relative permeability to the phase's saturation. When the exponent is equal to one, the

relationship becomes linear. Water is the wetting phase in the sandstone cores used in this paper. Due to differences in wetting properties, the two functions are different. Small amounts of water have little effects on the relative permeability of gas (non-wetting-phase), whereas small amounts of gas considerably reduce the relative permeability of water. The wetting phase tends to retreat in the small pores, which does not interfere with the non-wetting phase permeability. However, a small amount of the non-wetting phase occupies the large pores, blocking the flow of wetting phase in those pores. Therefore, n_w is larger (k_{rw} is more nonlinear) than n_g , as shown in **Table 2**. For gas injection, drainage curves are used since the gas phase saturation is increasing. The relative permeability curves as a function of water saturation for the Bentheimer, Berea, Sister Berea, and Bandera Gray layers can be found in **Figure 126**, **Figure 132**, **Figure 138**, and **Figure 144** respectively.

2.5. Mobility

Mobility describes the ease with which a particular fluid moves through porous medium under the influence of a pressure gradient. It is the ratio of effective permeability (k_α) to phase viscosity (μ_α), and could be written as

$$\lambda_w(S_w) = \frac{k_w(S_w)}{\mu_w} = \frac{kk_{rw}(S_w)}{\mu_w} = k\lambda_{rw}(S_w) \quad (0.6)$$

$$\lambda_g(S_w) = \frac{k_g(S_w)}{\mu_g} = \frac{kk_{rg}(S_w)}{\mu_g} = k\lambda_{rg}(S_w) \quad (0.7)$$

where λ_w and λ_g are the water and gas mobilities; also, λ_{rw} and λ_{rg} are the water and gas relative mobilities. Equation (0.3) could be expressed in terms of relative mobility as follows

$$u_\alpha = -k\lambda_{r\alpha}(S_w) \frac{\partial P}{\partial r} \quad (0.8)$$

The total relative mobility is defined as the summation of the relative mobilities of the various phases at specific water saturation as follows

$$\lambda_{rt}(S_w) = \lambda_{rw}(S_w) + \lambda_{rg}(S_w) \quad (0.9)$$

The total relative mobility curves as a function of water saturation for the Bentheimer, Berea, Sister Berea, and Bandera Gray layers can be found in **Figure 128**, **Figure 134**, **Figure 140** and **Figure 146** respectively.

The mobility ratio at a displacement front (M) is defined as the mobility of the displacing fluid divided by the mobility of the displaced fluid both taken at their saturations upstream and downstream of the front.

$$M = \frac{\lambda_{rt}^+}{\lambda_{rt}^-} \quad (0.10)$$

Where $^+$ and $^-$ denote saturations upstream and downstream of the front respectively. If the mobility ratio is unfavourable (greater than unity), the upstream bank tends to finger through and bypass the displaced fluid downstream. The mobility ratios for gas with and without surfactant can be found in **Table 7**.

2.6. Pressure Difference

2.6.1. Pressure Difference for Single-Phase Flow

For single phase flow, the pressure difference between the wellbore radius r_w and the outer radius r_e is obtained by integrating equation (0.2) as follows

$$\int_{P_e}^{P_w} dP_\alpha = - \int_{r_e}^{r_w} \frac{Q_\alpha \mu_\alpha}{A(r) k k_{r\alpha}} dr = \int_{r_w}^{r_e} \frac{Q_\alpha}{A(r) k \lambda_{r\alpha}} dr \quad (0.11)$$

where area of flow is based on the radial distance r as $A(r) = 2\pi rh$. Since the phase mobility for single phase flow is constant, the solution reads

$$P_w - P_e = \Delta P_\alpha = \frac{Q_\alpha}{2\pi h k \lambda_{r\alpha}} \ln \left(\frac{r_e}{r_w} \right) \quad (0.12)$$

2.6.2. Pressure Difference for Multiphase Flow

Since the flow is incompressible, the total flow rate is equal to

$$u_t = \frac{Q_t}{A} = u_w + u_g \quad (0.13)$$

Expanding the term using (0.8) leads to

$$u_t = - \left(k \lambda_{rw}(S_w) \frac{\partial P_w}{\partial r} + k \lambda_{rg}(S_w) \frac{\partial P_g}{\partial r} \right) \quad (0.14)$$

If capillary forces are neglected, the pressure gradient in both phases is equivalent. Additionally, incorporating equation (0.9) gives

$$u_t = -k \lambda_{rt}(S_w) \frac{dP}{dr} \quad (0.15)$$

Integrating equation (0.14) to get the pressure difference between the wellbore radius r_w and the outer radius r_e leads to

$$\int_{P_e}^{P_w} dP_\alpha = \int_{r_w}^{r_e} \frac{Q_t}{2\pi r h k \lambda_{rt}} dr \quad (0.16)$$

After integration, the pressure difference is

$$P_w - P_e = \frac{Q_t}{2\pi h k} \int_{r_w}^{r_e} \frac{1}{r \lambda_{rt}(S_w(r))} dr \quad (0.17)$$

The total relative mobility in this case changes as a function of water saturation that also changes with injection as a function of radius. In general, analytical integration of equation (0.17) is not possible. If, for any saturation, the radial position is known as is the case in fractional-flow theory, one can estimate the total relative mobility at every radius r . Therefore, the solution could be obtained using numerical integration.

2.7. Fractional-Flow Theory

2.7.1. Introduction and Assumptions

Buckley and Leverett (1942) derived the formulation for the fractional flow theory (FFT) for the purpose of estimating the efficiency of water floods. Since then, the theory has proven useful for a variety of EOR processes (Pope, 1980; Welsh and Lake, 1989; Lake et al., 2014). In this case, the application of the theory for foam EOR processes is discussed (Zhou and Rossen, 1994; Zhou and Rossen, 1995). The beauty of the fractional flow theory is that it simplifies the prediction of multiphase flow in porous media by using the fractional-flow function f_w . The theory makes many simplifying assumptions:

- 1) The flow is one-dimensional, through an isothermal permeable medium. There are no phase changes.
- 2) The rock and fluids, including gas, are incompressible.
- 3) The fluids do not react chemically with rock, except for surfactant adsorption
- 4) The phases immediately take the steady-state mobilities dictated by their saturations, fractional flows and the presence or absence of surfactants.
- 5) Dispersion and viscous fingering can be ignored.
- 6) The initial conditions are uniform in the medium.
- 7) At most there are two phases:
 - A gas phase that contains gas only
 - An aqueous phase, which contains water, or water and surfactant only.
- 8) At most, three components are present: water, gas, and surfactant.
- 9) The fractional-flow curve applies
- 10) Newtonian mobilities for all phases

Despite the simplifying assumptions, the theory has proven very useful in evaluating flooding processes.

2.7.2. Water Fractional-Flow Notation

For two-phase flow of water and gas, the fractional-flow of water f_w is defined as the fraction of water flow relative to the total flow rate. It could be written as follows

$$f_w \equiv \frac{Q_w}{Q_w + Q_g} = \frac{u_w}{u_w + u_g} \quad (0.18)$$

The term could be expanded using equation (0.8) to give

$$f_w(S_w) = \frac{\lambda_{rw}(S_w)}{\lambda_{rw}(S_w) + \lambda_{rg}(S_w)} \quad (0.19)$$

The fractional flow function can be further simplified to

$$f_w(S_w) = \left(1 + \frac{\lambda_{rg}(S_w)}{\lambda_{rw}(S_w)} \right)^{-1} \quad (0.20)$$

Fractional-flow curves for the Bentheimer, Berea, Sister Berea, and Bandera Gray are shown in [Figure 127](#), [Figure 133](#), [Figure 139](#) and [Figure 145](#) respectively.

2.7.3. Mass Balance

The principle of mass conservation states that for an incompressible system, the mass must remain constant. This could be translated into the following

$$\text{Flow in} - \text{Flow Out} = \text{Accumulation} \quad (0.21)$$

The terms in the equation (0.21) for water flow are

$$\text{Flow in} = 2\pi r h (u_w)_r \rho \Delta t = (Q_w)_r \rho \Delta t \quad (0.22)$$

$$\text{Flow out} = 2\pi (r + \Delta r) h (u_w)_{r+\Delta r} \rho \Delta t = (Q_w)_{r+\Delta r} \rho \Delta t \quad (0.23)$$

$$\text{Accumulation} = (2\pi r \Delta r h \rho \phi S_w)_{t+\Delta t} - (2\pi r \Delta r h \rho \phi S_w)_t \quad (0.24)$$

where the terms ϕ, ρ and t refer to porosity, density and time respectively. Combining the terms lead to

$$(Q_w)_r \rho \Delta t - (Q_w)_{r+\Delta r} \rho \Delta t = (2\pi r \Delta r h \rho \phi S_w)_{t+\Delta t} - (2\pi r \Delta r h \rho \phi S_w)_t \quad (0.25)$$

Dividing by the radial and time increments combined with the assumption that the fluids and matrix are incompressible leads to

$$\frac{(Q_w)_r - (Q_w)_{r+\Delta r}}{\Delta r} = 2\pi r h \phi \frac{(S_w)_{t+\Delta t} - (S_w)_t}{\Delta t} \quad (0.26)$$

Taking the limit when Δr and Δt are approaching zero leads to the differential form that is

$$-\frac{\partial(Q_w)}{\partial r} = 2\pi r h \phi \frac{\partial(S_w)}{\partial t} \quad (0.27)$$

Incorporating equation (0.18) and rearranging leads to

$$\phi \frac{\partial S_w}{\partial t} + \frac{Q_t}{2\pi r h} \frac{\partial f_w}{\partial r} = 0 \quad (0.28)$$

2.7.4. Dimensionless Parameters

2.7.4.1. Dimensionless Position

The dimensionless position is defined as the fraction of pore volume back to injection point; for radial flow, it is written as

$$x_D(r) \equiv \frac{r^2 - r_w^2}{r_e^2 - r_w^2} \quad x_D \in [0, 1] \quad (0.29)$$

The quadratic nature of the dimensionless position can be seen in [Figure 5](#).

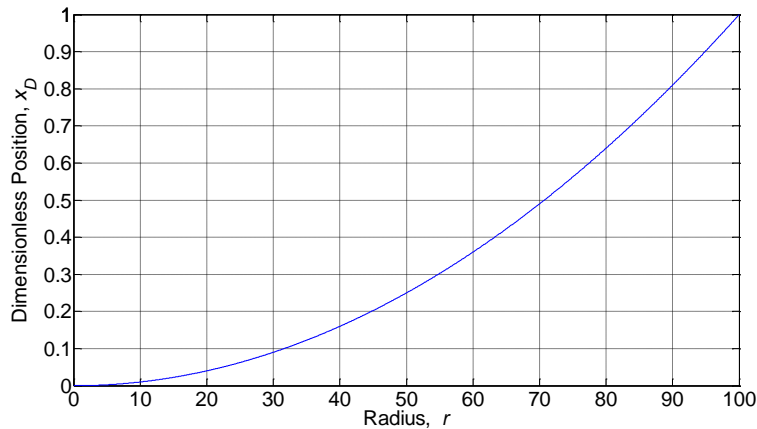


Figure 5: Reservoir Radius (r) vs. Dimensionless Position (x_D)

2.7.4.2. Dimensionless Time

The dimensionless time is defined as the cumulative pore volume injected divided by the pore volume of the region of interest, and can be written as

$$t_D \equiv \int \frac{Q_t dt}{\pi(r_e^2 - r_w^2)h\phi} \quad t_D > 0 \quad (0.30)$$

2.7.4.3. Dimensionless Pressure

In order to simplify the calculations, the total pressure difference in each layer is normalized here by the pressure difference caused by injecting water at the same volumetric rate into a fully water-saturated layer, i.e., $S_w=1$. The resulting value is dimensionless and is written as

$$P_D = \frac{P_{r_w} - P_{r_e}}{(P_{r_w} - P_{r_e})_{S_w=1}} = \frac{\Delta P_g}{\Delta P_w} = \frac{\frac{Q_g}{2\pi kh} \int_{r_w}^{r_e} \frac{1}{r \lambda_{rt}(S_w)} dr}{\frac{Q_w}{2\pi kh \lambda_{rw}} \ln\left(\frac{r_e}{r_w}\right)} \quad (0.31)$$

The relative water mobility for a water-saturated reservoir is $1/\mu_w = 1,000$ [Pa.s]⁻¹. Cancelling out similar terms in equation (0.31) leads to

$$P_D = \frac{\int_{r_w}^{r_e} \frac{1}{r \lambda_{rt}(S_w)} dr}{1000 \times \ln\left(\frac{r_e}{r_w}\right)} \quad (0.32)$$

2.7.5. FFT in Dimensionless Notations

The derivative of the dimensionless position with respect to radius is

$$\frac{dx_D}{dr} = \frac{2r}{r_e^2 - r_w^2} \quad (0.33)$$

The derivative of the dimensionless time with respect to physical time is

$$\frac{dt_D}{dt} = \frac{Q_t}{\pi(r_e^2 - r_w^2)h\phi} \quad (0.34)$$

Rearranging equation (0.33-0.34) and applying them into equation (0.28) leads to

$$\frac{Q_t \phi}{\pi(r_e^2 - r_w^2)h\phi} \frac{\partial S_w}{\partial t_D} + \frac{Q_t}{2\pi r h} \frac{2r}{(r_e^2 - r_w^2)} \frac{\partial f_w}{\partial x_D} = 0 \quad (0.35)$$

The terms cancel out, and the equation in dimensionless terms becomes

$$\frac{\partial S_w}{\partial t_D} + \frac{\partial f_w}{\partial x_D} = 0 \quad (0.36)$$

The fractional-flow is a function of water saturation only, and is independent of position and time; therefore, applying the chain rule to the partial differential equation leads to

$$\frac{\partial S_w}{\partial t_D} + \frac{df_w}{dS_w} \frac{\partial S_w}{\partial x_D} = 0 \quad (0.37)$$

The above equation is a first-order hyperbolic PDE; this means that saturation waves travel with a finite speed of propagation through the medium from a “source” or upstream boundary only in downstream direction (no information downstream of wave is needed). The saturation depends only on dimensionless position and time $S_w(x_D, t_D)$. Therefore, for a constant saturation, the total derivative dS_w could be written as

$$dS_w(x_D, t_D) = \frac{\partial S_w}{\partial t_D} dt_D + \frac{\partial S_w}{\partial x_D} dx_D = 0 \quad (0.38)$$

Rearranging equation (0.37) and using equation (0.38) leads to

$$\left(\frac{dx_D}{dt_D} \right)_{dS_w=0} = - \frac{\frac{\partial S_w}{\partial t_D}}{\frac{\partial S_w}{\partial x_D}} = \frac{df_w}{dS_w} = v_{s_w} \quad (0.39)$$

This equation expresses the velocity at which a particular value of saturation propagates through the medium, i.e., the saturation velocity, v_s , that is equal to the slope of the fractional-flow curve. For constant saturations, the PDE is reduced to a family of ordinary differential equations (ODE) along which the solution can be integrated from some initial conditions. This is called the method of characteristics (MOC), which is a technique typically used for solving first-order hyperbolic PDEs.

The initial condition I is assumed here to be at $S_w=1$ with uniform surfactant concentration. The gas injection condition J is at $S_w=S_{wr}$ because the injected gas fraction $f_g=1$ (i.e. $f_w=0$). The solution for the displacement is represented as a path along the fractional-flow curve from J to I with monotonically increasing slopes of the f_w curve (i.e. velocities). For a constant saturation, the equation implies that the velocity, v_s , is constant along a ‘characteristic’ path. If the velocities are not monotonically increasing from J to I , a portion of the solution is replaced by a tangent line that represents a discontinuity or shock from a value of f_w at $S_{w,shock}$ to the initial condition I . The cause of the shock is that the material upstream is travelling faster than downstream, which leads to an accumulation and therefore a “shock”. Only saturations below the point of tangency are actually observed in the displacement. The shock saturation moves with the highest velocity and behind it is a spreading wave (i.e. rarefaction) of progressively drier saturations with decreasing speed back to the injection condition J at the wellbore. This can be seen in the dimensionless time-distance diagrams in Appendix B for the gas injection without surfactant and for SAG using the STARS model and the modified model of Namdar Zanganeh et al. (2011).

2.8. Solution Method

2.8.1. For Gas Injection in a Single-Layer Reservoir

The goal is to estimate the dimensionless pressure P_D for every dimensionless pore volume injected t_D . The shock saturation is calculated using the derivative of the fractional flow curve to determine the range of saturations observed in the displacement process. The velocities of the saturation waves are then calculated to determine their radial position along with their total relative mobilities. Then the pressure is integrated from the injection well outward. A simplistic view for this flooding process is shown in **Figure 6**. The solution procedure is outlined below.

The derivative of the water fractional flow for gas and water without surfactant is given by

$$\frac{df_{w,g}}{dS_w} = \frac{d}{dS_w} \left(1 + \frac{\lambda_{rg}(S_w)}{\lambda_{rw}(S_w)} \right)^{-1} = - \left(\frac{\lambda_{rw}(S_w) + \lambda_{rg}(S_w)}{\lambda_{rw}(S_w)} \right)^{-2} \left(\frac{\lambda_{rw}(S_w)\lambda'_{rg}(S_w) - \lambda_{rg}(S_w)\lambda'_{rw}(S_w)}{\lambda_{rw}(S_w)^2} \right) \quad (0.40)$$

Simplifying equation (0.40) leads to

$$\frac{df_{w,g}}{dS_w} = \frac{\lambda_{rg}(S_w)\lambda'_{rw}(S_w) - \lambda_{rw}(S_w)\lambda'_{rg}(S_w)}{(\lambda_{rw}(S_w) + \lambda_{rg}(S_w))^2} \quad (0.41)$$

The derivatives for gas and water relative mobilities with respect to water saturation are

$$\lambda'_{rw}(S_w) = \frac{n_w k_{rwe} \left(\frac{S_w - S_{wc}}{1 - S_{wc} - S_{gr}} \right)^{(n_w-1)}}{\mu_w (1 - S_{wc} - S_{gr})} \quad (0.42)$$

$$\lambda'_{rg}(S_w) = - \frac{n_g k_{rge} \left(\frac{1 - S_w - S_{wc}}{1 - S_{wc} - S_{gr}} \right)^{(n_g-1)}}{\mu_g (1 - S_{wc} - S_{gr})} \quad (0.43)$$

Furthermore, the shock saturation is obtained by solving for the point of tangency to the f_w curve for a line passing through point (1, 1) as follows

$$f_w(S_w) + \frac{df_{w,g}(S_w)}{dS_w} (1 - S_w) - 1 = 0 \quad (0.44)$$

The shock saturations for the Bentheimer, Berea, Sister Berea, and Bandera Gray layers are shown in [Figure 127](#), [Figure 133](#), [Figure 139](#) and [Figure 145](#) respectively. The saturation values of the shocks for gas flooding without surfactant and for SAG using the STARS model and the modified model of Namdar Zanganeh et al. are found in [Table 4](#), [Table 5](#), and [Table 6](#).

The dimensionless positions of the characteristics are based on their velocities and PV of gas injected (t_D). In order to eliminate any characteristics that have reached the production well, the minimum function is used. For a specific dimensionless time t_D , the dimensionless position for each value of S_w is

$$x_D(S_w) = \min \left(\left(t_D \frac{df_{w,g}(S_w)}{dS_w} \right), 1 \right) \quad (0.45)$$

The dimensional position for each characteristic is calculated using equation (0.29) as follows

$$r(S_w) = \sqrt{x_D(S_w)(r_e^2 - r_w^2) + r_w^2} \quad (0.46)$$

Using the average mobilities between two consecutive radii (r_i and r_{i+1}), the pressure difference is estimated by

$$P_{i+1} - P_i = \frac{Q_i}{2\pi kh} \frac{1}{2} \left(\frac{1}{\lambda_{r,i}} + \frac{1}{\lambda_{r,i+1}} \right) \ln \left(\frac{r_{i+1}}{r_i} \right) \quad (0.47)$$

We calculate positions and pressures for 200 characteristics (M) of saturations between the injection condition J and the shock saturation. Then, the pressure difference between the wellbore to the shock radii ($P_{r_w} - P_{r_{shock}}$) is calculated by the summation of all the pressure increments. Therefore, the numerical integration of equation (0.17) is

$$\Delta P_g = P_{r_w} - P_{r_{shock}} = \frac{q_i}{2\pi hk} \int_{r_e}^{r_w} \frac{1}{r \lambda_{r_i}(S_w)} dr = \sum_{i=1}^M (P_{i+1} - P_i) \quad (0.48)$$

where P_i and r_i are the pressure and radius at the wellbore. Similarly, P_M and r_M are the pressure and radius at the shock. Ahead of the gas bank, the pressure difference caused by the water bank at initial conditions ($S_w=1$), is calculated using equation (0.12)

$$\Delta P_w = P_{r_{shock}} - P_{r_e} = \frac{Q_i}{2\pi kh \lambda_{r_w}} \ln \left(\frac{r_e}{r_{shock}} \right) \quad (0.49)$$

Therefore, the total pressure difference between the wellbore and outer radii is

$$P_{r_w} - P_{r_e} = \Delta P_g + \Delta P_w \quad (0.50)$$

The dimensionless pressure in this case is

$$P_D = \frac{\Delta P_g + \Delta P_w}{\frac{Q}{2\pi kh \lambda_{r_w}} \ln \left(\frac{r_e}{r_w} \right)} \quad (0.51)$$

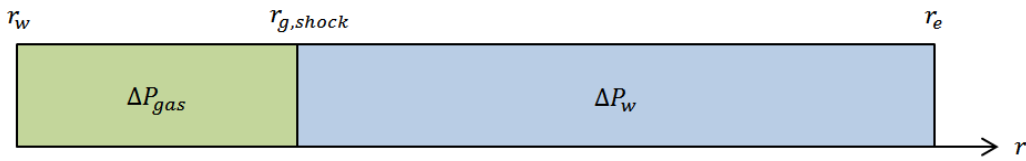


Figure 6: Gas Injection into a Water-Saturated Reservoir

2.8.2. For Gas Injection in a Multi-Layer Reservoir

In the hypothetical reservoir scenario studied here, the four sandstone non-communicating layers are assumed to have equal pore volume. The calculated height of each layer is shown in Table 3 in Appendix A. The pressure difference between the boundaries at the wellbore radius r_w and the external radius r_e is assumed to be the same for all layers. In a multi-layered reservoir, the positions of the various waves reflect the cumulative injection into layers and in turn control the respective injection rates. In order to estimate injectivity in a layered-reservoir, we increment in small steps (n) of total dimensionless time $t_{D_{total}}$. For every step (n), the volumetric flow ratio injected into each layer is estimated based on: permeability k , height h , and dimensionless pressure P_D . The cumulative injectivity ratio (R), the average dimensionless pressure $P_{D_{total}}$ for the entire reservoir, and the relative time are introduced below. Details of solution procedure are outlined below as well.

The pore volume (PV) of an individual layer (j) is

$$PV_j = \pi (r_e^2 - r_w^2) h_j \phi_j \quad (0.52)$$

The total pore volume is calculated by summing the pore volumes of all layers as follows

$$PV_{total} = \sum_{j=1}^4 \pi (r_e^2 - r_w^2) h_j \phi_j \quad (0.53)$$

The dimensionless pore volume t_D for an individual layer (j) is defined by the total pore volume of gas injected into each layer divided by the layer's pore volume. It could be written as

$$t_{D_j} \equiv \int \frac{Q_j dt}{\pi (r_e^2 - r_w^2) h_j \phi_j} = \int \frac{Q_j dt}{PV_j} \quad (0.54)$$

The total dimensionless time $t_{D_{total}}$ is defined by the total pore volume injected into all layers divided by the total reservoir volume

$$t_{D_{total}} = \sum_{j=1}^4 t_{D_j} = \frac{\sum_{j=1}^4 \int Q_j dt}{PV_{total}} \quad (0.55)$$

The gas injection into the reservoir is calculated using increments of total dimensionless time $\Delta t_{D_{total}}$, defined as

$$\Delta t_{D_{total}} = \frac{\Delta V_{total}}{PV_{total}} \quad (0.56)$$

In order to track the dimensionless pore volume injected into a certain layer, the following need to be calculated. First, the fraction (F_j) of an individual layer's pore volume relative to the total reservoir volume is calculated as follows

$$F_j = \frac{PV_j}{PV_{total}} = \frac{\pi (r_e^2 - r_w^2) h_j \phi_j}{\sum_{j=1}^4 \pi (r_e^2 - r_w^2) h_j \phi_j} = \frac{h_j \phi_j}{\sum_{j=1}^4 h_j \phi_j} \quad (0.57)$$

For all layers in this study, $F_j = 1/4$. The fraction of the dimensionless time increment Δt_{D_j} for an individual layer divided by the total dimensionless time increment $\Delta t_{D_{total}}$ is

$$\frac{\Delta t_{D_j}}{\Delta t_{D_{total}}} = \frac{\frac{\Delta V_j}{PV_j}}{\frac{\Delta V_{total}}{PV_{total}}} = \frac{\Delta V_j}{\Delta V_{total}} \frac{PV_{total}}{PV_j} = \frac{\Delta V_j}{\Delta V_{total}} F_j^{-1} \quad (0.58)$$

where the flow ratio for each time increment is calculated by

$$\frac{\Delta V_j}{\Delta V_{total}} = \frac{\frac{k_j h_j}{P_{D_j}}}{\sum_{j=1}^4 \frac{k_j h_j}{P_{D_j}}} \quad (0.59)$$

Therefore, the individual layer's increment in PV injected (Δt_{D_j}) is equivalent to

$$\Delta t_{D_j} = \frac{\frac{k_j h_j}{P_{D_j}}}{\sum_{j=1}^4 \frac{k_j h_j}{P_{D_j}}} \Delta t_{D_{total}} F_j^{-1} \quad (0.60)$$

The mobilities into each layer change with injection as the saturation of the injected fluid increases. Therefore, a time counter in increments of total dimensionless time ($1 \leq n \leq N$) is introduced where N represents the total number of dimensionless time increments. For the first time step ($n=1$), the dimensionless time for layer (j) is

$$t_{D_j}^{n=1} = \frac{\frac{k_j h_j}{P_{D_j}^{n=1}}}{\sum_{j=1}^4 \frac{k_j h_j}{P_{D_j}^{n=1}}} F_j^{-1} \Delta t_{D_{total}}^{n=1} \quad (0.61)$$

We increment forward in dimensionless time by using the previously outlined procedure for each layer individually in order to calculate the dimensionless pressure P_D at the next time step; the individual pore volume in each layer increases as follows

$$t_{D_j}^{n+1} = t_{D_j}^n + \frac{\frac{k_j h_j}{P_{D_j}^{n+1}}}{\sum_{j=1}^4 \frac{k_j h_j}{P_{D_j}^{n+1}}} F_j^{-1} \Delta t_{D_{total}}^{n+1} \quad (0.62)$$

This shows that the volume received by each layer is proportional to the layer's permeability and height and inversely proportional to the dimensionless pressure of that layer at any given dimensionless time. For each total dimensionless time increment, the dimensionless time and the associated dimensionless pressure for each layer is calculated in order to estimate injectivity.

The ratio of cumulative injection into each layer (j) at each dimensionless time step (n) is

$$R_j^n = \frac{t_{D_j}^n}{\sum_{j=1}^4 t_{D_j}^n} \quad (0.63)$$

This is a measure of how much injection a layer has received relative to the other layers at a specific dimensionless time step (n). The total dimensionless pressure $P_{D_{total}}$ of the reservoir is defined as the injectivity of gas into all layers divided by the injectivity of water at the same volumetric rate. For each dimensionless time step (n), it is

$$P_{D_{total}}^n = \frac{\sum_{j=1}^4 \frac{k_j h_j}{P_{D_w}}}{\sum_{j=1}^4 \frac{k_j h_j}{P_{D_j}^n}} = \frac{\sum_{j=1}^4 k_j h_j}{\sum_{j=1}^4 \frac{k_j h_j}{P_{D_j}^n}} \quad (0.64)$$

2.8.2.1. Relative Time Derivation

Since the injection rates into different layers vary during simultaneous injection according to the mobilities in each layer, a given dimensionless time in the various layers does not necessarily correspond to the same physical time. Relative time is defined as the ratio of time it takes to inject a given volume of gas to the time it takes to inject the same volume of water into a water-saturated reservoir ($S_w=1$).

The injection rate scales with $1/P_D$ when injection pressure is fixed, and the advance of physical time scales to the integral of P_D with respect to t_D . The relative time is given by

$$relative\ time = \int_0^1 P_D dt_D = \sum_{n=1}^N P_D^n \Delta t_D^n \quad (0.65)$$

This is relative time for a single-layered reservoir. Similarly, for a multi-layered reservoir, the relative time is obtained through the integration of the total dimensionless pressure $P_{D_{total}}$ (equation 0.64) over the total dimensionless time $t_{D_{total}}$ as follows

$$relative\ time = \int_0^1 P_{D_{total}} dt_{D_{total}} = \sum_{n=1}^N P_{D_{total}}^n \Delta t_{D_{total}}^n \quad (0.66)$$

2.8.3. For SAG Using Single Surfactant-Slug

Similarly, the FFT theory could also be applied to foam flow in porous media. To simplify the problem, several assumptions are imposed. First, fixed residual oil saturation can be assumed; however, we assume that only water and gas are present in the reservoir. Second, the reservoir is fully saturated with surfactants solution. Third, foam doesn't alter the water relative permeability function $k_{rw}(S_w)$. Fourth, the reduction of gas phase mobility is represented by modifying gas relative permeability only. Fifth, foam is present in the reservoir wherever there is surfactant and gas. Finally, surfactant adsorption is neglected. A simplistic view for this flooding process for a single-layered reservoir is displayed in **Figure 7**.

In the STARS model, the reduction of the gas relative permeability due to the presence of foam is expressed through a foam mobility-reduction factor (FM) multiplied by the gas relative permeability (k_{rg}) in the absence of foam. This is given by

$$k_{rg}^f(S_w) = FM(S_w) k_{rg}(S_w) \quad (0.67)$$

FM is a dimensionless modifier that represents the factor by which gas mobility is reduced due to the presence of foam relative to the gas mobility at the same water saturation in the absence of foam. It is defined as

$$FM(S_w) = \frac{1}{1 + fmmob F_1 F_2 F_3 F_4 F_5 F_6} \quad 0 \leq F_i \leq 1 \quad (0.68)$$

where $fmmob$ represents the reference mobility reduction factor; it is the reduction in gas mobility at maximum foam strength. Each F_i is a dimensionless coefficient that represents the effect of surfactant concentration, water saturation, oil saturation, capillary number, gas velocity, and critical capillary number, respectively, on foam behaviour (CMG, 2012).

In this paper, we only use the F_2 function, which represents the effect of water saturation on foam behaviour. It is commonly known as the dryout function or F_w . This function controls foam behaviour in the high-quality regime (Cheng et al., 2000), which is crucial to SAG processes. Therefore, the foam mobility-reduction factor (FM) becomes

$$FM(S_w) = \frac{1}{1 + fmmob F_w} \quad (0.69)$$

In the STARS model, the dryout function is written as

$$F_w(S_w) = 0.5 + \frac{\arctan(epdry(S_w - fmdry))}{\pi} \quad (0.70)$$

$epdry$ controls the abruptness of foam collapse as a function of water saturation; small values give a gradual transition between the two regimes, while larger values yield a sharper transition. However, according to equation (0.70), foam does not fully collapse at any water saturation including S_{wc} . $fmdry$ is the water saturation near which foam abruptly weakens.

Similar to equation (0.9), the total relative mobility of gas in the presence of foam λ_{rt}^f is

$$\lambda_{rt}^f(S_w) = \lambda_{rw}(S_w) + \lambda_{rg}^f(S_w) = \frac{k_{rw}(S_w)}{\mu_w} + \frac{k_{rg}^f(S_w)}{\mu_g} \quad (0.71)$$

The superscript (f) indicates the presence of foam. The total relative mobility curves as a function of water saturation for the Bentheimer, Berea, Sister Berea, and Bandera Gray layers can be found in [Figure 128](#), [Figure 134](#), [Figure 140](#) and [Figure 146](#) respectively. The fractional flow function in this case is

$$f_w(S_w) = \left(1 + \frac{\lambda_{rg}^f(S_w)}{\lambda_{rw}(S_w)} \right)^{-1} \quad (0.72)$$

Fractional-flow curves for the Bentheimer, Berea, Sister Berea, and Bandera Gray layers are shown in [Figure 127](#), [Figure 133](#), [Figure 139](#) and [Figure 145](#) respectively. The analytical derivative of the fractional flow is

$$\frac{df_{w,f}}{dS_w} = \frac{\lambda_{rg}^f(S_w)\lambda_{rw}'(S_w) - \lambda_{rw}(S_w)\lambda_{rg}^{f'}(S_w)}{(\lambda_{rw}(S_w) + \lambda_{rg}^f(S_w))^2} \quad (0.73)$$

The derivative of the foam relative mobility is

$$\lambda_{rg}^{f'}(S_w) = FM'(S_w)\lambda_{rg}(S_w) + FM(S_w)\lambda_{rg}'(S_w) \quad (0.74)$$

The derivative of the foam mobility reduction factor (FM) is

$$FM'(S_w) = -\frac{FM^2 \times fmmob \times epdry}{\pi(1 + epdry^2(S_w - fmdry)^2)} \quad (0.75)$$

The same solution procedure outlined earlier for fractional-flow theory for gas without foam is followed. Similar to equation (0.48), the pressure difference in the foam bank is

$$\Delta P_f = P_{r_w} - P_{r_{shock}} = \frac{q_t}{2\pi kh} \int_{r_e}^{r_w} \frac{1}{r \lambda_{rt}^f(S_w)} dr = \sum_{i=1}^M (P_{i+1} - P_i) \quad (0.76)$$

The main difference here is that the mobilities and speed of characteristics behind the shock are modified by the presence of foam. The dimensionless pressure in the case of gas injection into a fully surfactant saturated reservoir becomes

$$P_D = \frac{\Delta P_f + \Delta P_w}{\frac{Q}{2\pi kh\lambda_{r_w}} \ln\left(\frac{r_e}{r_w}\right)} \quad (0.77)$$

2.8.4. Modification of F_w by Namdar Zanganeh et al.

In the STARS model, foam doesn't completely collapse at residual water saturation, i.e. $F_w \neq 0$ at S_{wr} . Therefore, Namdar Zanganeh et al. (2011) suggested a simple modification to the dryout function, F_w

$$F_w(S_w) = \left(0.5 + \frac{\arctan(epdry(S_w - fmdry))}{\pi}\right) - \left(0.5 + \frac{\arctan(epdry(S_{wr} - fmdry))}{\pi}\right) \quad (0.78)$$

Note that in equation (0.78), $F_w(S_{wr}) = 0$. The extension does not alter the solution procedure except for the calculation of the dryout function. The derivative of FM remains the same since only a constant is added to the function.



Figure 7: Gas Injection into a Single Layer Surfactant-Saturated Reservoir

2.8.5. For SAG Using Different Surfactant Slug Sizes

Initially, the layers in this case are fully saturated with water ($S_w=1$) without surfactant. We inject different surfactant slug sizes with the assumption that the density and relative permeability do not change due to the presence of surfactant. The surfactant slug sizes are represented as fractions of the total reservoir pore volume $t_{D_{total}}$. Before gas breaks through the foam bank, the solution procedure for SAG remains the same as outlined earlier. After gas breakthrough, there are three regions in each layer foam bank, gas bank, and water at initial condition. In this case, the FFT for SAG and gas injection are combined. Details of the solution procedure are presented below.

Since the mobilities are constant during the injection of the surfactant slugs, the volume that goes into each layer (j), for a given surfactant slug is given by

$$v_{s_j} = V_s \frac{k_j h_j}{\sum_{j=1}^4 k_j h_j} \quad (0.79)$$

Where V_s represents the surfactant slug size, and v_{s_j} represents the amount of surfactant that goes into each layer (j). The volume of the surfactant bank in layer (j) is

$$v_{s_j} = \pi (r_{s_j}^2 - r_w^2) \phi_j h_j \quad (0.80)$$

Re-arranging the equation to solve for the radius of the surfactant bank (r_s) into layer (j) prior to gas injection is given by

$$r_{s_j} = \sqrt{\frac{V_{s_j}}{\pi\phi_j h_j} + r_w^2} \quad (0.81)$$

During gas injection in a SAG process, the water saturation profile is nearly uniform, at values similar to that at the point of tangency, i.e. shock, throughout almost the entire length of the foam bank. This is because almost all the change in slope (df_w/dS_w) from the value at the shock to zero occurs near $fmdry$ as shown in **Figure 127** in Appendix B. For simplicity, at gas breakthrough, we assume that the foam bank has uniform water saturation $S_w=fmdry$. Using a material balance on surfactant and ignoring adsorption, the radius of the foam bank into each layer (j) is

$$r_{f_j} = \sqrt{\frac{V_{s_j}}{\pi\phi_j h_j fmdry_j} + r_w^2} \quad (0.82)$$

Although the radius of the foam bank r_f would slowly increase a little after gas breakthrough as foam dries out, we assume that it remains constant. In order to calculate pressure drop after gas breaks through the foam bank, the characteristics that have passed beyond the edge of the foam bank r_f are ignored, because they do not contribute to the pressure difference. Therefore, the dimensionless position of the foam bank x_{D_f} is calculated relative to the outer radius of the reservoir in each layer (j) using equation (0.29)

$$x_{D_{f_j}} = \frac{r_{f_j}^2 - r_w^2}{r_e^2 - r_w^2} \quad (0.83)$$

For a specific volume of surfactant slug V_s , this value is constant for each layer (j). However, it changes for different surfactant slug sizes. x_{D_f} marks the boundary at which gas breaks through the foam bank. Similar to equation (0.45), the dimensionless position for the characteristics in the foam bank is given by

$$x_D(S_w) = \min\left(\left(t_D \frac{df_{w,f}(S_w)}{dS_w}\right), x_{D_f}\right) \quad (0.84)$$

The radial position r_{f_j} corresponding to this dimensionless position is calculated using equation (0.46). The water saturation is assumed to be $S_w=fmdry$. Within the boundary of the foam bank, a certain PV of gas t_{D_f} is injected into each layer (j) that is

$$t_{D_{f_j}} = \frac{\pi(r_{f_j}^2 - r_w^2)h_j\phi_j(1 - fmdry_j)}{\pi(r_e^2 - r_w^2)h_j\phi_j} = \frac{(r_{f_j}^2 - r_w^2)}{(r_e^2 - r_w^2)}(1 - fmdry_j) \quad (0.85)$$

The pressure drop in the foam bank (ΔP_f) is calculated using equation (0.76). Beyond the surfactant bank, a second displacement begins where gas displaces water at the initial condition ($S_w=1$) without surfactants. For simplicity, the injection condition J is assumed to be at $f_g=1$. There is a shock to I and a spreading wave behind it back to J where $S_w=S_{wc}$. The position of characteristics in this wave are given by

$$x_{D_2}(S_w) = \min\left(\left(x_{D_f} + (t_D - t_{D_f}) \frac{df_{w,g}(S_w)}{dS_w}\right), 1\right) \quad (0.86)$$

The dimensionless position of the foam bank is added to the first term in equation (0.86) in order for the radii of gas characteristics to start at the boundary where gas breaks through. The dimensionless time is modified

by subtracting the dimensionless time needed to fill the foam bank for a specific layer (j). The radii are calculated using equation (0.46). After gas breakthrough, three regions (banks) influence the pressure difference in each layer (j) (foam, gas, and water). Therefore, three equations are needed to calculate the pressure differences ΔP_f , ΔP_g , ΔP_w . The pressure difference in the water bank ahead of the gas bank is calculated using equation (0.49). The dimensionless pressure for every dimensionless time step (n) for layer (j) is

$$P_{D_j}^n = \frac{\Delta P_f + \Delta P_g + \Delta P_w}{\frac{Q}{2\pi kh\lambda_{rw}} \ln\left(\frac{r_e}{r_w}\right)} \quad (0.87)$$

Prior to gas breakthrough from the foam bank, the displacement is identical to gas injection into a fully surfactant-saturated reservoir as shown in **Figure 7**. After breakthrough, **Figure 8** and **Figure 9** show the above mentioned boundaries.

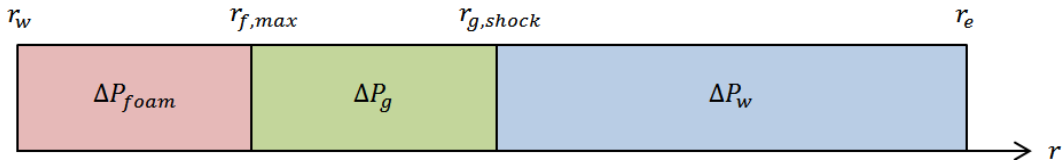


Figure 8: Radii for Boundaries after Gas Breakthrough

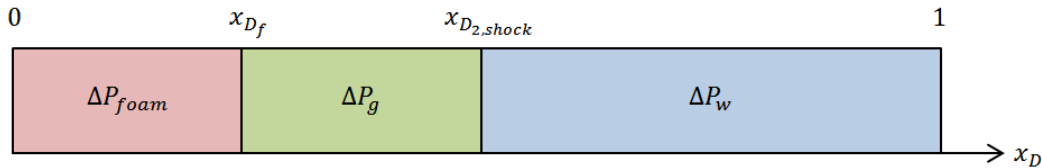


Figure 9: Dimensionless Positions after Gas Breakthrough

2.9. Pseudo Algorithm

In computer science, the pseudo codes are written in flow charts using symbols shown in **Figure 10**. In this paper, three algorithms are used for gas injection without surfactant, gas injection for a SAG process in fully surfactant-saturated layered reservoir, and gas injection for a SAG process with finite volume of surfactant slug, respectively. The third algorithm combines the first two to account for the pressure difference caused by gas after it breaks through the foam bank. In each case, the algorithm is divided into a Driver and a Function.

The total dimensionless time steps are logarithmic; the first total dimensionless time increment $\Delta t_D^{n=1}$ is in the order of $10^{-12} PV_{total}$. For the first total dimensionless time increment $\Delta t_D^{n=1}$, the dimensionless pressure $P_D=1$. The Driver calculates dimensionless time for each layer (j) $t_{D_j}^{n=1}$, i.e. how much volume each layer receives for the first step, as shown in equation (0.61). For every time step (n) and for each layer (j), the Driver sends the needed parameters (petrophysical, foam model, etc.) along with dimensionless time $t_{D_j}^n$ to the Function. The Function uses the fractional-flow theory to construct a saturation profile for every individual dimensionless time at every total dimensionless time step (n) for each layer (j) $t_{D_j}^n$. Additionally, the Function constructs the corresponding total relative mobility λ_{rt} profile and integrates it, as shown in equation (0.48), to predict the next dimensionless pressure $P_{D_j}^{n+1}$ that is sent back to the Driver. The Driver uses the kh -ratio and the predicted dimensionless pressures $P_{D_j}^{n+1}$ to calculate the next individual

dimensionless time for each layer (j) $t_{D_j}^{n+1}$ using equation (0.62). The process continues until the specified volume, $10 PV_{\text{total}}$ in this paper, is completely injected into the reservoir. Afterwards, the Driver calculates the cumulative injectivity ratio R_j^n . The actual algorithms can be found in the Appendix C, and the pseudo algorithms are shown in **Figure 11** through **Figure 16**.


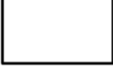
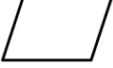

Flow Chart Symbols	
	Start /Stop
	Main Computation Step
	Input/Output
	Decision Point

Figure 10: Flow Chart Symbols

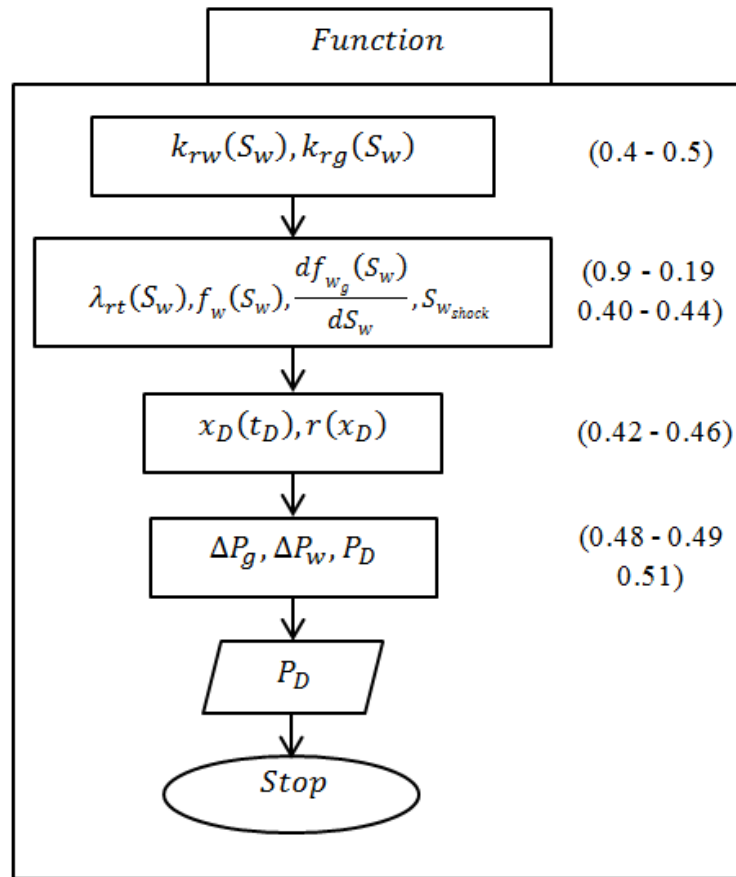


Figure 11: Function, Gas Injection Case (No Surfactant)

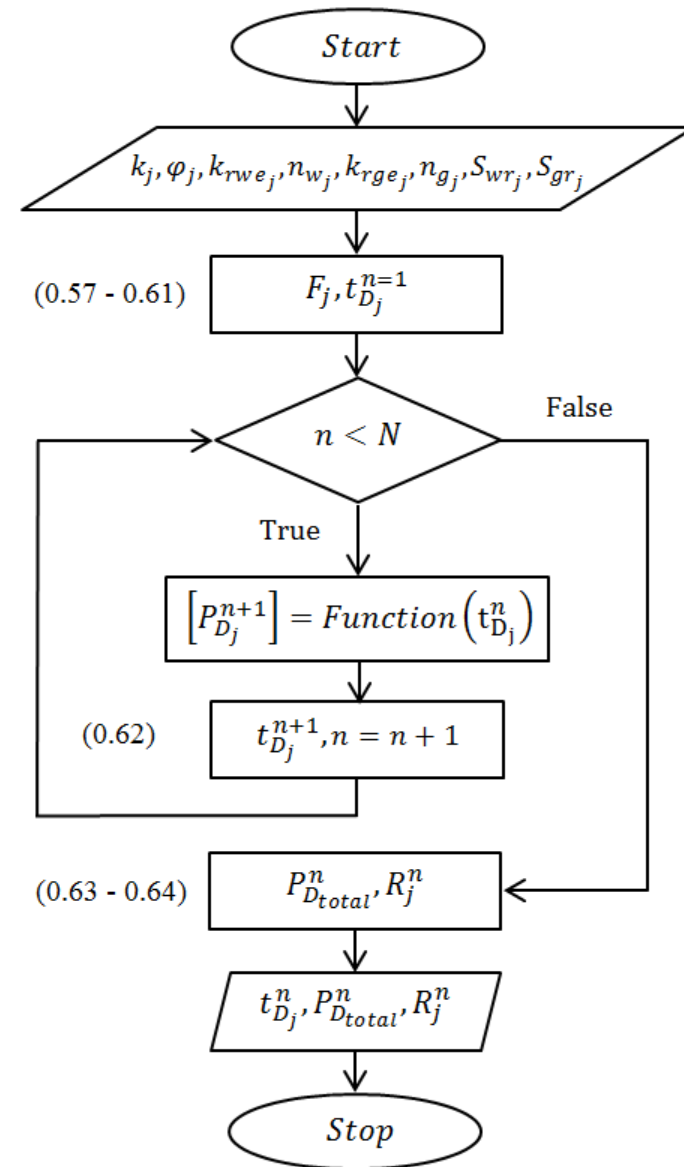


Figure 12: Driver, Gas Injection Case (No Surfactant)

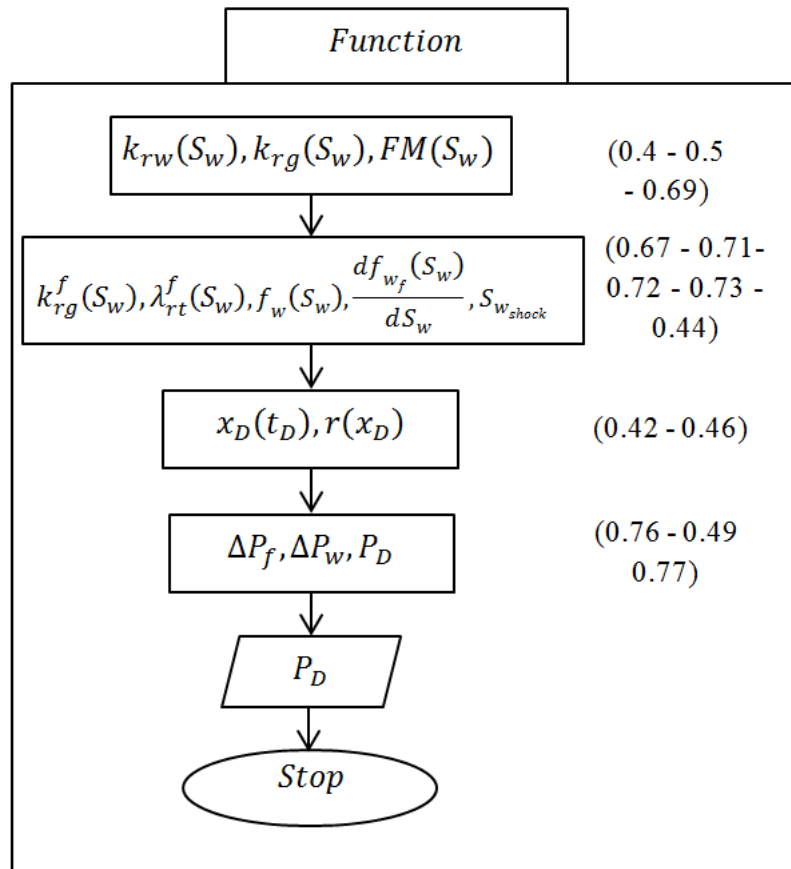


Figure 13: Function, SAG in Surfactant Saturated Reservoir

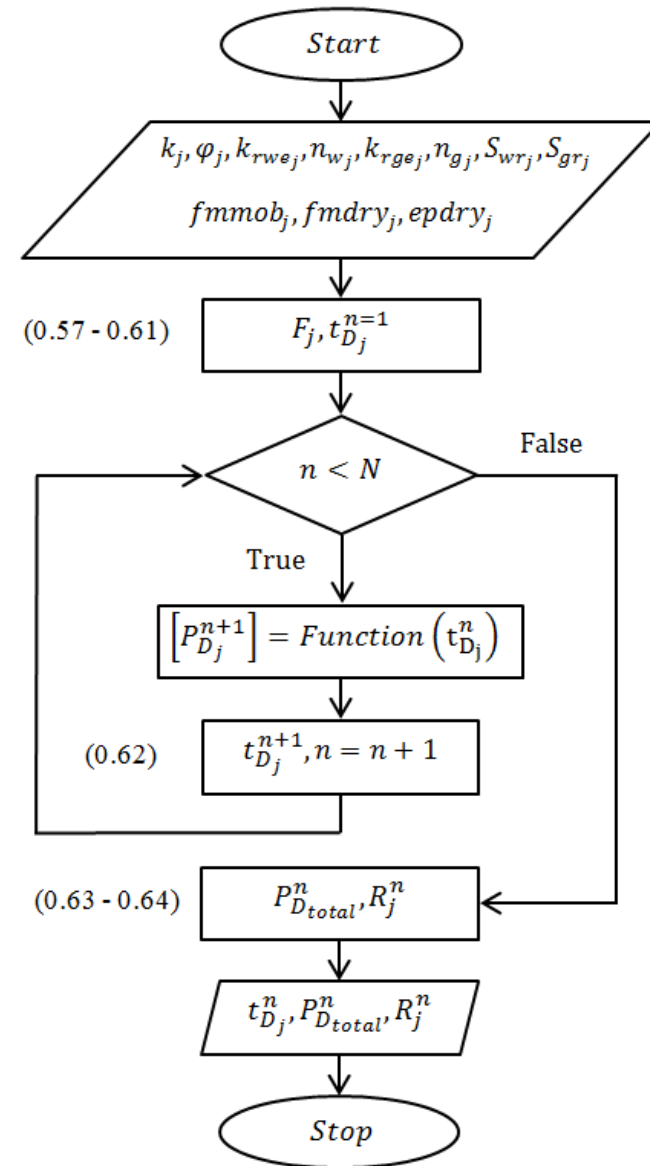


Figure 14: Driver, SAG in Surfactant Saturated Reservoir

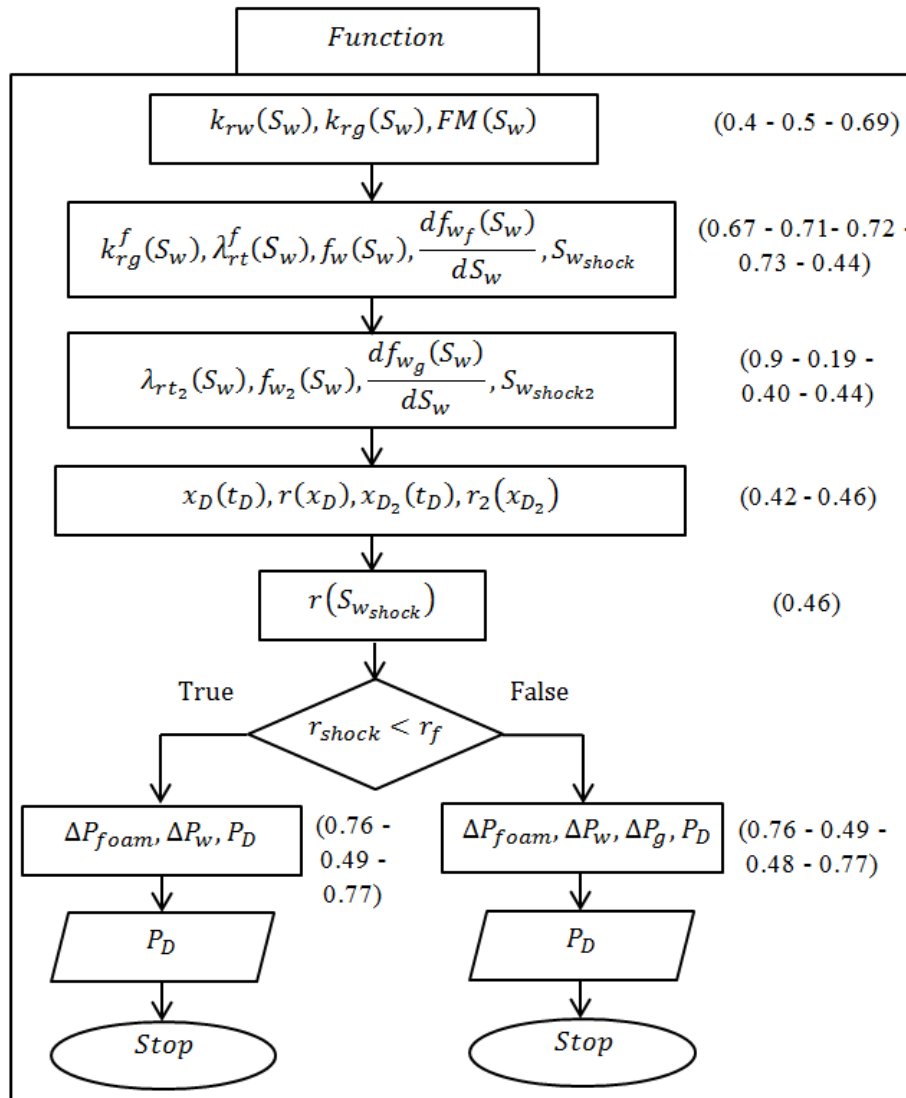


Figure 15: Function, SAG in Discrete Surfactant Slugs

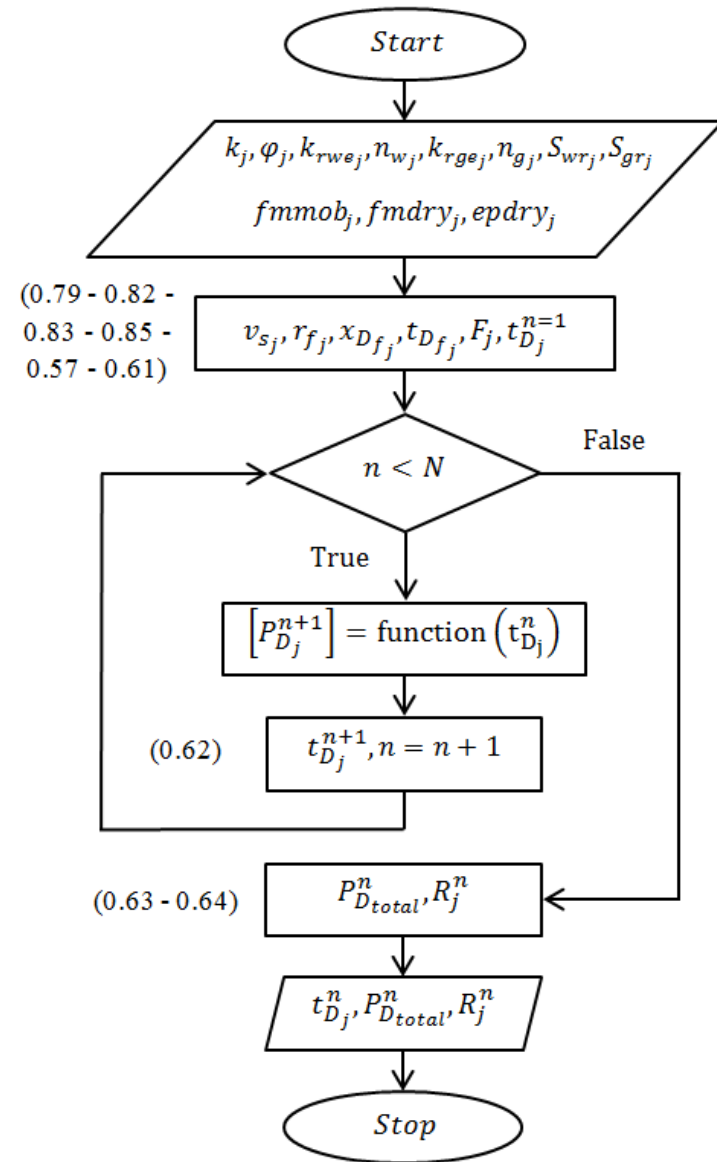


Figure 16: Main, SAG in Discrete Surfactant Slugs

2.10. Validity of the Model

In general, analytical solutions are based on various simplifying assumptions involving the idealized depiction of a reservoir. For example, a classification of flow as steady state is highly idealized, and in reality a reservoir is nearly always in a continuous pressure transient situation. Although these idealizations are rarely encountered in the real world, the solutions are instrumental in visualizing the dynamics of flow in the porous media and the overall reservoir behaviour. In this section, the limitations, assumptions, and range of validity of the used models are discussed.

The models used here are one-dimensional. Therefore, they cannot capture fingering or gravity effects that occur in 2D and 3D flows. Mobility ratio for gas injection without surfactants is unfavourable ($M > 1$) in all layers as shown in [Table 7](#); this indicates that the injected gas would finger through the water bank at initial conditions. In real reservoirs, the pressure drop due to gas injection into a water bank is lower than that predicted by the one-dimensional model due to viscous fingering and gravity override. Moreover, for SAG processes, the mobility ratio at the front is favourable ($M < 1$) as shown in [Table 7](#); this indicates that fingering at the flood front, where mobility control is maintained, is not likely. However, there can be fingering within the foam bank, where mobility increases toward the injection well. Whether fingering in the foam bank is important is an on-going topic of research.

Additionally, the model ignores gravity. Since there is less hydrostatic pressure to overcome at the top of the reservoir, gas propagates faster there as shown in [Figure 17](#). Gravity override occurs due to a competition between gravity (due to density differences) and horizontal pressure gradients. The horizontal pressure gradient is a crucial factor in controlling gravity override in SAG processes. If injection rate and injection pressure are sufficiently high, gravity override is less severe (Boeije & Rossen, 2013).

The foam model contains different functions that control foam behaviour by modifying the FM factor as shown in equation (0.68). F_1 models the effect of surfactant concentration; in our case, we simply assume that surfactant concentration is higher than CMC and is constant wherever the surfactant has flooded. F_2 or F_w models the effect of water saturation, which is thoroughly investigated in our research. F_3 models the effect of oil saturation; this has a detrimental effect on foam strength, but is ignored in this research for simplicity. Also, the foam scans in Kapetas et al. (2015) were conducted for foam without oil. In the vicinity of near-wellbore region, the combination of surfactant and gas injection drives oil saturation to very low values, which in that case can be ignored. F_4 models the effect of gas velocity; in the high quality regime the pressure gradient is independent of gas velocity (u_g); therefore, it is ignored. F_5 models the effect of capillary number; the function takes into account the shear-thinning rheology of foam. Since the high-quality regime is generally Newtonian, the effect of capillary number is ignored. In the models used here, gas diversion in a SAG process is independent of flow rate or pressure gradient. This could be challenged since high-quality foam can be shear-thinning.

Although foam scans were carried for sandstone formations that are similar in porosities and residual saturations, one would like to use cores taken from the same formation with ranging permeabilities. The foam scans were carried out at room temperature; therefore, the foam model parameters may not be fully representative at reservoir conditions. Although surfactant-formulation controls the effect of temperature on foam, foam mobility is generally higher at higher temperatures. The foam scans by Kapetas et al. (2015) show strong foams; in field applications, foam is likely to be less strong (more mobile). Furthermore, petrophysical data along with Corey parameters were measured for different cores than the ones used for the foam scans. Although the samples were taken from the same formation, there was a noticeable variation in permeability as shown in [Table 9](#). The difference in permeability might affect the model fit parameters.

However, it is expected that relative permeability is not very sensitive to permeability, and therefore the relative-permeability curves apply.

Another problem for modelling SAG processes with confidence is that they occur at very low water fractional-flow f_w values (Rossen and Boeije, 2015). However, current foam scans generally lack density of data at this range leading to uncertainties regarding the model fit. Unfortunately, grossly different results are predicted depending on how these data are extrapolated to very low f_w (Rossen and Boeije, 2015). The scarcity of data at high f_g values, in the foam scans used here, is displayed in **Figure 150** in Appendix B. Additionally, the foam model parameters, for the Bandera Gray formation, do not fit the foam scan data properly as shown in **Figure 150**. However, it is used here to illustrate cases with extreme permeability contrast.

Due to the simplifying assumption, the application of fractional-flow theory for foam has some disadvantages. FFT is approximate when applied to compressible phases, which may be slow to reach their steady-state mobilities. If the period of foam generation is significant on reservoir scale, then modelling foam using FFT would be invalid. Furthermore, capillarity is not ignored in the models used here since it is accounted for in Corey relative-permeability functions, k_{rw} and k_{rg} . However, gradient of capillary pressure is ignored since the viscous pressure gradient is much larger than the capillary pressure gradient in the field. The models used here do not account for diffusion or adsorption; the effects might be important since the predicted optimal slug size results in small foam banks in the near wellbore region. In field applications, the predicted optimal surfactant slug sizes need to be larger to account for diffusion or adsorption. The displacement is also assumed to be immiscible. For nitrogen foams, this is a very good assumption, because the dissolvability of the gas phase into the liquid phase and vice versa is very small.

Uniform initial condition is assumed here. However, if gas is present initially, the surfactant slug will slump down during injection and the problem of gravity override is more severe. After gas breakthrough the foam bank, gas is modelled using FFT with an injection of $f_g = 1$. This is a simplifying assumption that allows for a continuous solution. The error is expected to be minimal since the pressure drop in the foam bank is orders of magnitude higher than that caused by gas displacement. Water evaporation in the near wellbore region due to gas injection is also ignored. Since evaporation increases the gas relative-permeability, the effect is dependent on the range of values of gas relative-permeability. Moreover, the minimum resolution in our scheme is 0.5 m. Such resolution can hardly be obtained using conventional reservoir simulators. This gives an advantage of the FFT over the Peaceman equation commonly used in reservoir simulators (Leefink et al., 2013).

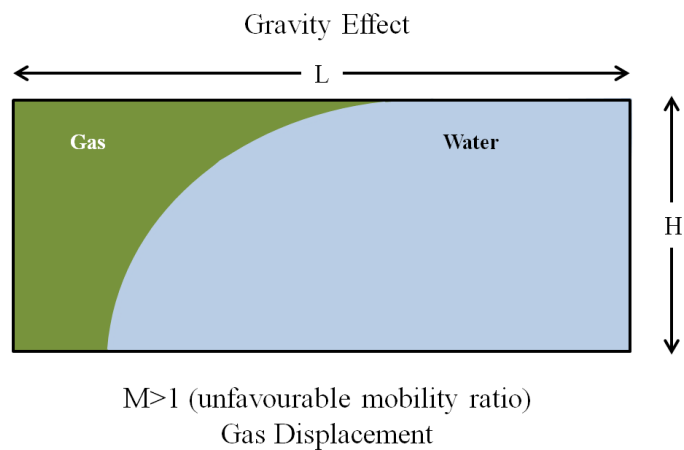


Figure 17: Gravity Override Due to Density Differences for $M > 1$

3 Results

The results of the following scenarios are shown here.

- I. Base Case: gas injection without surfactant
- II. Surfactant saturated reservoir
 - A. STARS Model
 - B. Namdar Zanganeh et al. (2011) modification
- III. Discrete Surfactant Slug Size
 - A. STARS Model
 - B. Namdar Zanganeh et al. (2011) modification
- IV. No Surfactant Injection into Bandera Gray
 - A. All other layers are fully Saturated
 - i. STARS Model
 - ii. Namdar Zanganeh et al. (2011) modification
 - B. Discrete Surfactant Slug Size
 - i. STARS Model
 - ii. Namdar Zanganeh et al. (2011) modification

For the different scenarios investigated, the results are displayed in four different graphs.

1. Injectivity Ratio (R_i^n) vs. Total Pore Volume Injected ($t_{D_{total}}$)

This graph displays the ratio of cumulative flow into each layer out of the total pore volume injected $t_{D_{total}}$ on a semi-log plot. The starting value for each layer (j) is equivalent to the kh -ratio for that layer. The graph displays how injectivity changes overtime based on mobilities predicted by the model.

2. Individual Pore Volume Received (t_{D_i}) vs. Total Pore Volume injected ($t_{D_{total}}$)

This graph is shown for 3 total pore volumes injected $t_{D_{total}}$, and describes how much each layer receives in each scenario.

3. The average dimensionless pressure ($P_{D_{total}}$) vs. Total Pore Volume injected ($t_{D_{total}}$)

This graph displays the average dimensionless pressure of all layers $P_{D_{total}}$ as it changes with total pore volume injected $t_{D_{total}}$. This is an indication of injectivity; values above 1 indicate that the injected fluid experiences more resistance than water injection in a water-saturated reservoir and vice versa. This is displayed in a semi-logarithmic plot.

4. Total Pore Volume injected ($t_{D_{total}}$) vs. Relative Injection Time

This graph displays the time it take to inject one reservoir pore volume of gas relative to the time it would take to inject the same volume of water in water-saturated reservoir, i.e. with $S_w=1$.

I. Base Case: Gas Injection without Surfactant

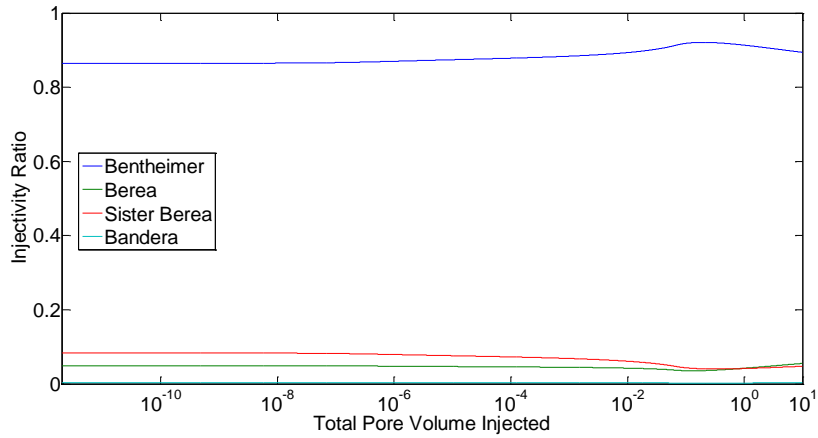


Figure 18: Injectivity Ratio vs. Total logarithmic PV Injected (Base Case)

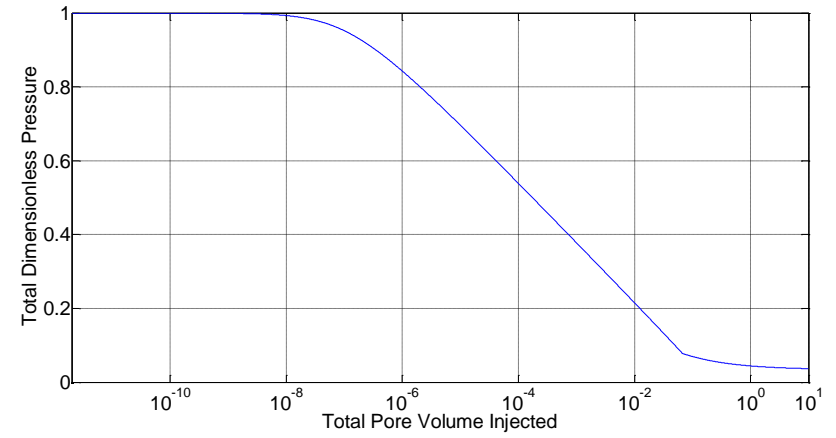


Figure 20: Total Dimensionless Pressure vs. Total Pore Volume injected (Base Case)

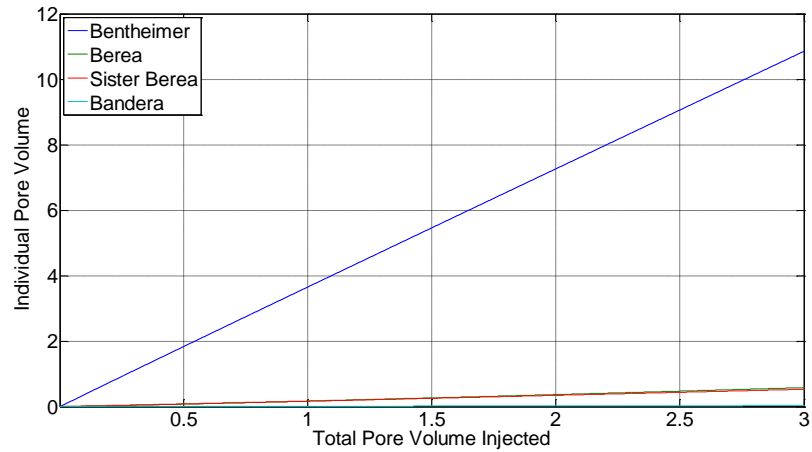


Figure 19: Individual Pore Volume vs. Total Pore Volume of Gas injected (Base Case)

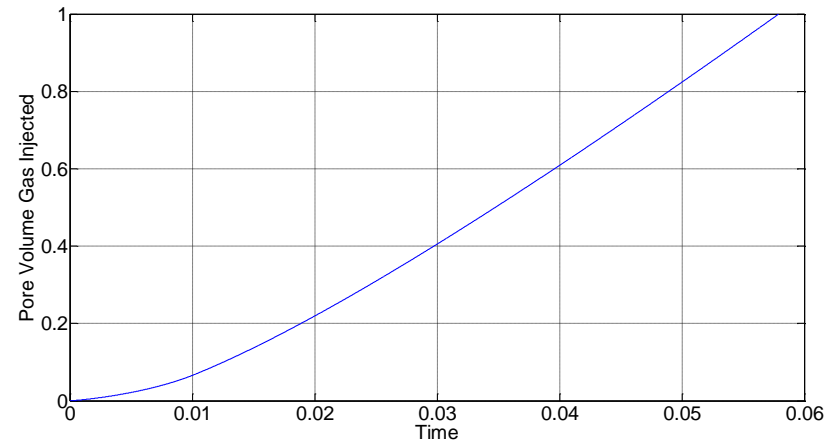


Figure 21: Relative Injection Time vs. PV of Gas Injected (Base Case)

II. Surfactant-Saturated Reservoir (A.STARS Model)

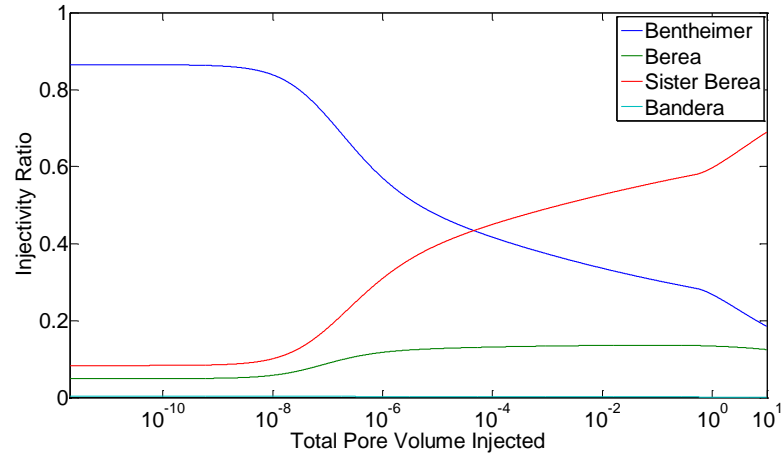


Figure 22: Injectivity Ratio vs. log of Total Pore Volumes (Case II.A)

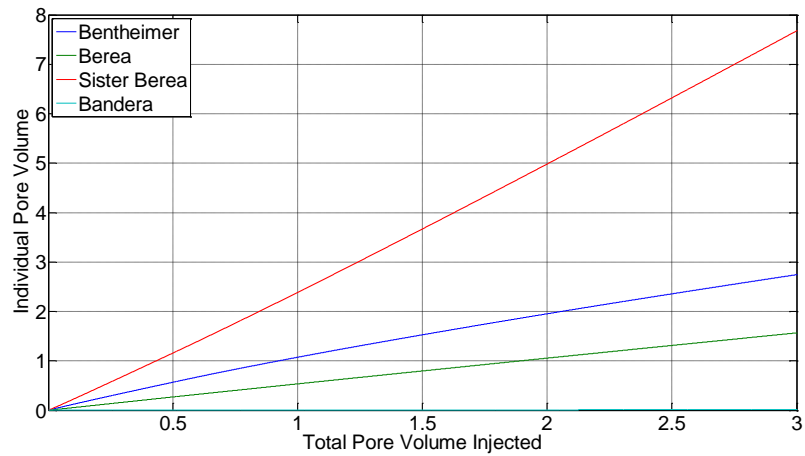


Figure 23: Individual Pore Volume vs. Total Pore Volume of Gas injected (Case II.A)

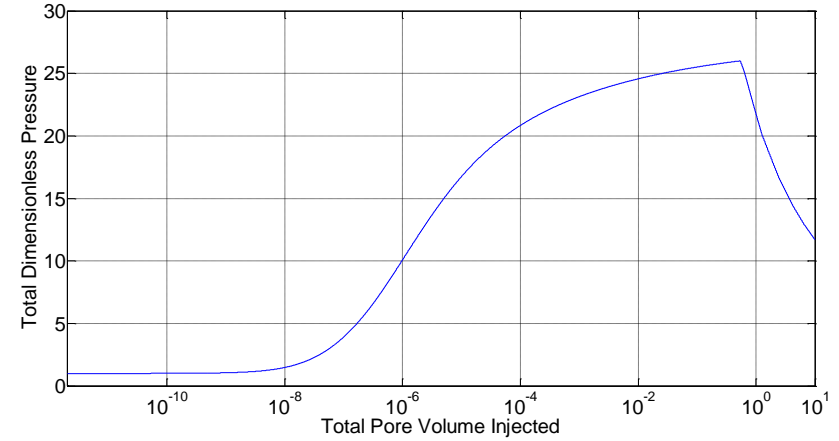


Figure 24: Total Dimensionless Pressure vs. Total Pore Volume Injected (Case II.A)

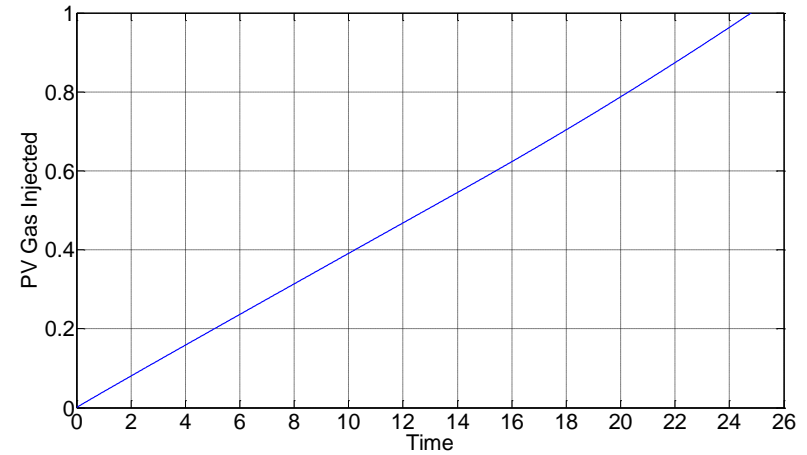


Figure 25: Relative Injection Time vs. PV of Gas Injected (Case II.A)

II. Surfactant-Saturated Reservoir (B. Namdar Zanganeh et al. Modified Model)

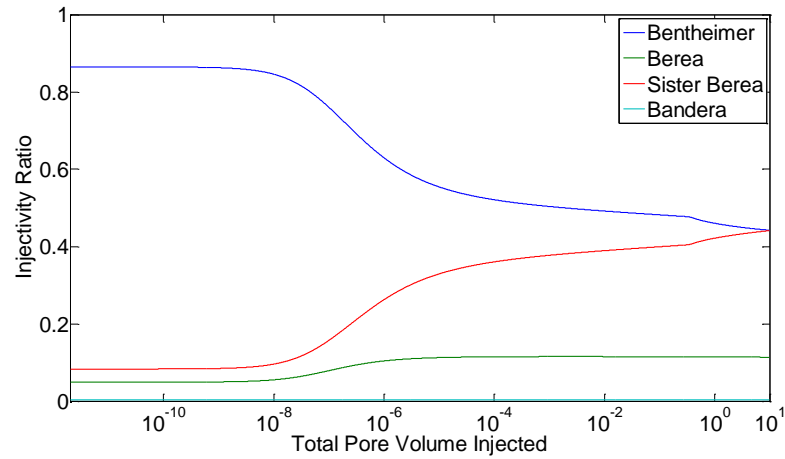


Figure 26: Injectivity Ratio vs. log of Total Pore Volumes (Case II.B)

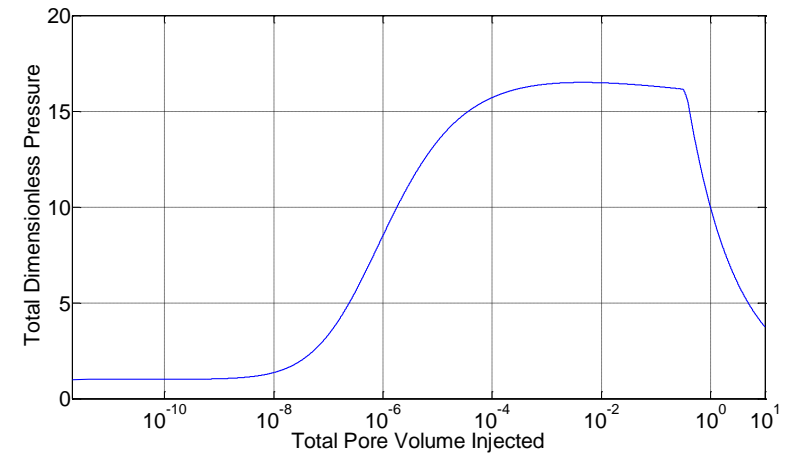


Figure 28: Total Dimensionless Pressure vs. Total Pore Volume Injected (Case II.B)

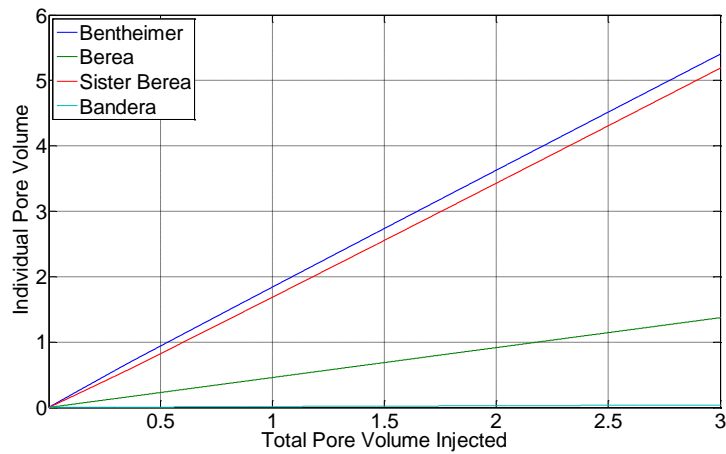


Figure 27: Individual Pore Volume vs. Total Pore Volume of Gas injected (Case II.B)

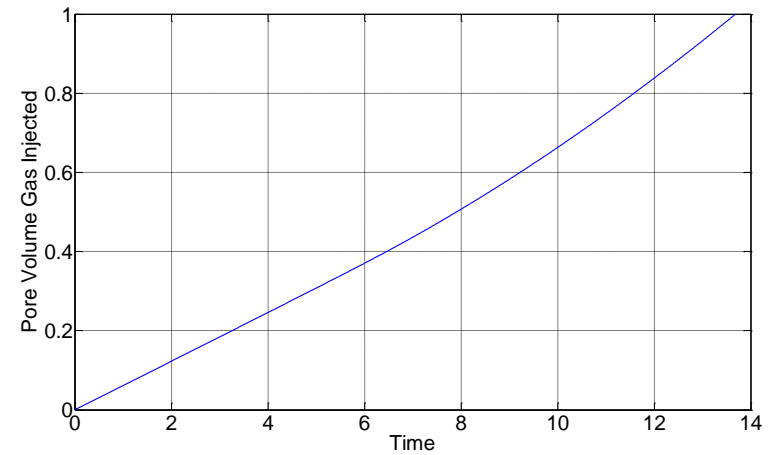


Figure 29: Relative Injection Time vs. PV of Gas Injected (Case II.B)

III. Discrete Surfactant Slug Sizes (A. STARS Model)

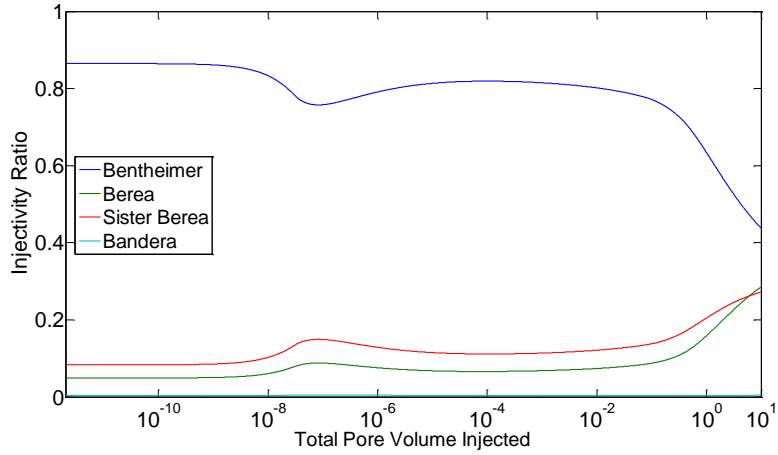


Figure 30: Injectivity Ratio vs. Total Pore Volume of Gas injected ($V_s=1.0^{-8}$) (Case III.A)

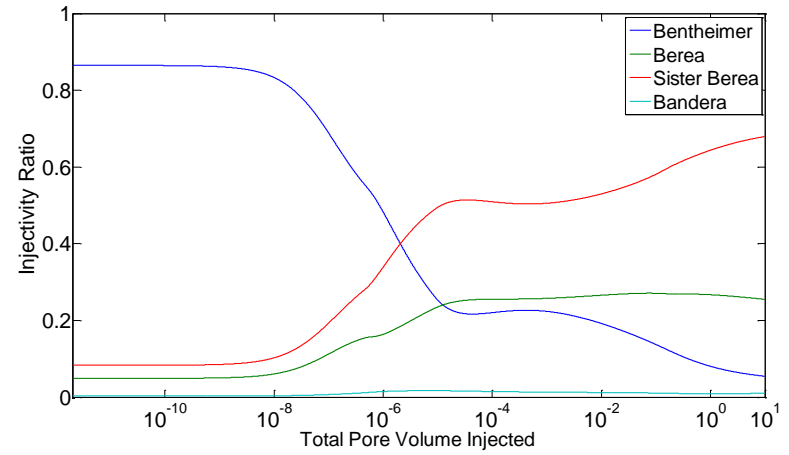


Figure 32: Injectivity Ratio vs. Total Pore Volume of Gas injected ($V_s=1.0^{-6}$) (Case III.A)

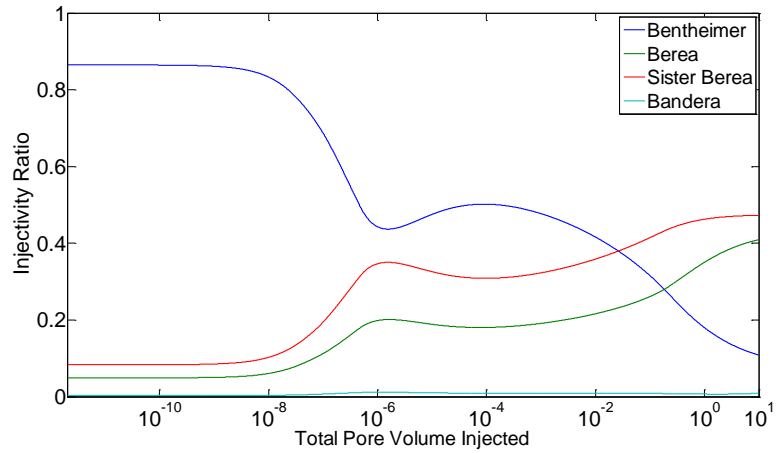


Figure 31: Injectivity Ratio vs. Total Pore Volume of Gas injected ($V_s=1.0^{-7}$) (Case III.A)

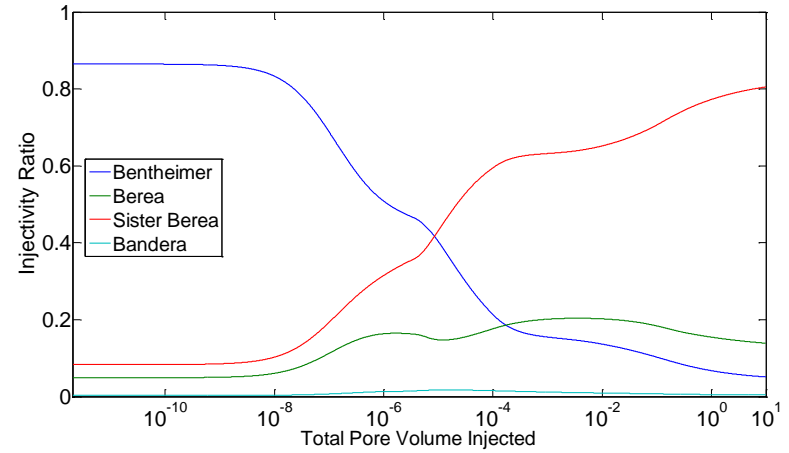


Figure 33: Injectivity Ratio vs. Total Pore Volume of Gas injected ($V_s=1.0^{-5}$) (Case III.A)

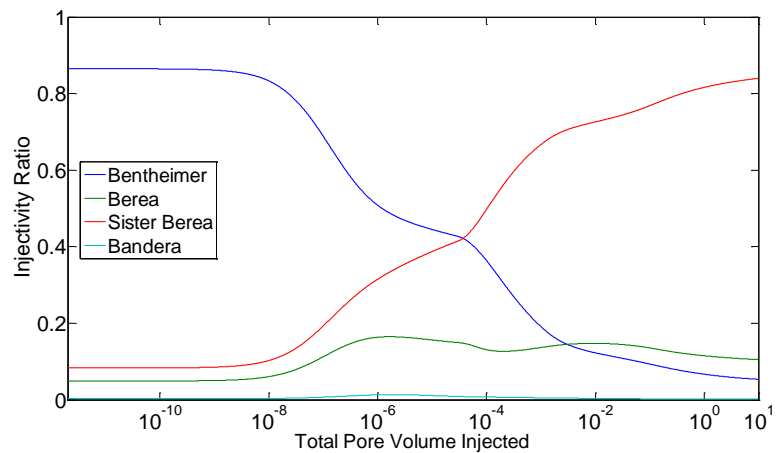


Figure 34: Injectivity Ratio vs. Total Pore Volume of Gas injected ($V_s=1.0^{-4}$) (Case III.A)

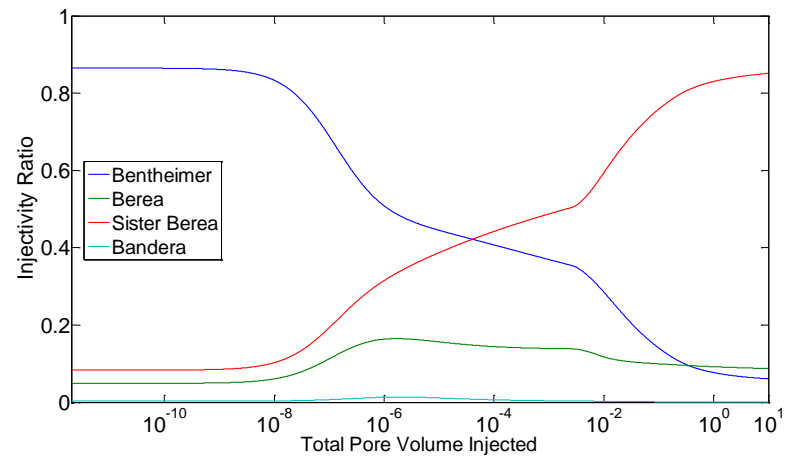


Figure 36: Injectivity Ratio vs. Total Pore Volume of Gas injected ($V_s=1.0^{-2}$) (Case III.A)

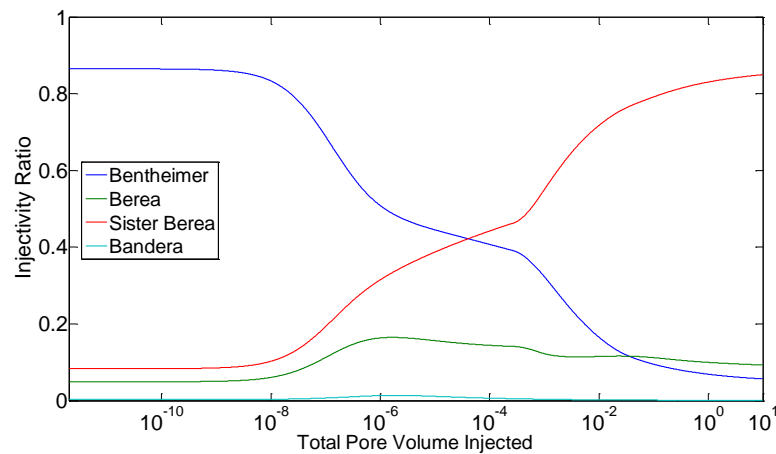


Figure 35: Injectivity Ratio vs. Total Pore Volume of Gas injected ($V_s=1.0^{-3}$) (Case III.A)

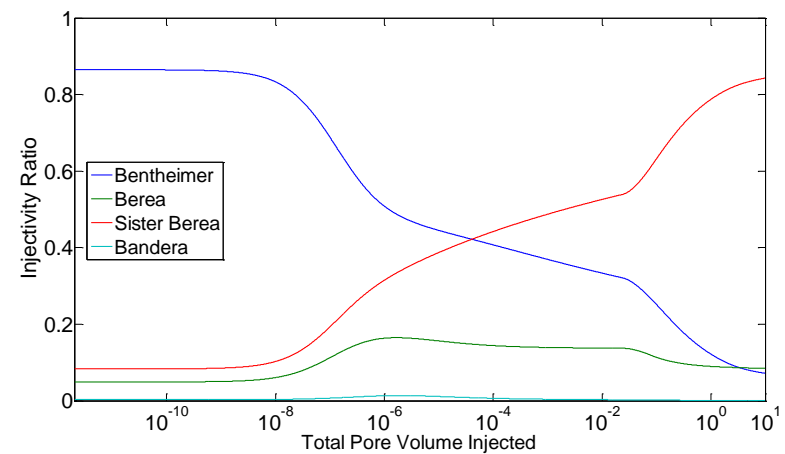


Figure 37: Injectivity Ratio vs. Total Pore Volume of Gas injected ($V_s=1.0^{-1}$) (Case III.A)

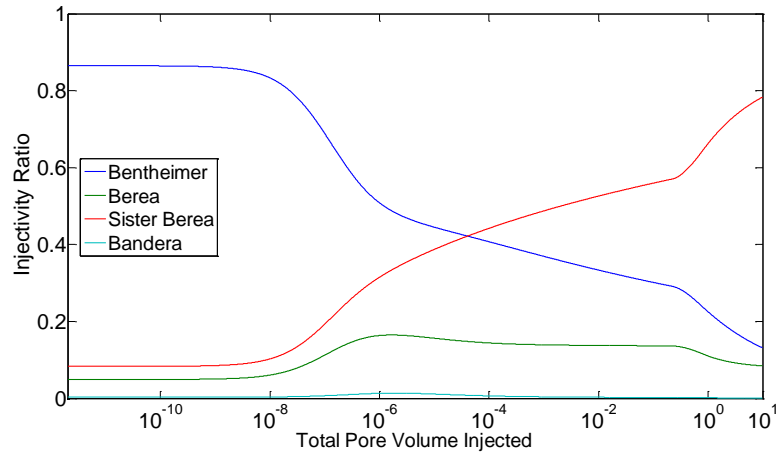


Figure 38: Injectivity Ratio vs. Total Pore Volume of Gas injected ($V_s=1.0$) (Case III.A)

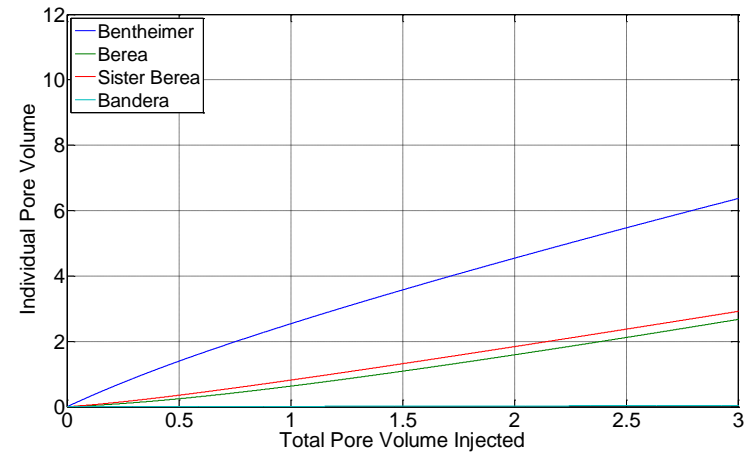


Figure 40: Individual Pore Volume vs. Total Pore Volume of Gas injected ($V_s=1.0^{-8}$) (Case III.A)

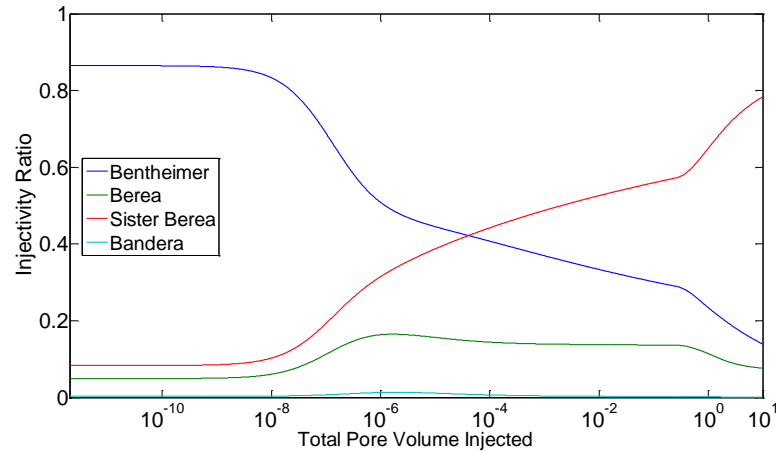


Figure 39: Injectivity Ratio vs. Total Pore Volume of Gas injected ($V_s=10.0$) (Case III.A)

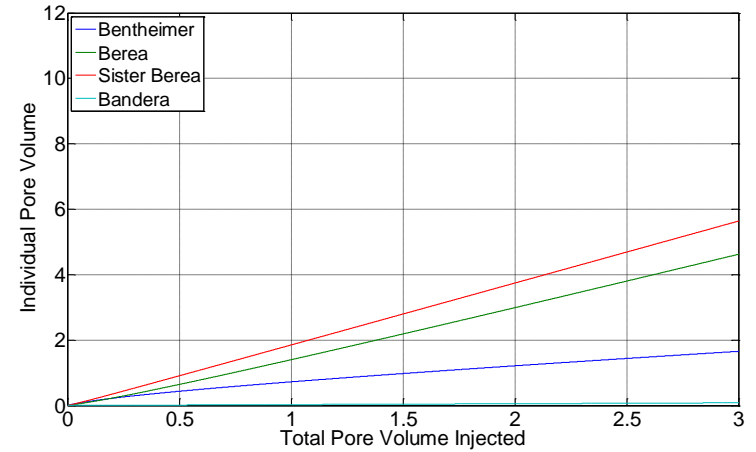


Figure 41: Individual Pore Volume vs. Total Pore Volume of Gas injected ($V_s=1.0^{-7}$) (Case III.A)

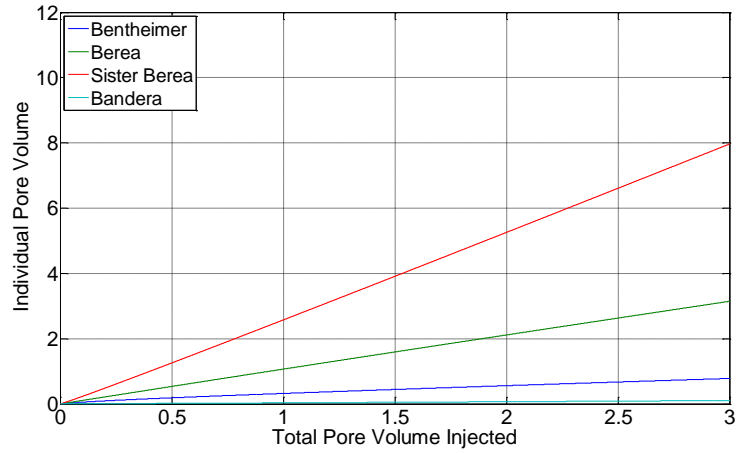


Figure 42: Individual Pore Volume vs. Total Pore Volume of Gas injected ($V_s=1.0^{-6}$) (Case III.A)

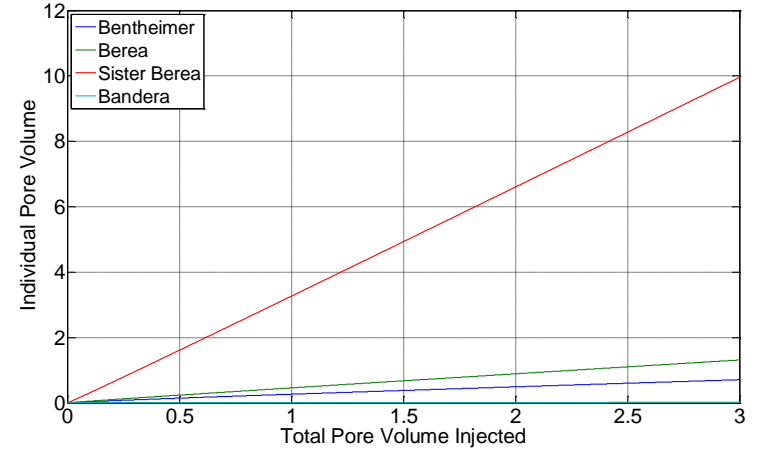


Figure 44: Individual Pore Volume vs. Total Pore Volume of Gas injected ($V_s=1.0^{-4}$) (Case III.A)

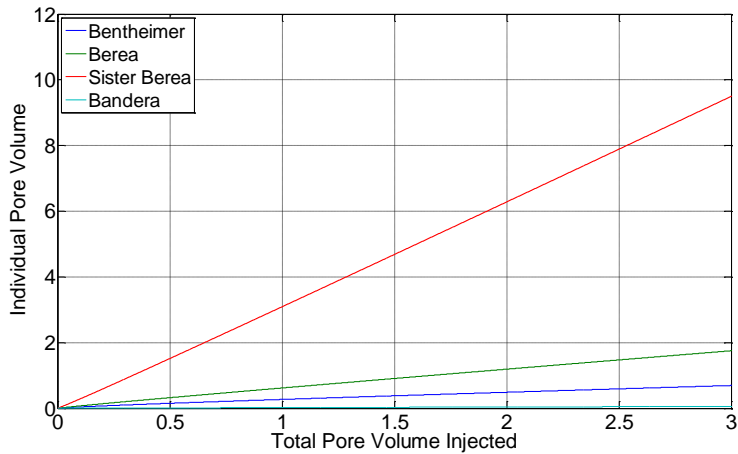


Figure 43: Individual Pore Volume vs. Total Pore Volume of Gas injected ($V_s=1.0^{-5}$) (Case III.A)

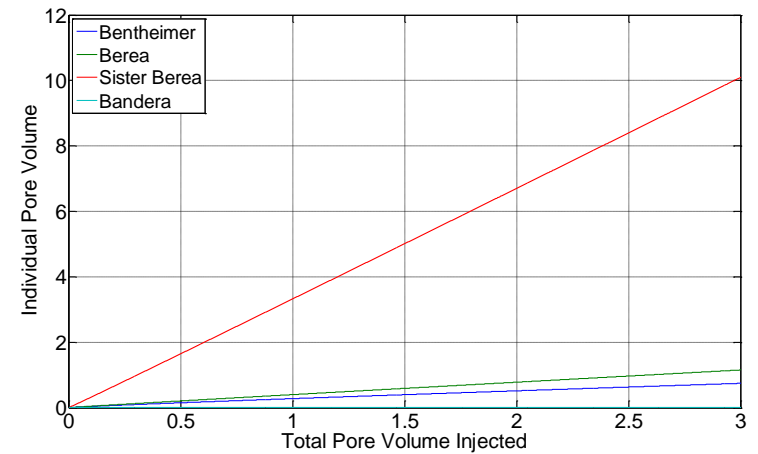


Figure 45: Individual Pore Volume vs. Total Pore Volume of Gas injected ($V_s=1.0^{-3}$) (Case III.A)

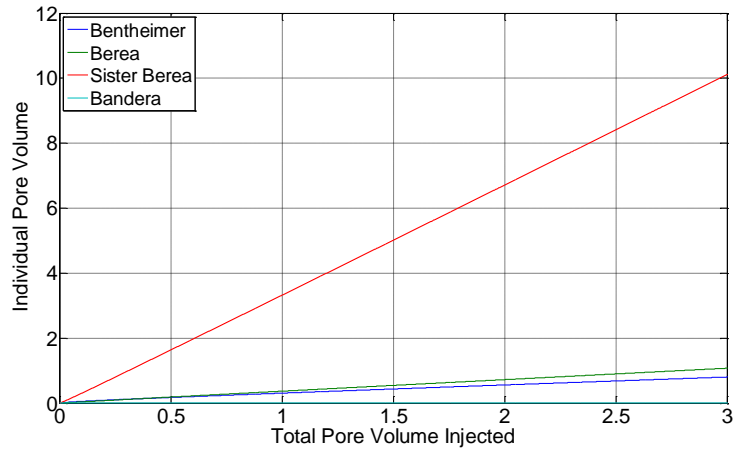


Figure 46: Individual Pore Volume vs. Total Pore Volume of Gas injected ($V_s=1.0^{-2}$) (Case III.A)

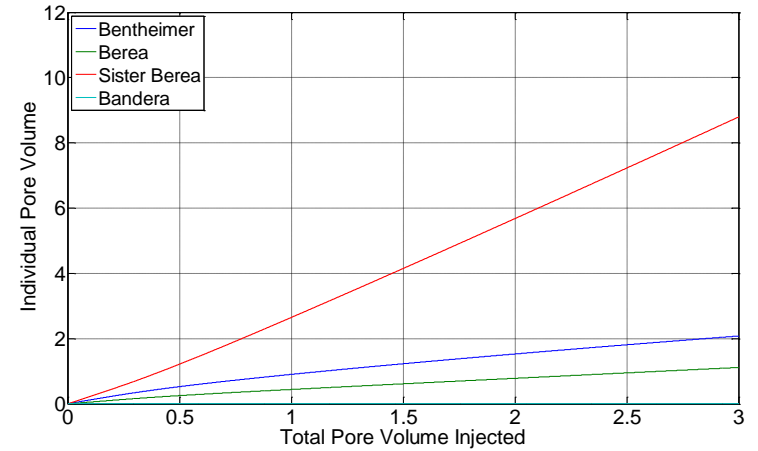


Figure 48: Individual Pore Volume vs. Total Pore Volume of Gas injected ($V_s=1.0$) (Case III.A)

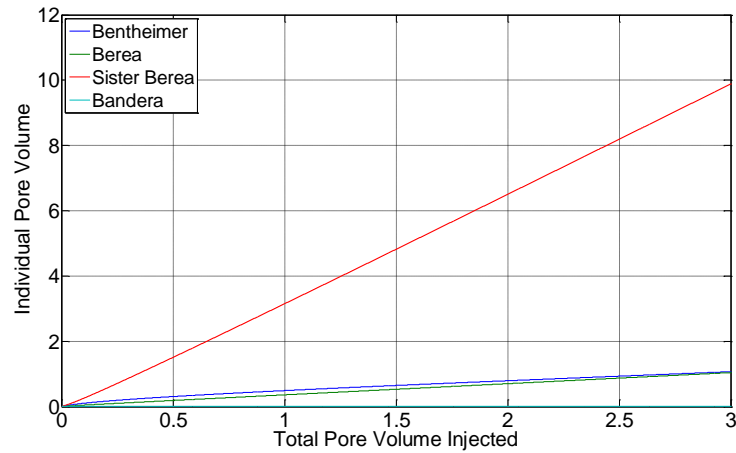


Figure 47: Individual Pore Volume vs. Total Pore Volume of Gas injected ($V_s=1.0^{-1}$) (Case III.A)

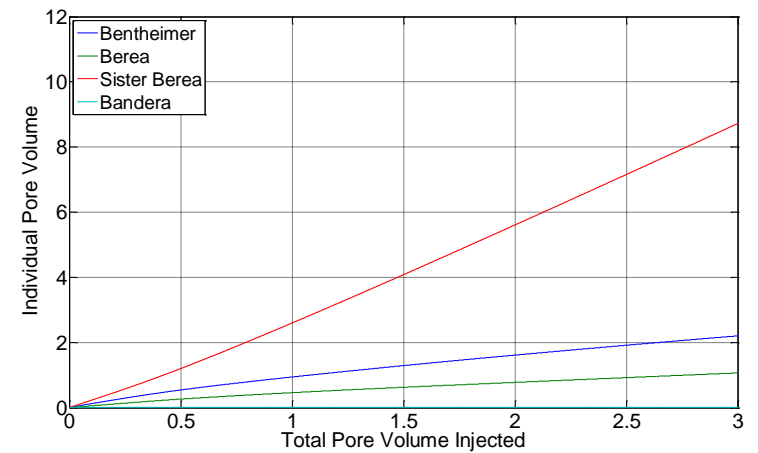


Figure 49: Individual Pore Volume vs. Total Pore Volume of Gas injected ($V_s=10.0$) (Case III.A)

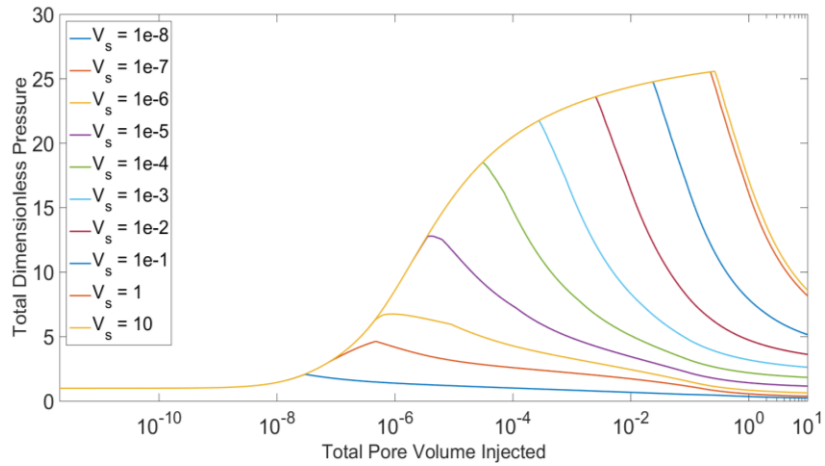


Figure 50: Total Dimensionless Pressure vs. Total Pore Volume Injected for Different Surfactant Slug Sizes (Case III.A)

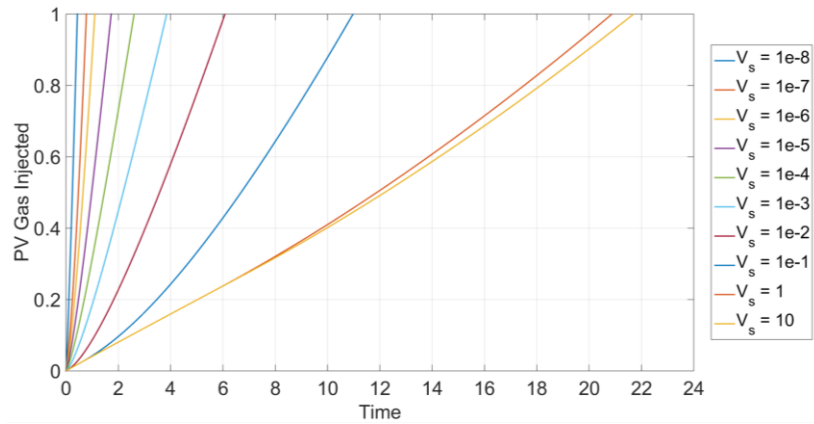


Figure 51: Relative Injection Time vs. PV of Gas Injected for Various Surfactant-Slug Sizes (Case III.A)

III. Discrete Surfactant Slug Sizes (B. Namdar Zanganeh et al. Modified Model)

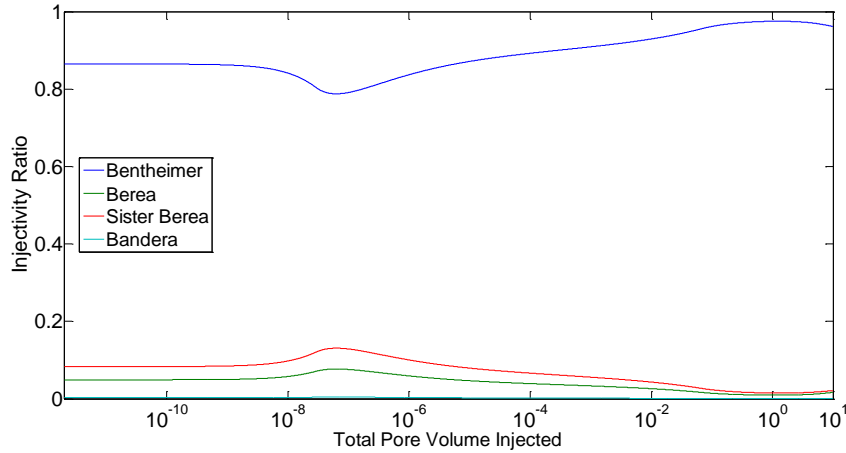


Figure 52: Injectivity Ratio vs. Total Pore Volume of Gas injected ($V_s=1.0^{-8}$) (Case III.B)

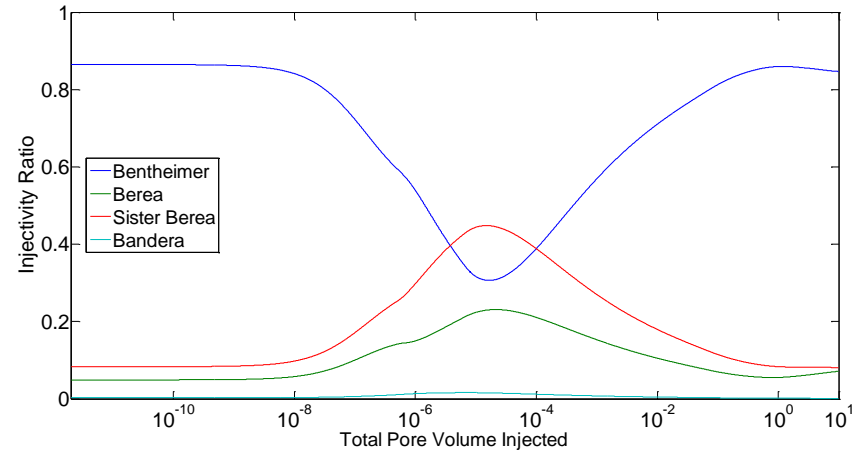


Figure 54: Injectivity Ratio vs. Total Pore Volume of Gas injected ($V_s=1.0^{-6}$) (Case III.B)

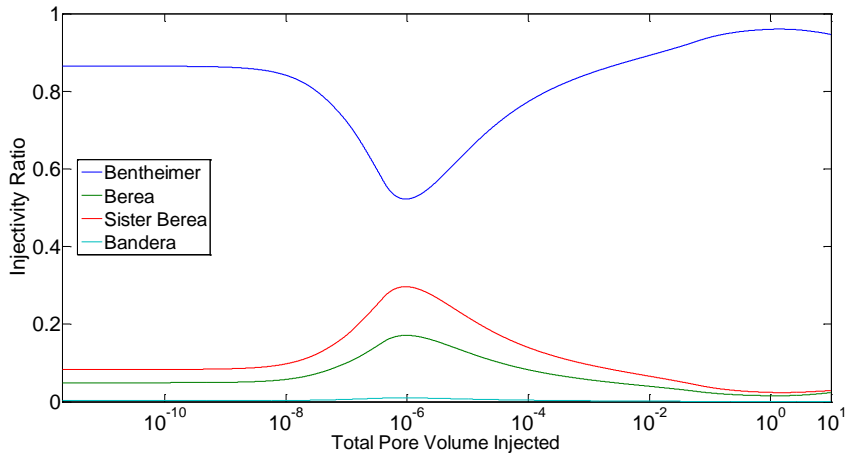


Figure 53: Injectivity Ratio vs. Total Pore Volume of Gas injected ($V_s=1.0^{-7}$) (Case III.B)

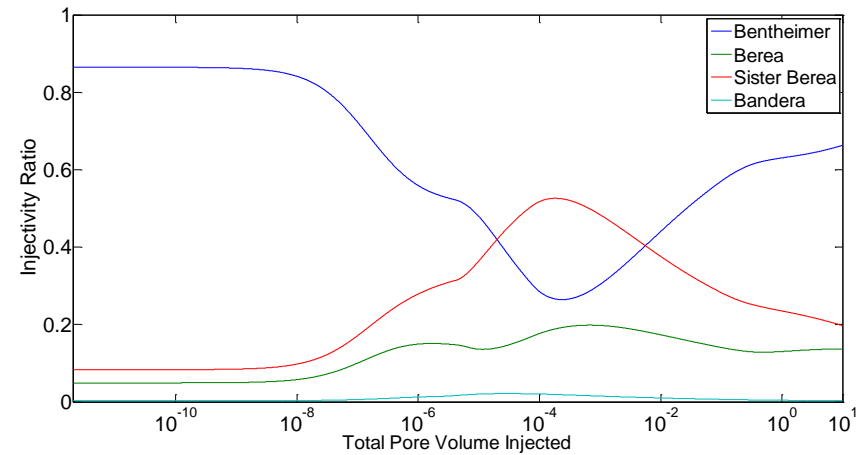


Figure 55: Injectivity Ratio vs. Total Pore Volume of Gas injected ($V_s=1.0^{-5}$) (Case III.B)

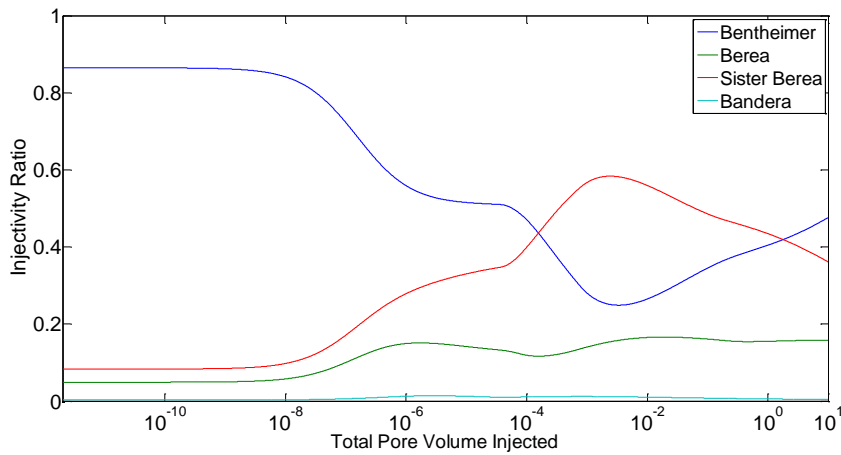


Figure 56: Injectivity Ratio vs. Total Pore Volume of Gas injected ($V_s=1.0^{-4}$) (Case III.B)

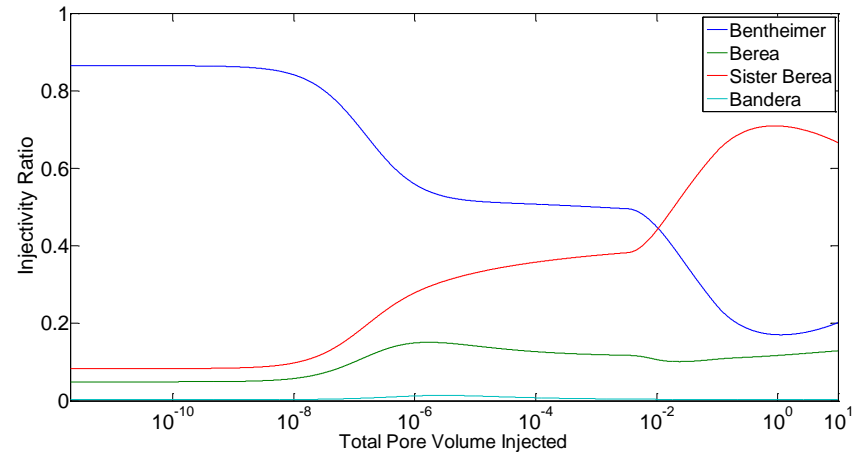


Figure 58: Injectivity Ratio vs. Total Pore Volume of Gas injected ($V_s=1.0^{-2}$) (Case III.B)

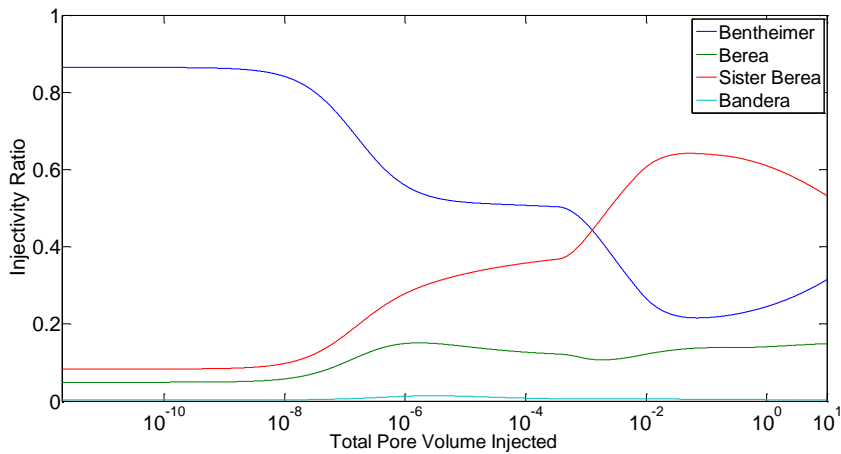


Figure 57: Injectivity Ratio vs. Total Pore Volume of Gas injected ($V_s=1.0^{-3}$) (Case III.B)

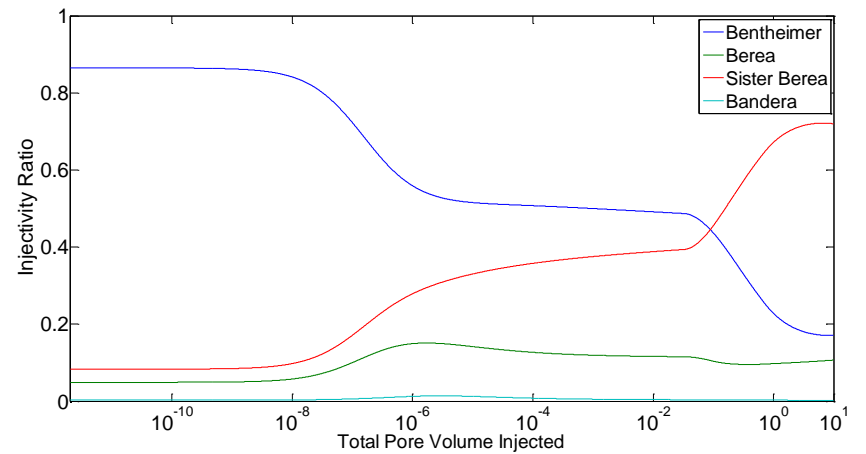


Figure 59: Injectivity Ratio vs. Total Pore Volume of Gas injected ($V_s=1.0^{-1}$) (Case III.B)

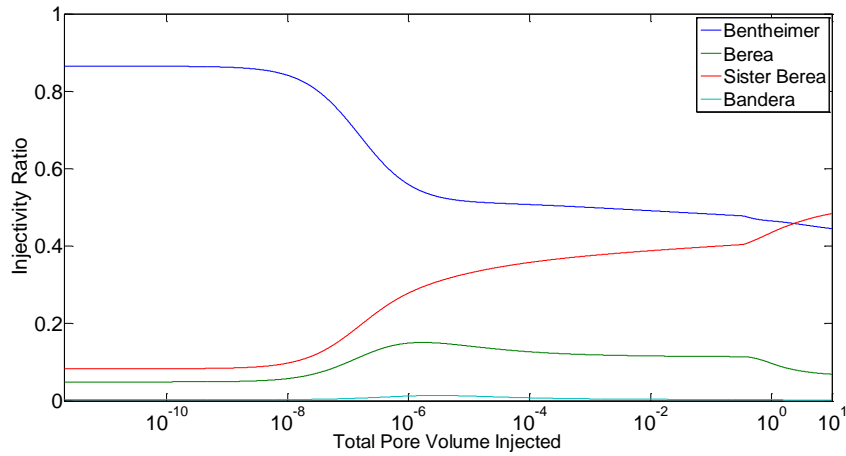


Figure 60: Injectivity Ratio vs. Total Pore Volume of Gas injected ($V_s=1.0$) (Case III.B)

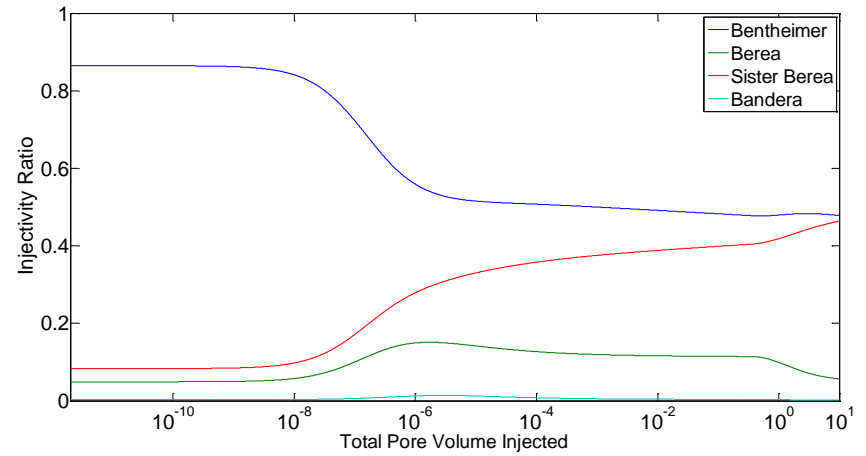


Figure 61: Injectivity Ratio vs. Total Pore Volume of Gas injected ($V_s=10.0$) (Case III.B)

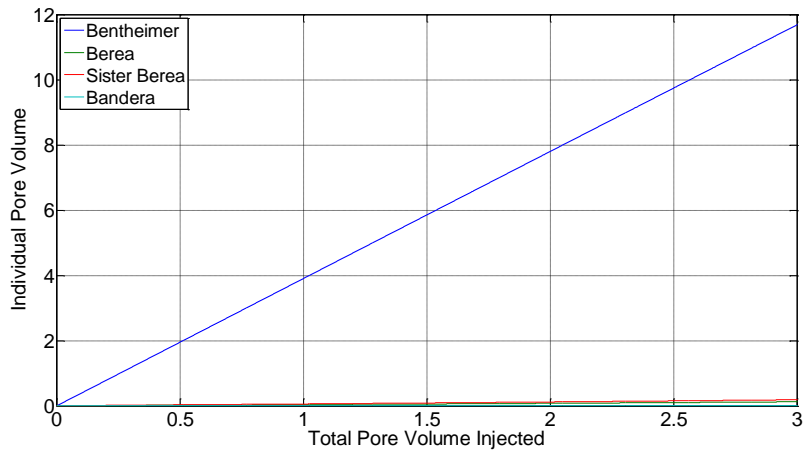


Figure 62: Individual Pore Volume vs. Total Pore Volume of Gas injected ($V_s=1.0^{-8}$) (Case III.B)

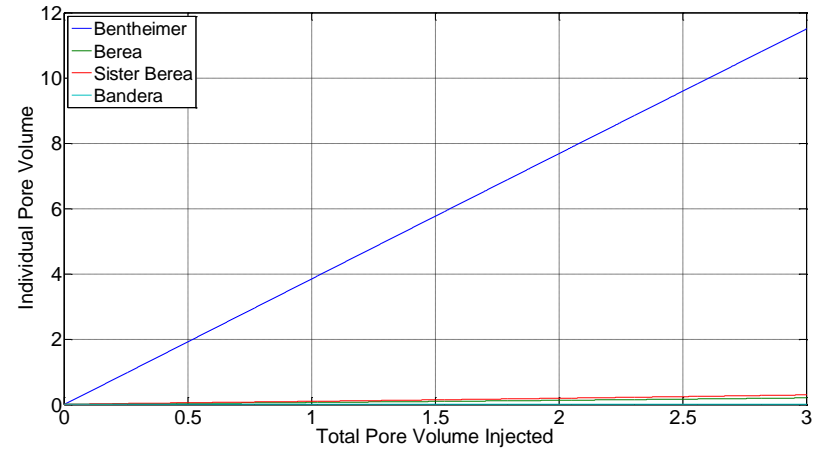


Figure 63: Individual Pore Volume vs. Total Pore Volume of Gas injected ($V_s=1.0^{-7}$) (Case III.B)

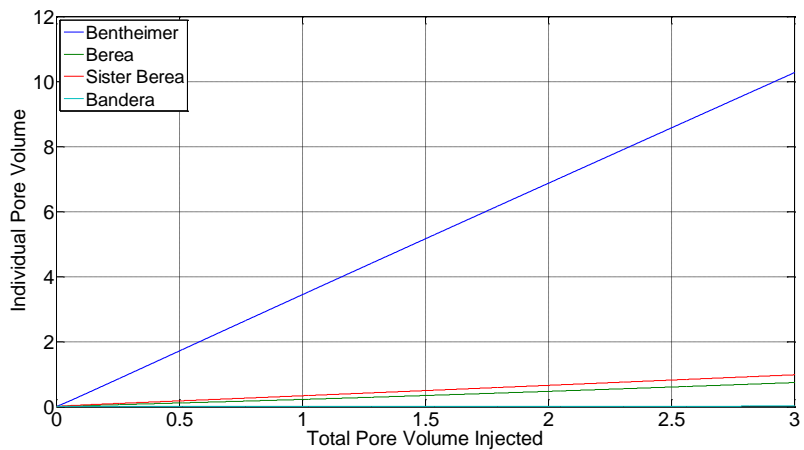


Figure 64: Individual Pore Volume vs. Total Pore Volume of Gas injected ($V_s=1.0^{-6}$) (Case III.B)

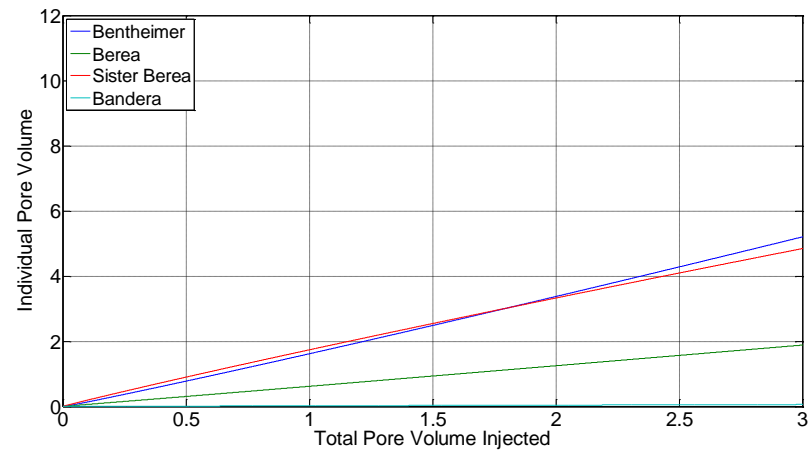


Figure 66: Individual Pore Volume vs. Total Pore Volume of Gas injected ($V_s=1.0^{-4}$) (Case III.B)

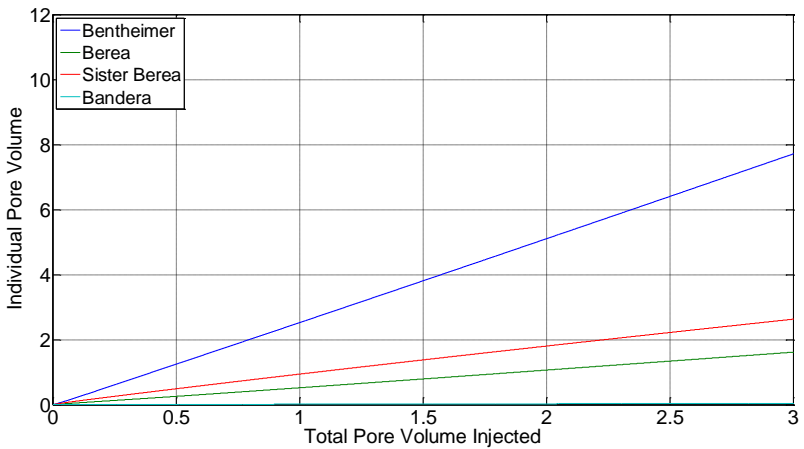


Figure 65: Individual Pore Volume vs. Total Pore Volume of Gas injected ($V_s=1.0^{-5}$) (Case III.B)

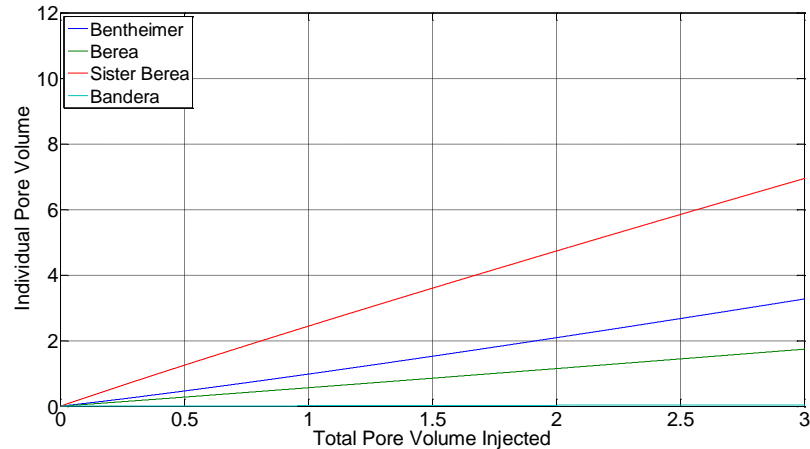


Figure 67: Individual Pore Volume vs. Total Pore Volume of Gas injected ($V_s=1.0^{-3}$) (Case III.B)

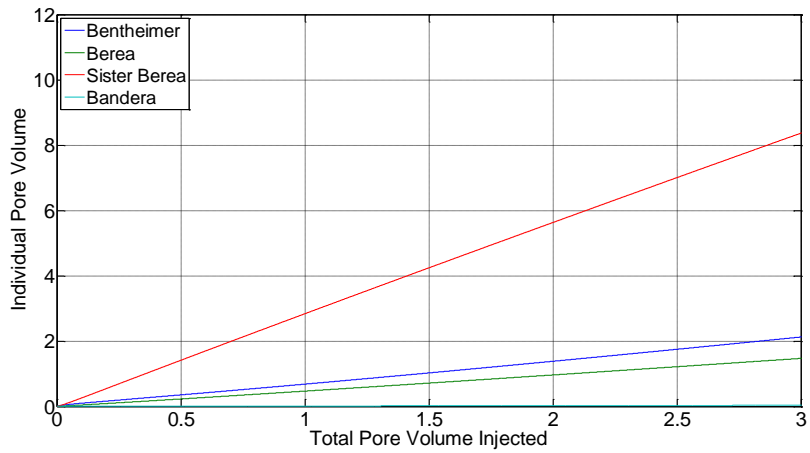


Figure 68: Individual Pore Volume vs. Total Pore Volume of Gas injected ($V_s=1.0^{-2}$) (Case III.B)

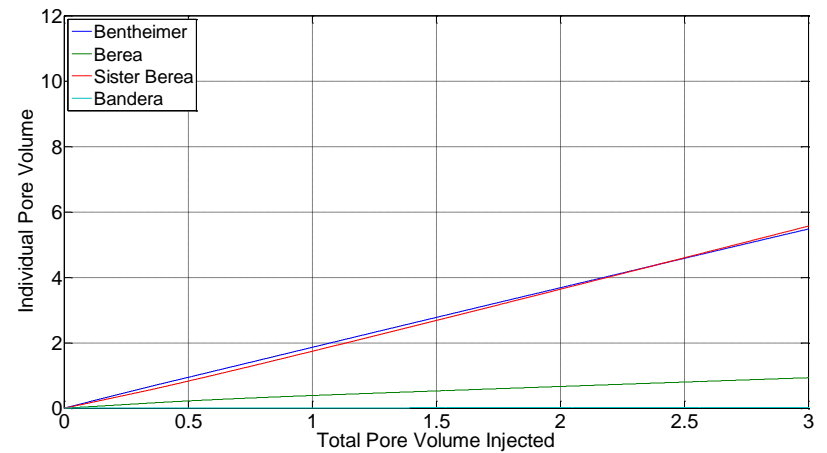


Figure 70: Individual Pore Volume vs. Total Pore Volume of Gas injected ($V_s=1.0$) (Case III.B)

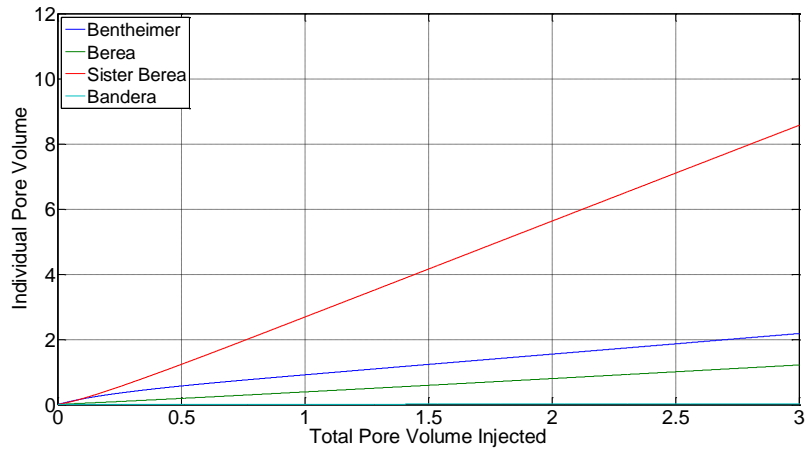


Figure 69: Individual Pore Volume vs. Total Pore Volume of Gas injected ($V_s=1.0^{-1}$) (Case III.B)

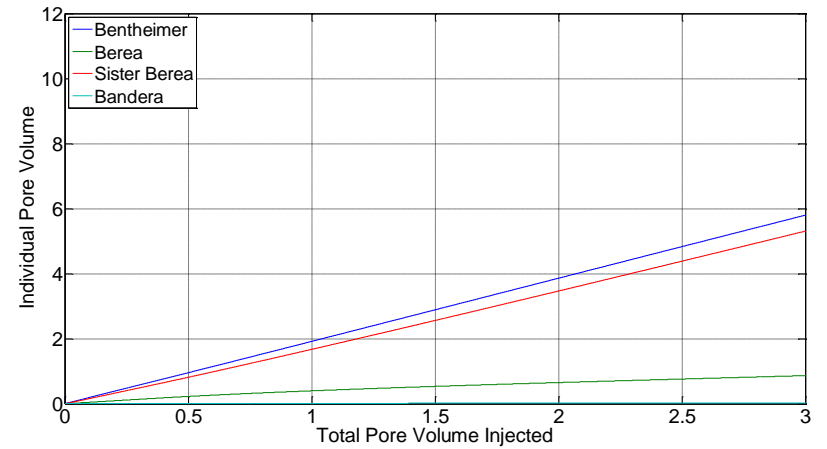


Figure 71: Individual Pore Volume vs. Total Pore Volume of Gas injected ($V_s=10.0$) (Case III.B)

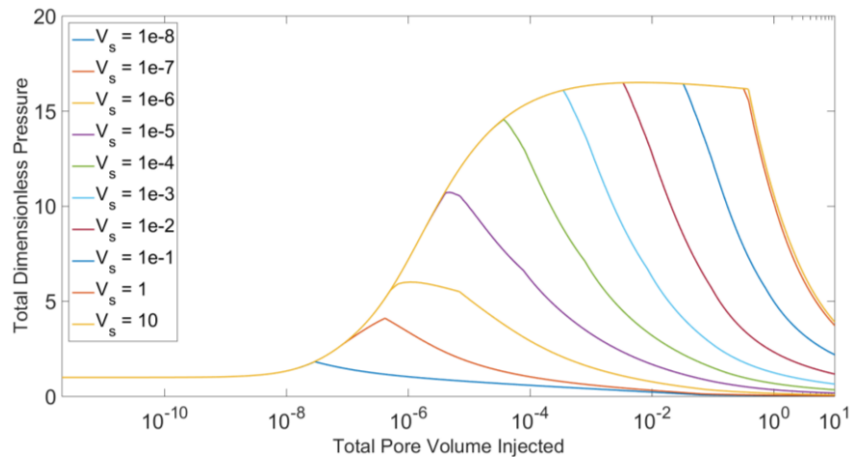


Figure 72: Total Dimensionless Pressure vs. Total Pore Volume Injected for Different Surfactant Slug Sizes Model (Case III.B)

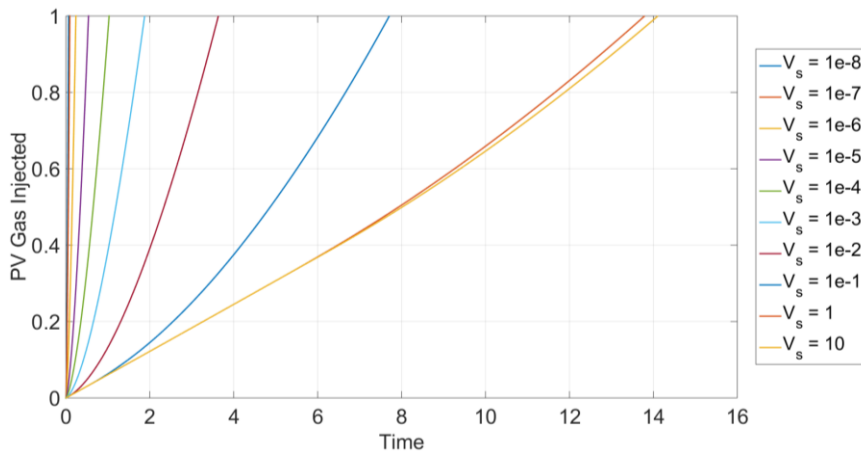


Figure 73: Relative Injection Time vs. PV of Gas Injected for Various Surfactant-Slug Sizes (Case III.B)

IV. No Surfactant Injection into Bandera Gray (A. Other Layers are Surfactant-Saturated i. STARS Model)

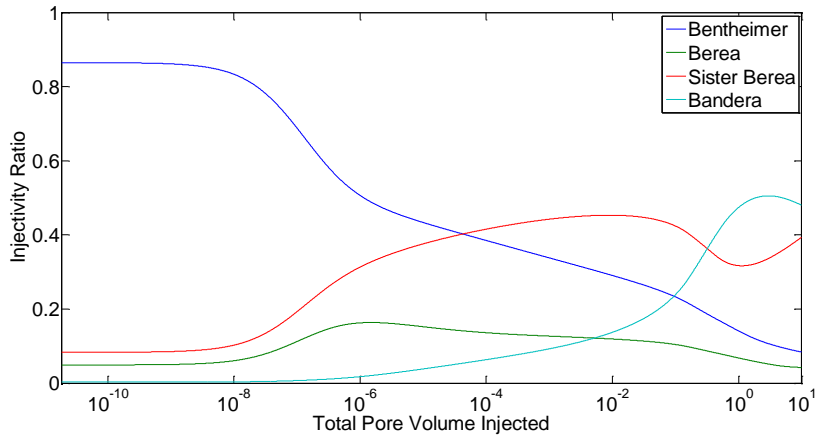


Figure 74: Injectivity Ratio vs. log of Total Pore Volumes (Case IV.A.i)

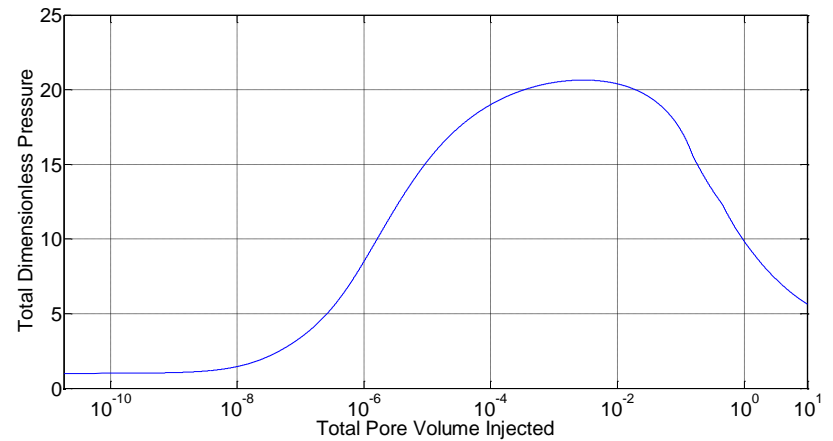


Figure 76: Total Dimensionless Pressure vs. Total Pore Volume injected (Case IV.A.i)

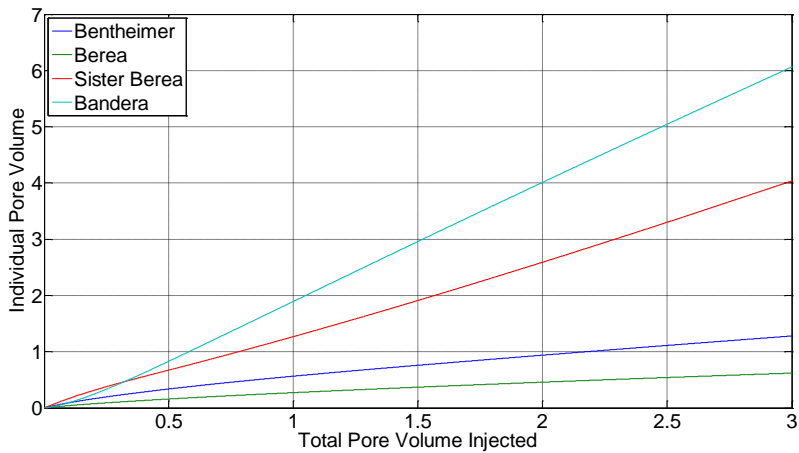


Figure 75: Individual Pore Volume vs. Total Pore Volume of Gas injected (Case IV.A.i)

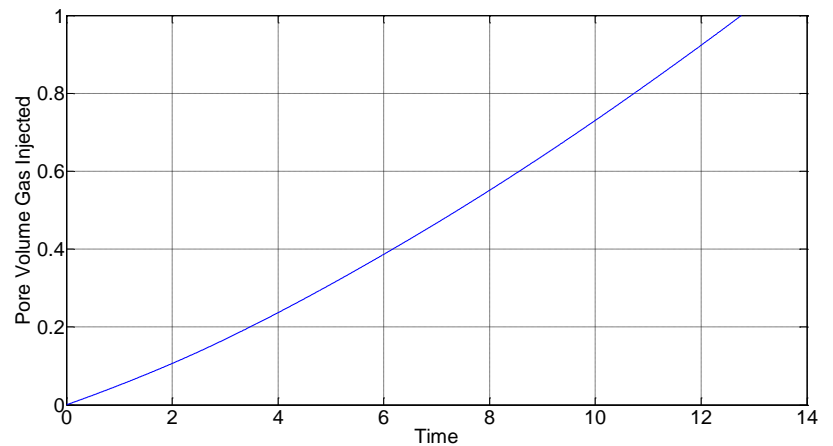


Figure 77: Relative Injection Time vs. PV of Gas Injected (Case IV.A.i)

IV. No Surfactant Injection into Bandera Gray (A. Other Layers are Surfactant-Saturated ii. Namdar Zanganeh et al. Modified Model)

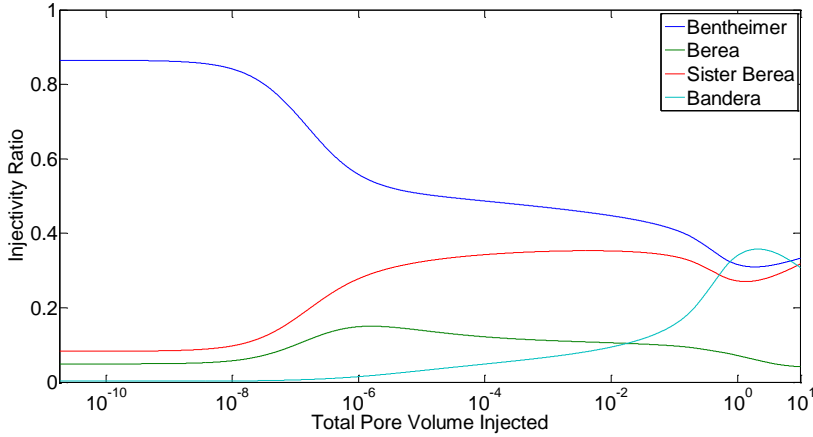


Figure 78: Injectivity Ratio vs. log of Total Pore Volumes (Case IV.A.ii)

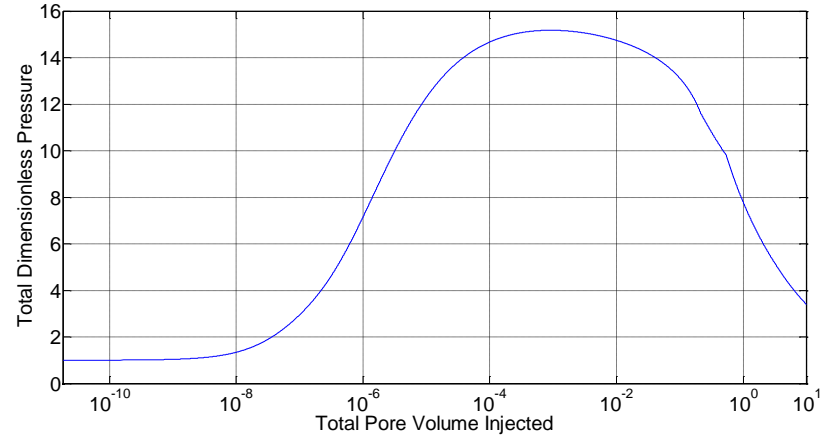


Figure 80: Total Dimensionless Pressure vs. Total Pore Volume injected (Case IV.A.i)

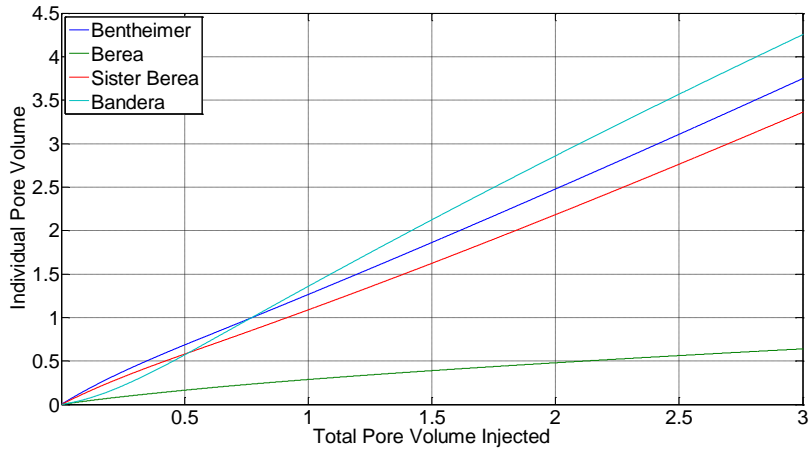


Figure 79: Individual Pore Volume vs. Total Pore Volume of Gas injected (Case IV.A.ii)

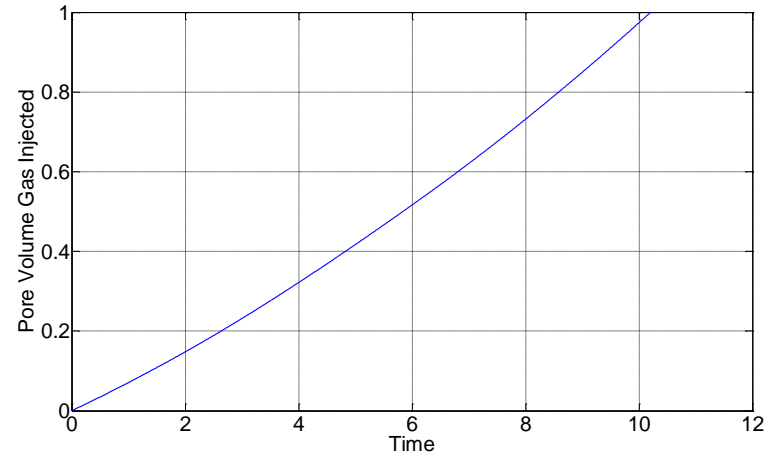


Figure 81: Relative Injection Time vs. PV of Gas Injected (Case IV.A.i)

IV. No Surfactant Injection into Bandera Gray (B. Discrete Surfactant Slugs ii. STARS Model)

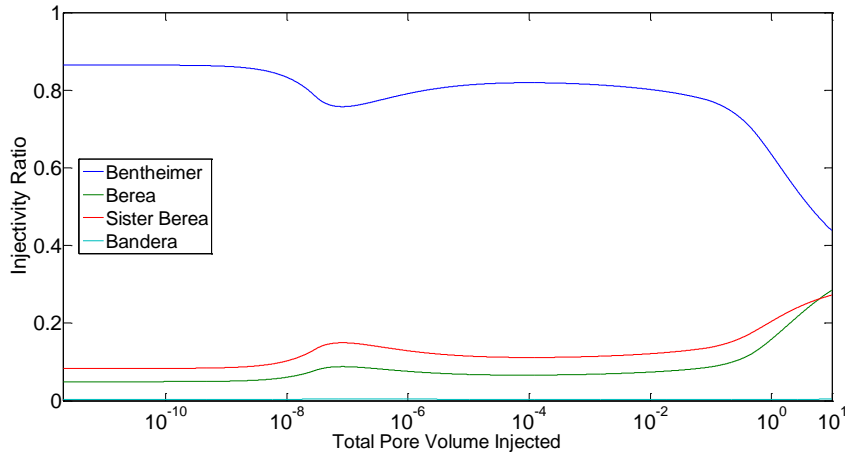


Figure 82: Injectivity Ratio vs. Total Pore Volume of Gas injected ($V_s=1.0^{-8}$) (Case IV.B.i)

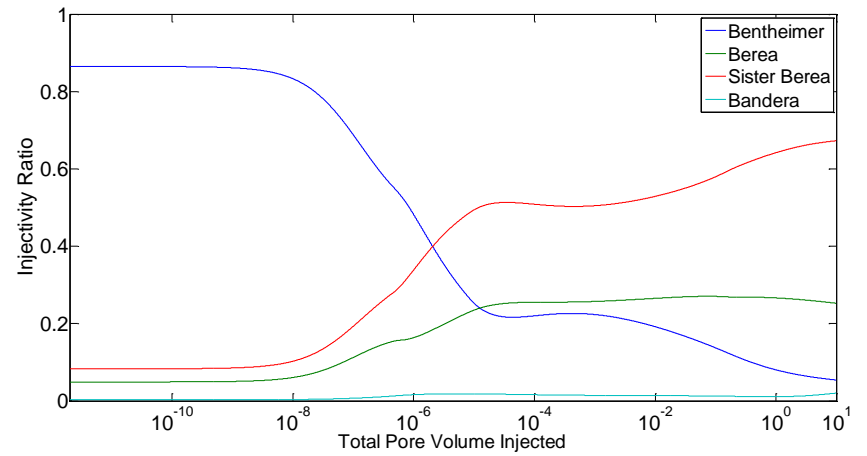


Figure 84: Injectivity Ratio vs. Total Pore Volume of Gas injected ($V_s=1.0^{-6}$) (Case IV.B.i)

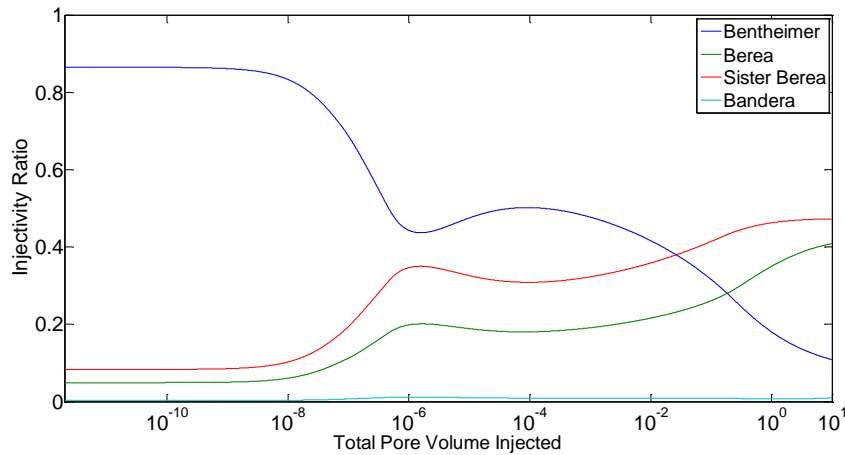


Figure 83: Injectivity Ratio vs. Total Pore Volume of Gas injected ($V_s=1.0^{-7}$) (Case IV.B.i)

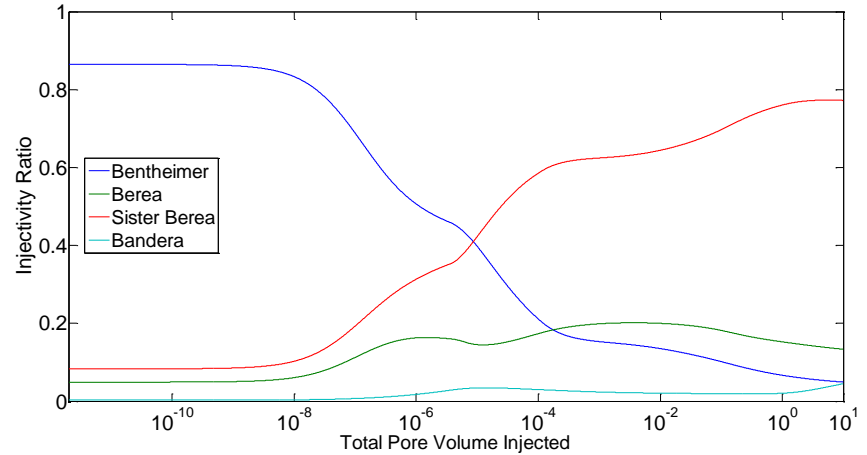


Figure 85: Injectivity Ratio vs. Total Pore Volume of Gas injected ($V_s=1.0^{-5}$) (Case IV.B.i)

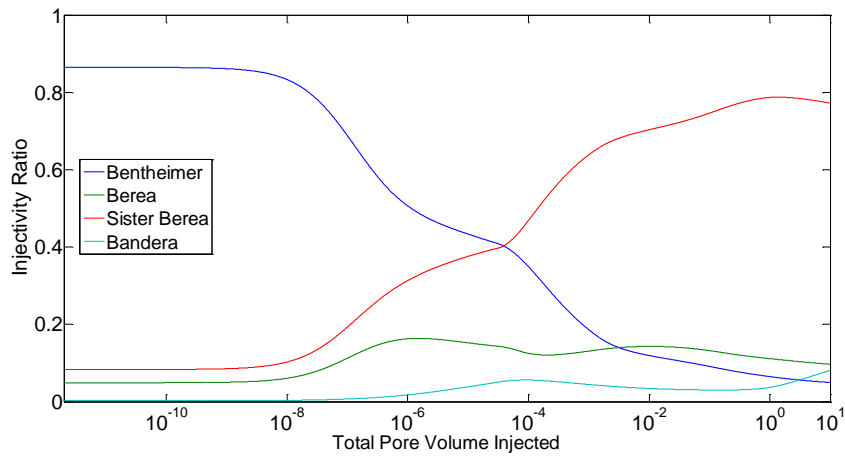


Figure 86: Injectivity Ratio vs. Total Pore Volume of Gas injected ($V_s=1.0^{-4}$) (Case IV.B.i)

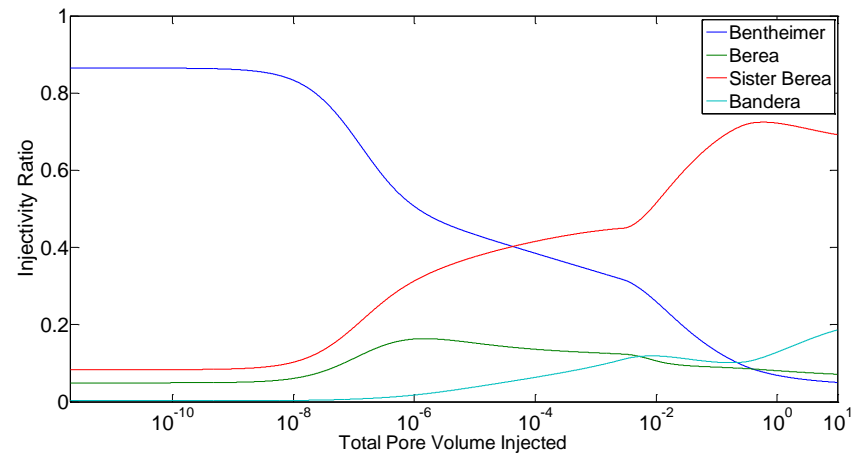


Figure 88: Injectivity Ratio vs. Total Pore Volume of Gas injected ($V_s=1.0^{-2}$) (Case IV.B.i)

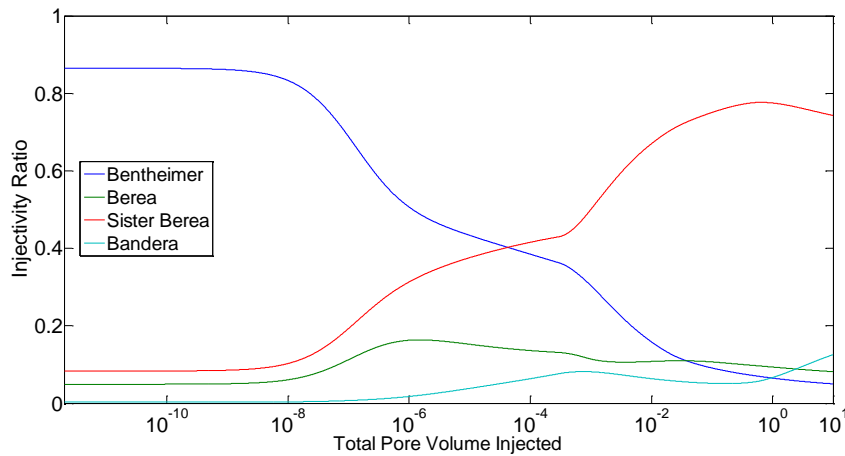


Figure 87: Injectivity Ratio vs. Total Pore Volume of Gas injected ($V_s=1.0^{-3}$) (Case IV.B.i)

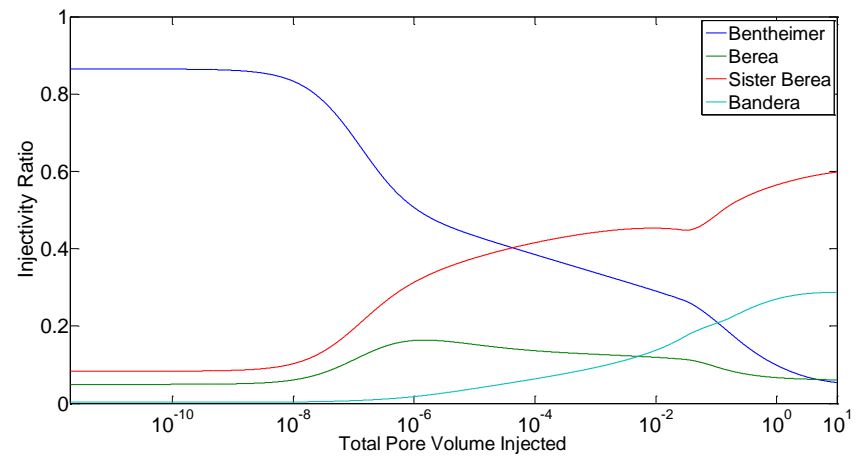


Figure 89: Injectivity Ratio vs. Total Pore Volume of Gas injected ($V_s=1.0^{-1}$) (Case IV.B.i)

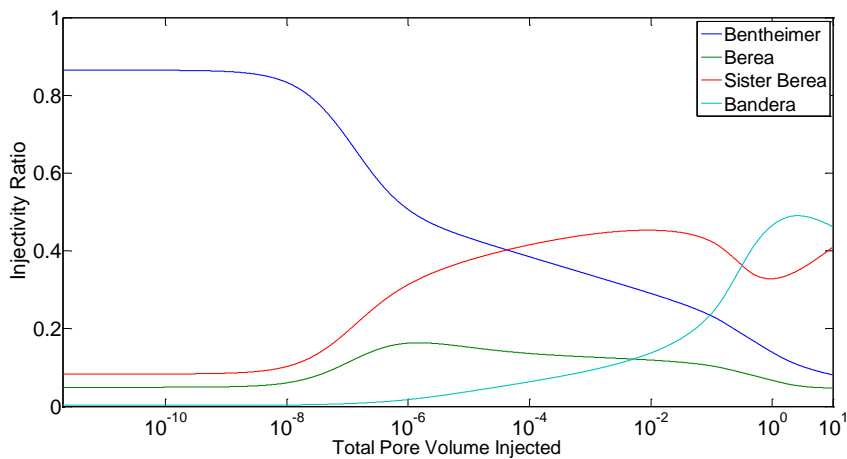


Figure 90: Injectivity Ratio vs. Total Pore Volume of Gas injected ($V_s=1.0$) (Case IV.B.i)

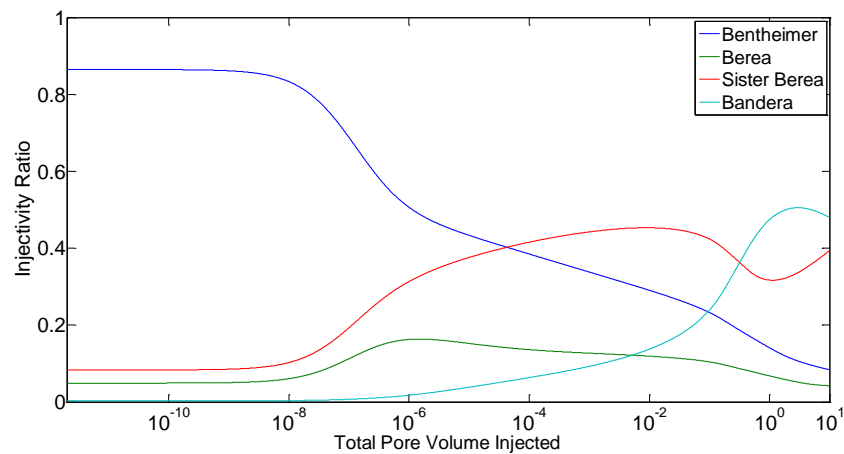


Figure 91: Injectivity Ratio vs. Total Pore Volume of Gas injected ($V_s=10.0$) (Case IV.B.i)

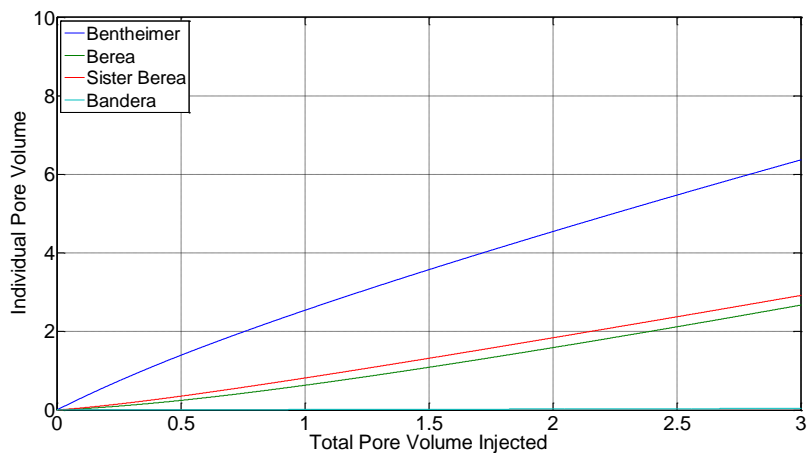


Figure 92: Individual Pore Volume vs. Total Pore Volume of Gas injected ($V_s=1.0^{-8}$) (Case IV.B.i)

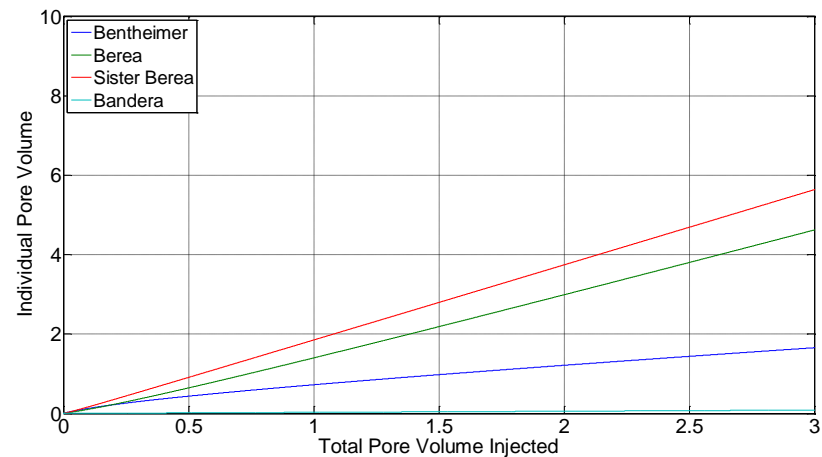


Figure 93: Individual Pore Volume vs. Total Pore Volume of Gas injected ($V_s=1.0^{-7}$) (Case IV.B.i)

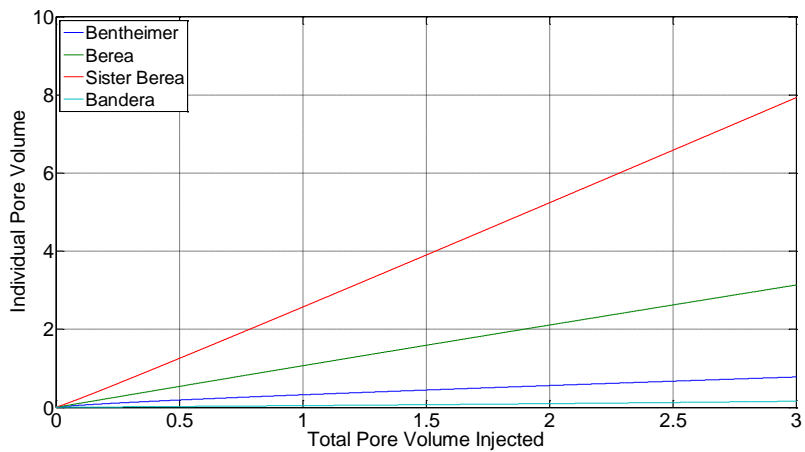


Figure 94: Individual Pore Volume vs. Total Pore Volume of Gas injected ($V_s=1.0^{-6}$) (Case IV.B.i)

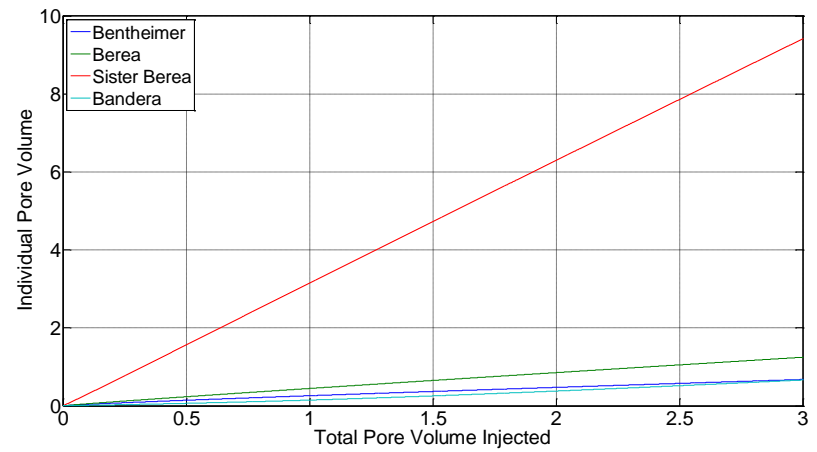


Figure 96: Individual Pore Volume vs. Total Pore Volume of Gas injected ($V_s=1.0^{-4}$) (Case IV.B.i)

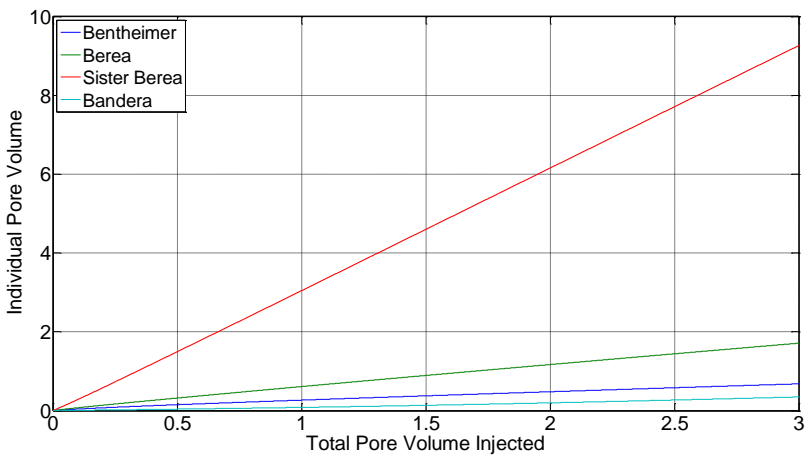


Figure 95: Individual Pore Volume vs. Total Pore Volume of Gas injected ($V_s=1.0^{-5}$) (Case IV.B.i)

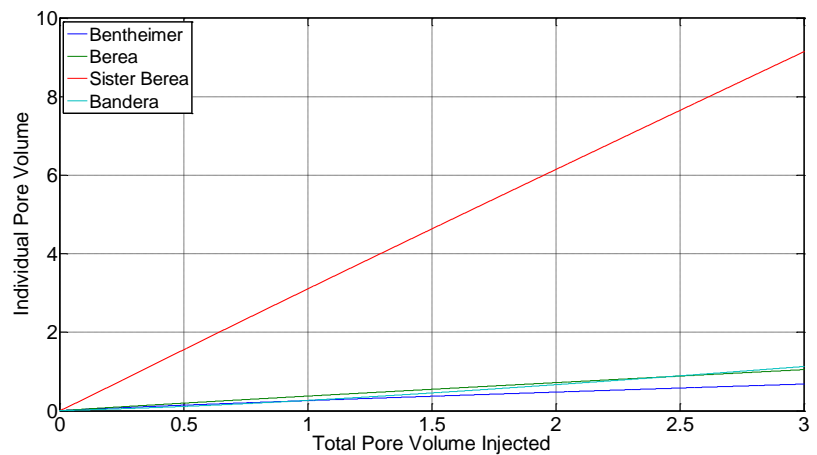


Figure 97: Individual Pore Volume vs. Total Pore Volume of Gas injected ($V_s=1.0^{-3}$) (Case IV.B.i)

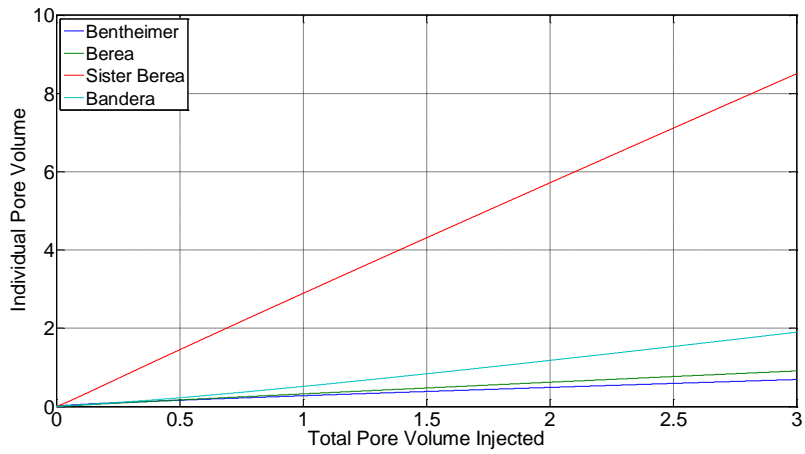


Figure 98: Individual Pore Volume vs. Total Pore Volume of Gas injected ($V_s=1.0^{-2}$) (Case IV.B.i)

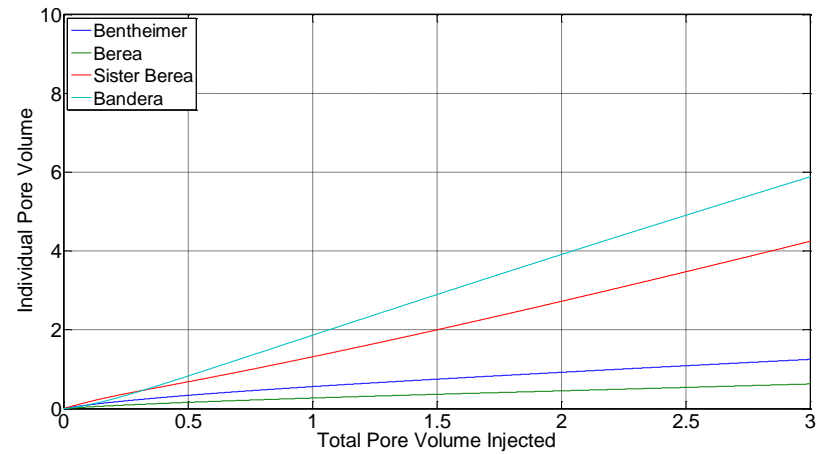


Figure 100: Individual Pore Volume vs. Total Pore Volume of Gas injected ($V_s=1.0$) (Case IV.B.i)

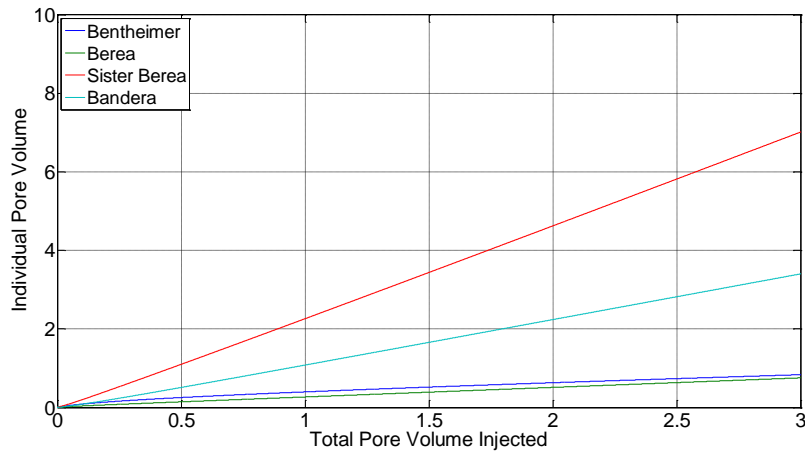


Figure 99: Individual Pore Volume vs. Total Pore Volume of Gas injected ($V_s=1.0^{-1}$) (Case IV.B.i)

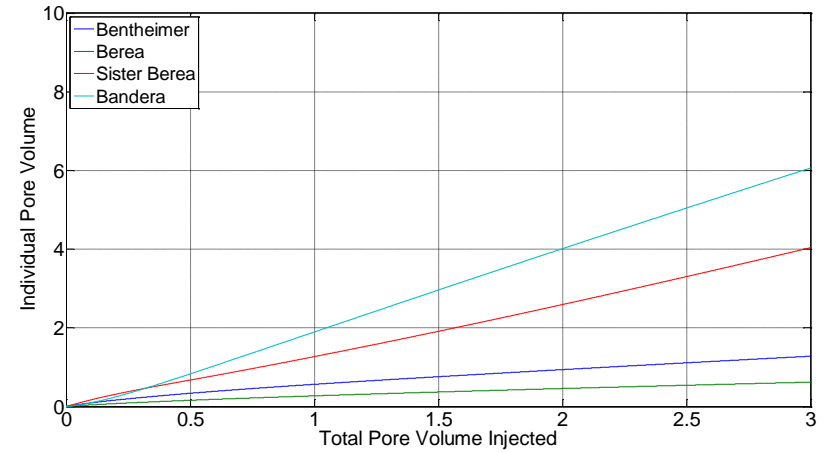


Figure 101: Individual Pore Volume vs. Total Pore Volume of Gas injected ($V_s=10.0$) (Case IV.B.i)

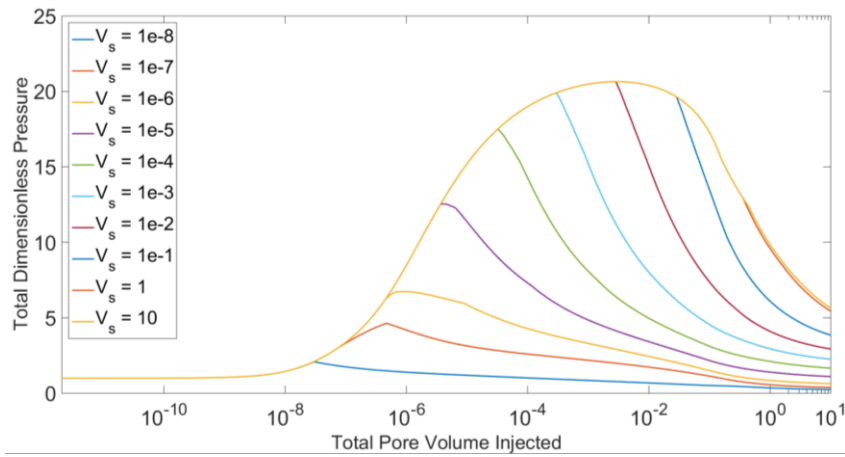


Figure 102: Total Dimensionless Pressure vs. Total Pore Volume Injected for Different Surfactant Slug Sizes Model (Case IV.B.i)

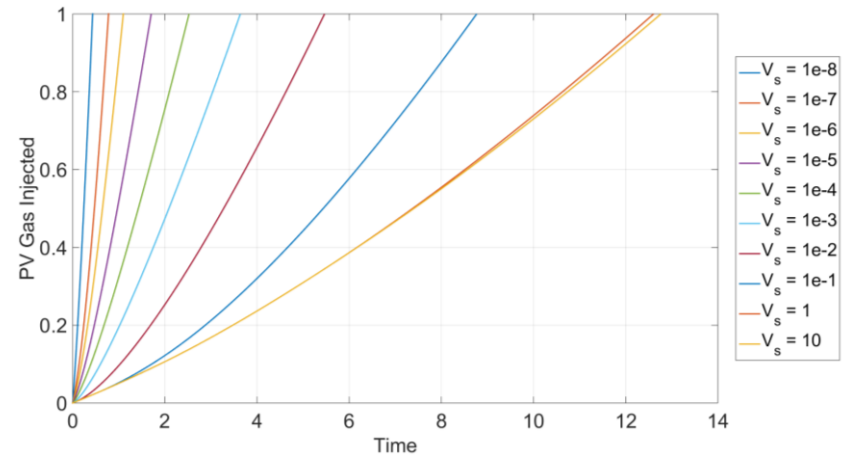


Figure 103: Relative Injection Time vs. PV of Gas Injected for Various Surfactant-Slug Sizes (Case IV.B.i)

IV. No Surfactant Injection into Bandera Gray (B. Discrete Surfactant Slugs ii. Namdar Zanganeh et al. Modified Model)

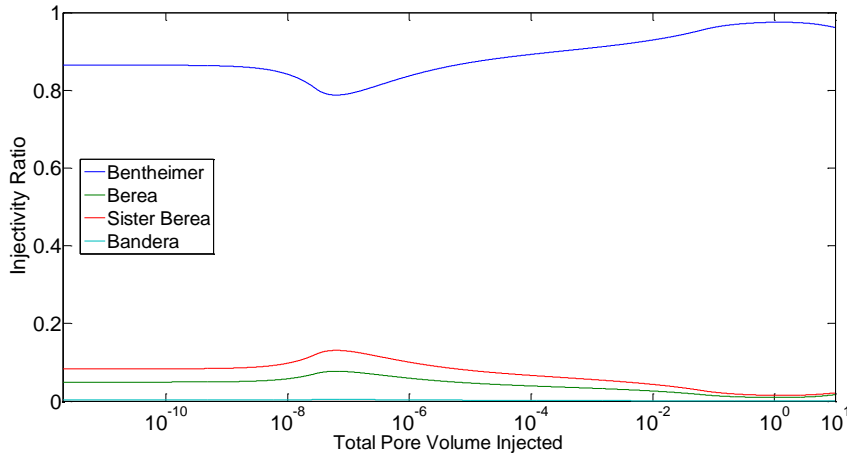


Figure 104: Injectivity Ratio vs. Total Pore Volume of Gas injected ($V_s=1.0^{-8}$) (Case IV.B.ii)

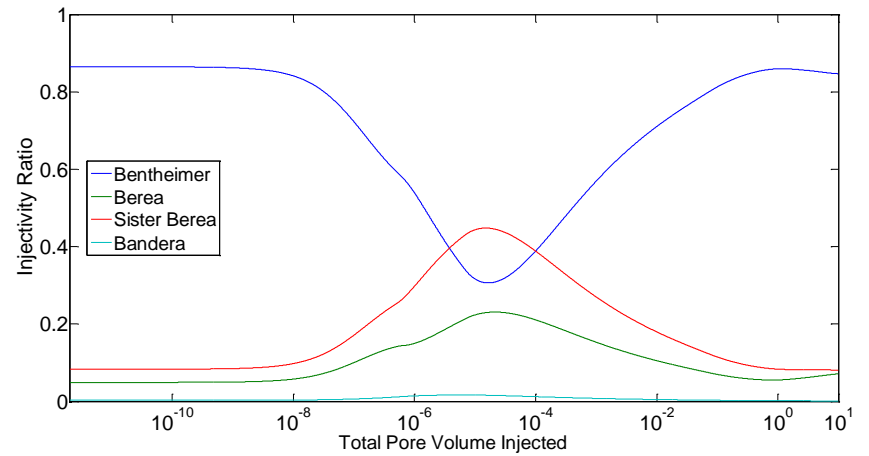


Figure 106: Injectivity Ratio vs. Total Pore Volume of Gas injected ($V_s=1.0^{-6}$) (Case IV.B.ii)

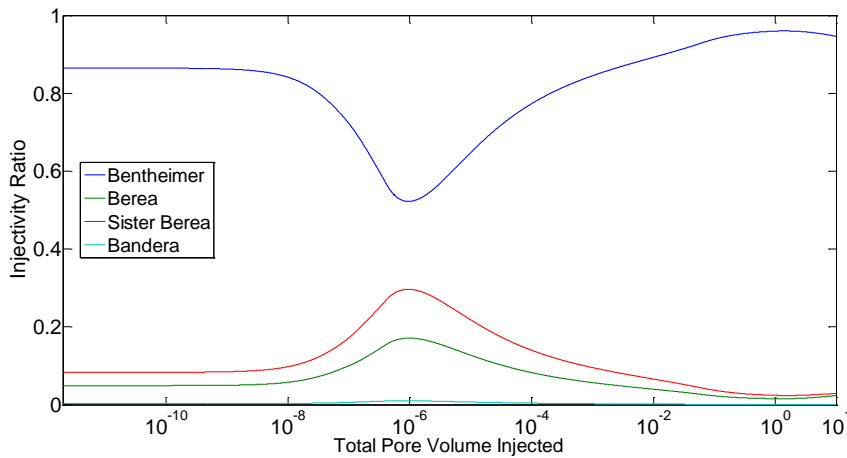


Figure 105: Injectivity Ratio vs. Total Pore Volume of Gas injected ($V_s=1.0^{-7}$) (Case IV.B.ii)

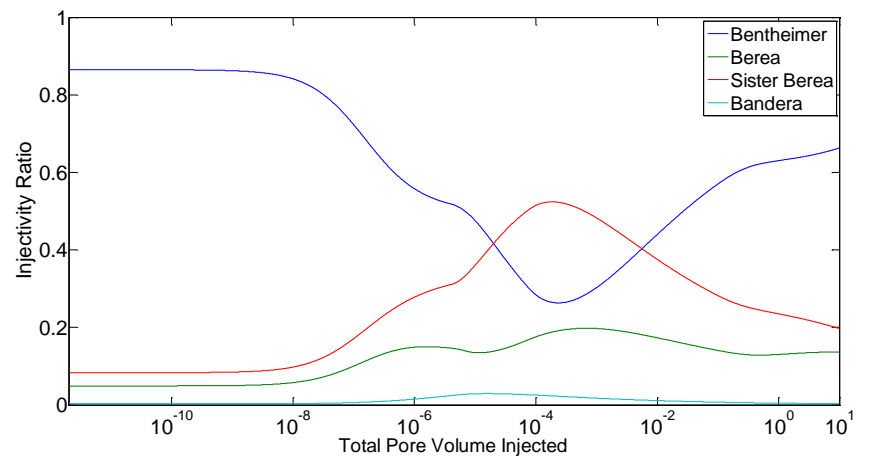


Figure 107: Injectivity Ratio vs. Total Pore Volume of Gas injected ($V_s=1.0^{-5}$) (Case IV.B.ii)

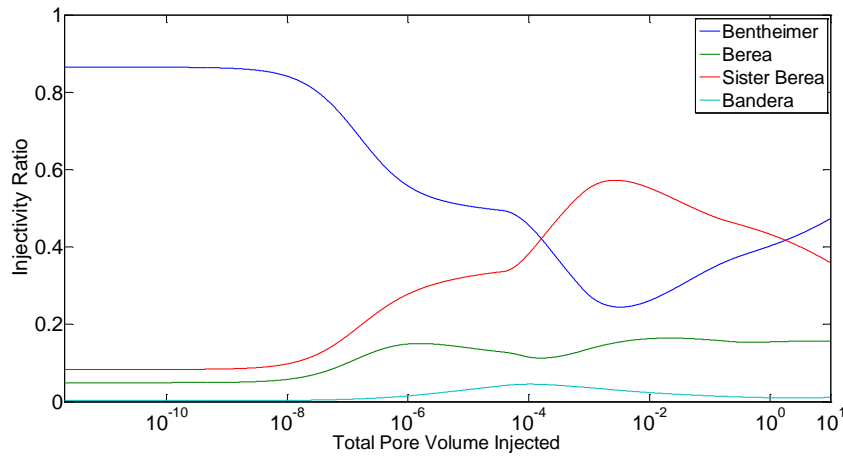


Figure 108: Injectivity Ratio vs. Total Pore Volume of Gas injected ($V_s=1.0^{-4}$) (Case IV.B.ii)

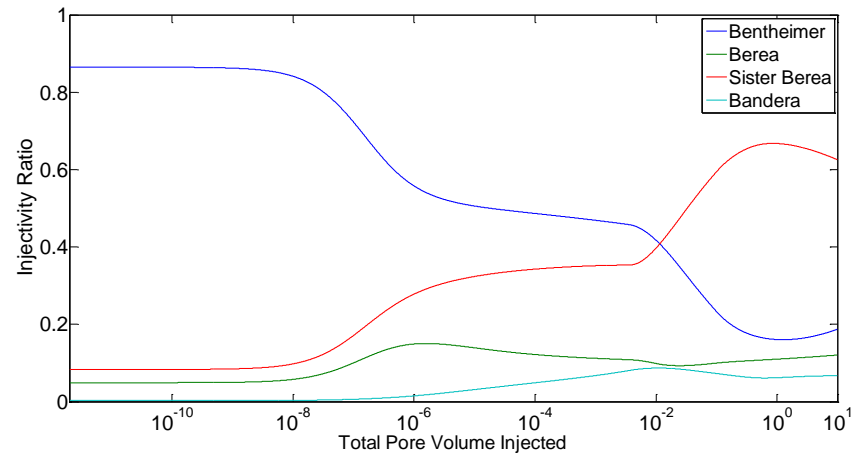


Figure 110: Injectivity Ratio vs. Total Pore Volume of Gas injected ($V_s=1.0^{-2}$) (Case IV.B.ii)

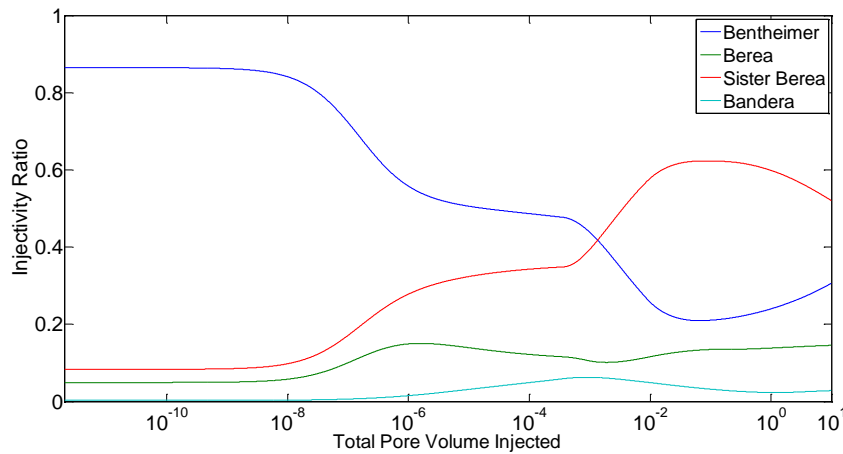


Figure 109: Injectivity Ratio vs. Total Pore Volume of Gas injected ($V_s=1.0^{-3}$) (Case IV.B.ii)

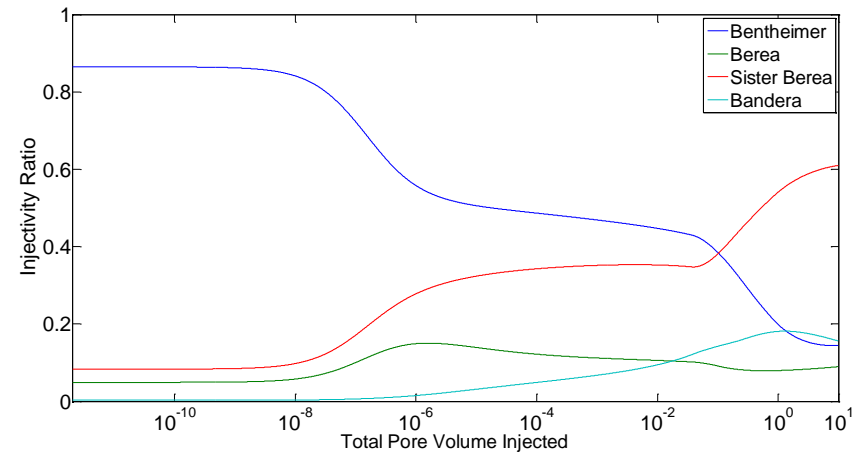


Figure 111: Injectivity Ratio vs. Total Pore Volume of Gas injected ($V_s=1.0^{-1}$) (Case IV.B.ii)

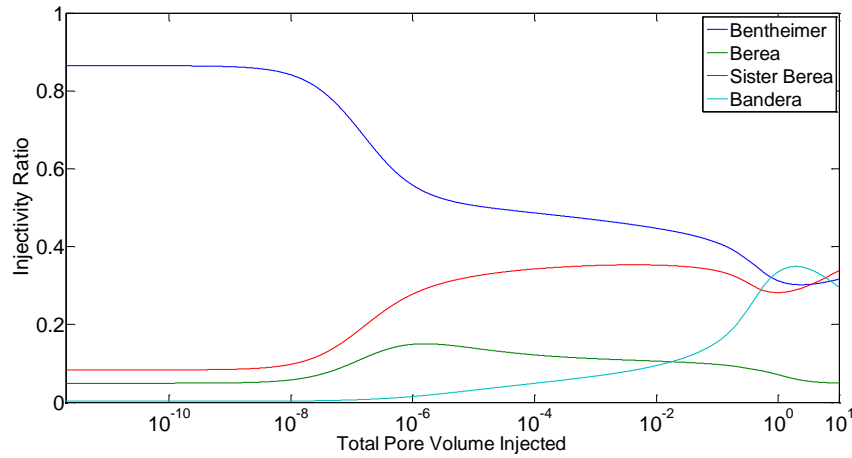


Figure 112: Injectivity Ratio vs. Total Pore Volume of Gas injected ($V_s=1.0$) (Case IV.B.ii)

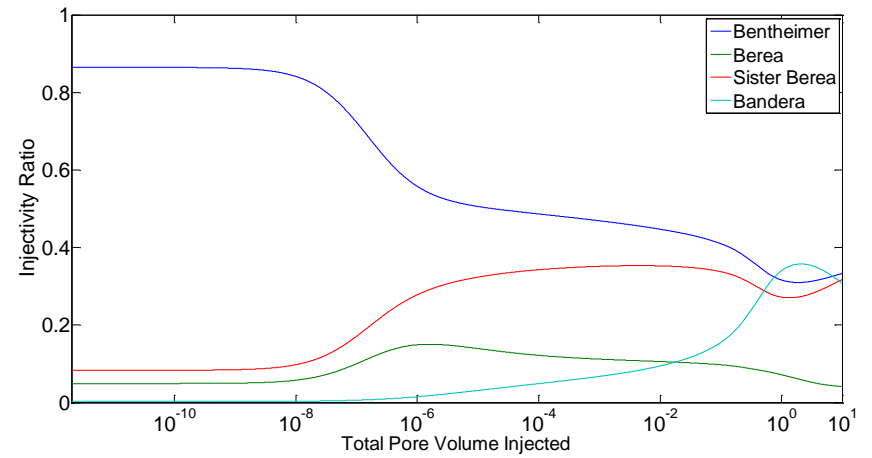


Figure 113: Injectivity Ratio vs. Total Pore Volume of Gas injected ($V_s=10.0$) (Case IV.B.ii)

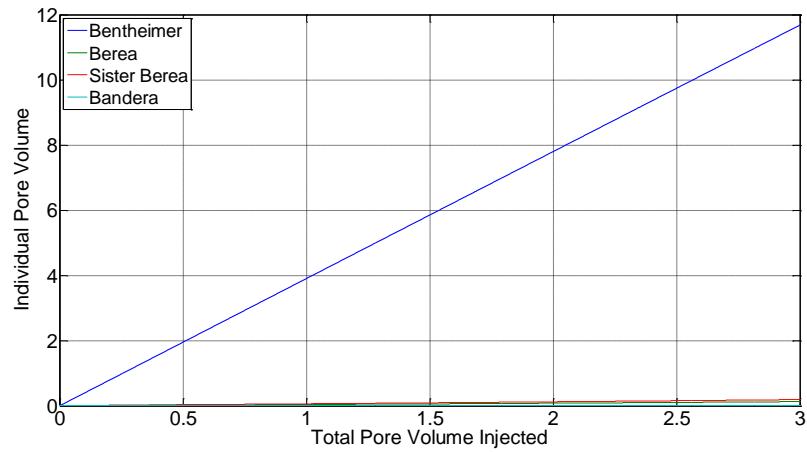


Figure 114: Individual Pore Volume vs. Total Pore Volume of Gas injected ($V_s=1.0^{-8}$) (Case IV.B.ii)

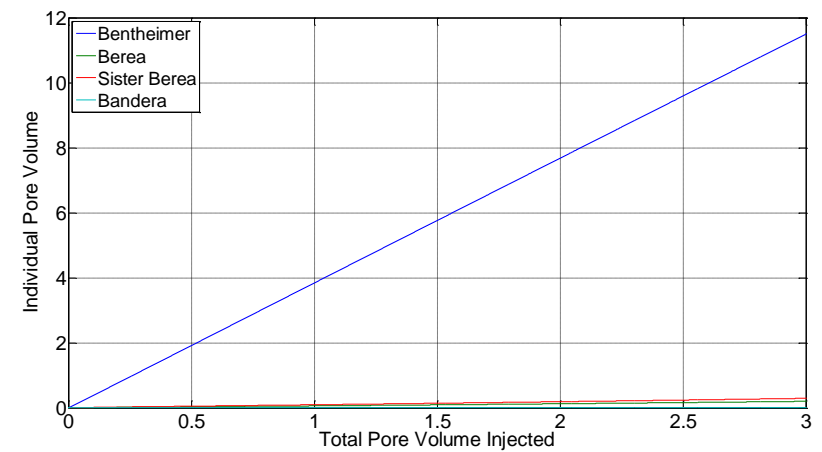


Figure 115: Individual Pore Volume vs. Total Pore Volume of Gas injected ($V_s=1.0^{-7}$) (Case IV.B.ii)

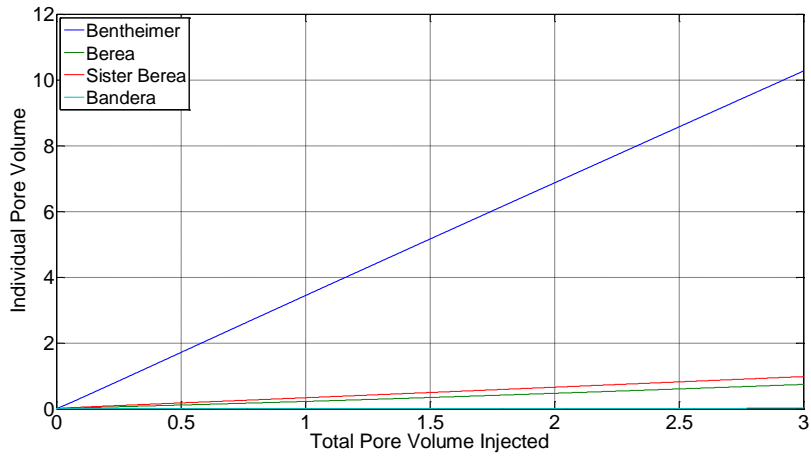


Figure 116: Individual Pore Volume vs. Total Pore Volume of Gas injected ($V_s=1.0^{-6}$) (Case IV.B.ii)

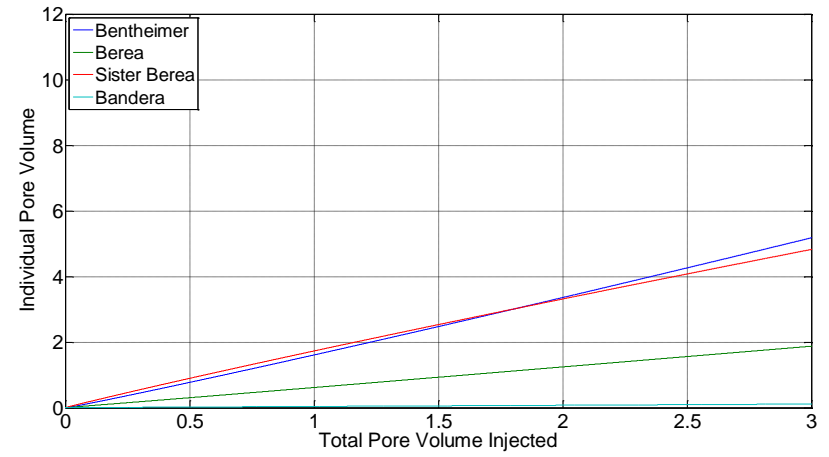


Figure 118: Individual Pore Volume vs. Total Pore Volume of Gas injected ($V_s=1.0^{-4}$) (Case IV.B.ii)

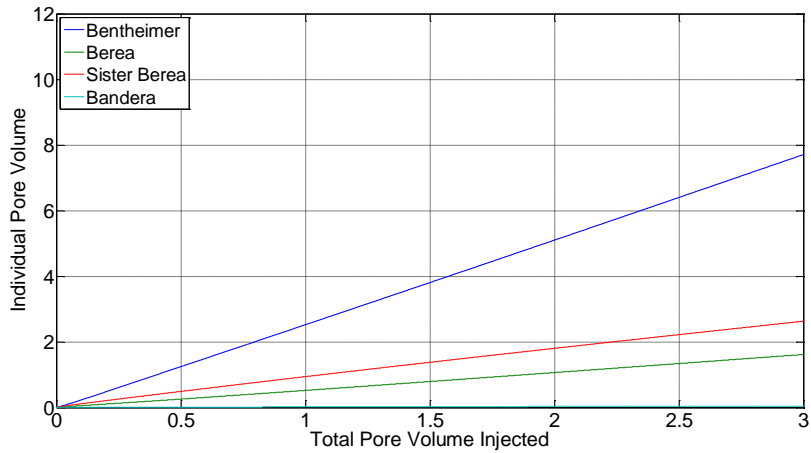


Figure 117: Individual Pore Volume vs. Total Pore Volume of Gas injected ($V_s=1.0^{-5}$) (Case IV.B.ii)

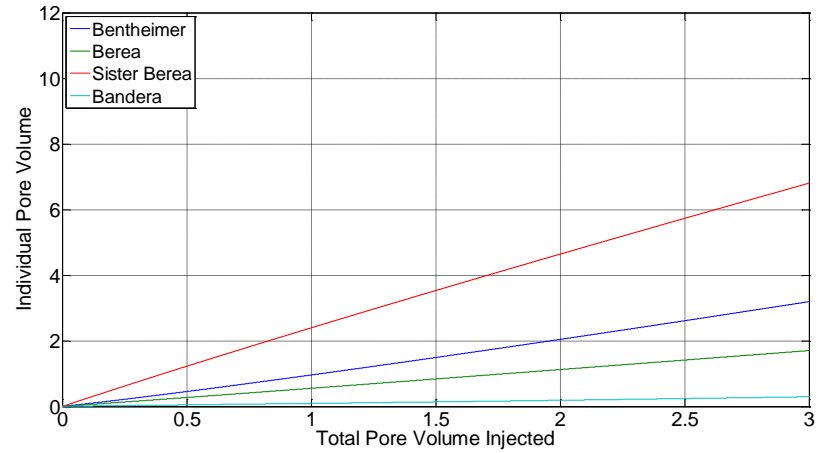


Figure 119: Individual Pore Volume vs. Total Pore Volume of Gas injected ($V_s=1.0^{-3}$) (Case IV.B.ii)

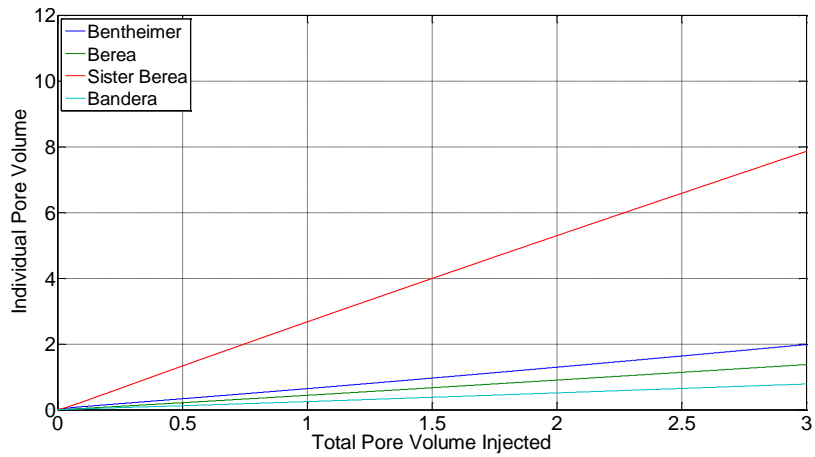


Figure 120: Individual Pore Volume vs. Total Pore Volume of Gas injected ($V_s=1.0^{-2}$) (Case IV.B.ii)

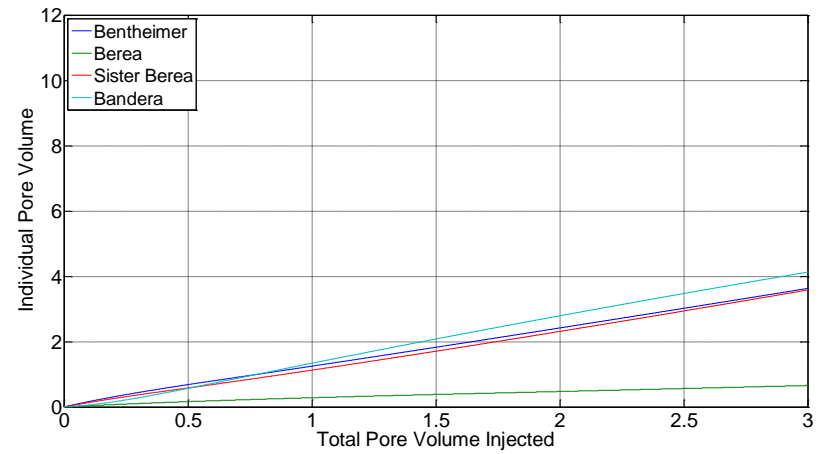


Figure 122: Individual Pore Volume vs. Total Pore Volume of Gas injected ($V_s=1.0$) (Case IV.B.ii)

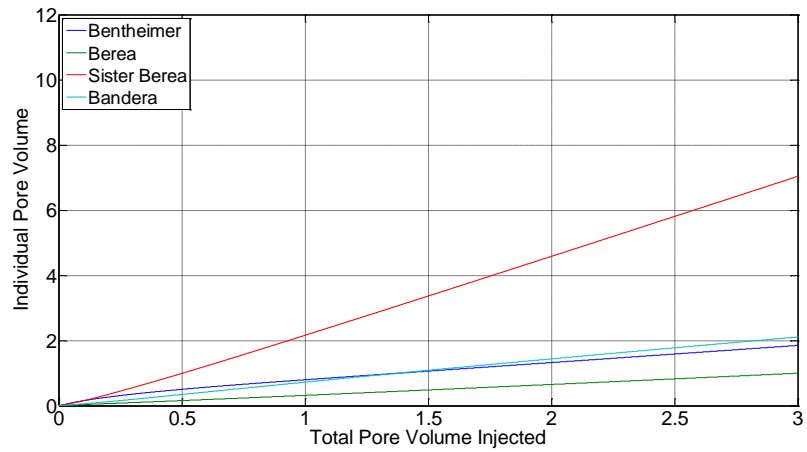


Figure 121: Individual Pore Volume vs. Total Pore Volume of Gas injected ($V_s=1.0^{-1}$) (Case IV.B.ii)

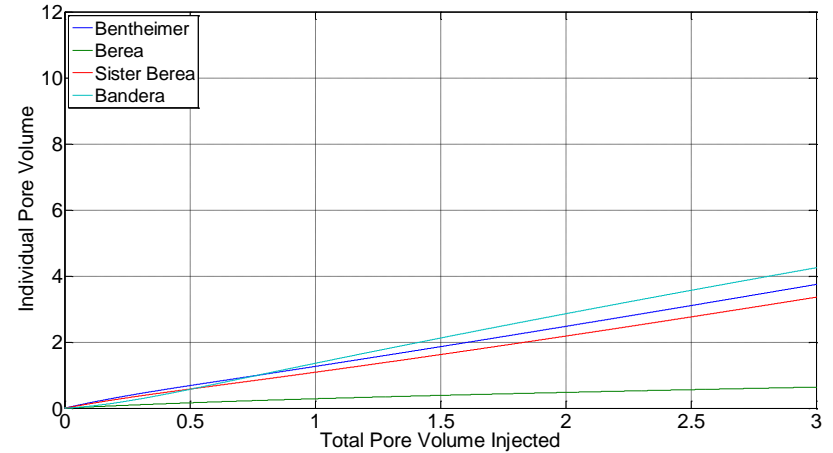


Figure 123: Individual Pore Volume vs. Total Pore Volume of Gas injected ($V_s=10.0$) (Case IV.B.ii)

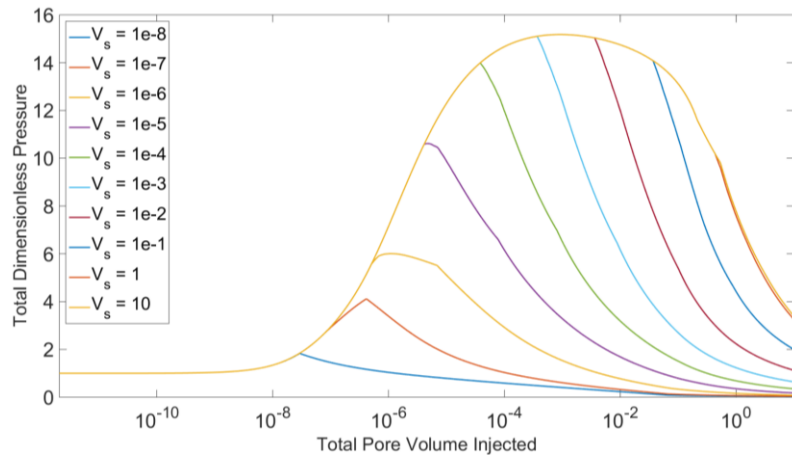


Figure 124: Total Dimensionless Pressure vs. Total Pore Volume Injected for Different Surfactant Slug Sizes Model (Case IV.B.ii)

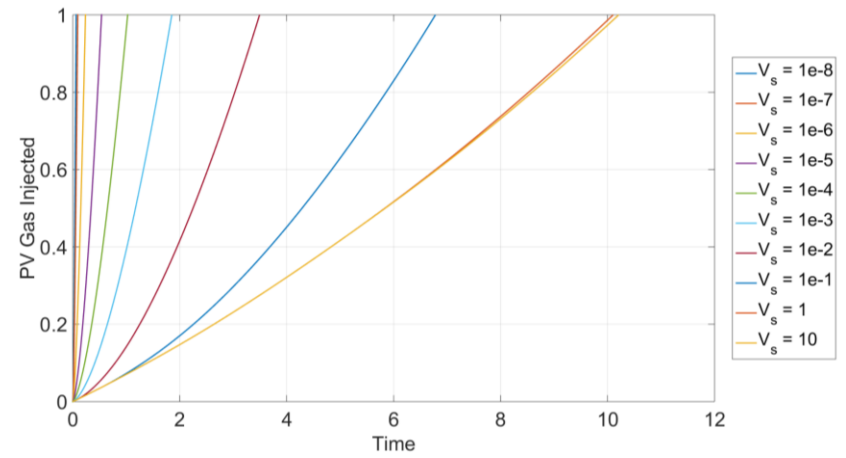


Figure 125: Relative Injection Time vs. PV of Gas Injected for Various Surfactant-Slug Sizes (Case IV.B.ii)

4 Discussion

The base case (case I) studies gas injection without surfactant. In the envisaged reservoir setting, the highest permeability layer (Bentheimer) receives about 86% of the injected gas and presents the highest level of recycling as shown in **Figure 18**. Gas is injected in fractions of the total reservoir volume $t_{D_{total}}$, and it is tracked into each individual layer as a ratio of the individual layer's pore volume t_{D_j} . We can compare between the volumes received by each layer since all layers have equivalent pore volume. **Figure 19** shows that if 3 total pore volumes (equivalent to 12 individual layer pore volumes) are injected, the majority of flow goes to the Bentheimer (about 11 PV_j) while the Berea and Sister Berea receive less than an individual pore volume. The Bandera layer barely receives any noticeable flow. The dynamic change in the injectivity ratio is due to changes in mobility as gas saturation increases and due to gas breakthrough. **Figure 20** shows that the total dimensionless pressure $P_{D_{total}}$ as a function of total pore volume injected $t_{D_{total}}$ is much less than 1 demonstrating that gas is easier to inject than water. Furthermore, the relative injection time for a single total pore volume $t_{D_{total}}$ of gas in this case is about 6% of the time it would take to inject the same volume of water in single-phase flow as shown in **Figure 21**.

In case (II.A), for the STARS model where all layers are filled with surfactant, the graphs show different behaviour than that for gas injection without surfactant. Due to foam forming in-situ, the change in total relative mobility in each layer is based on foam model parameters ($fmdry$, $epdry$ and $fmmob$) and the amount of gas it receives t_{D_j} . Therefore, injectivity ratio changes as a function of $t_{D_{total}}$. For the highest-permeability layer (Benteheimer), the ratio drops from 86% to 30% after the injection of 1 PV_{total} and continues to drop over 10 PV_{total} of injection as shown in **Figure 22**. **Figure 23** shows how much each layer would receive if 3 PV_{total} (12 PV_j) are injected: Bentheimer, Berea, and sister Berea would approximately receive 2.8, 7.5, and 1.5 individual pore volumes. This indicates that the Sister Berea layer receives more flow than the Benteheimer layer, in spite of the large difference in the kh -ratio. As shown in **Table 7**, the model predicts that the total relative mobility at the shock front is around 4, 20, 43, 9 [Pa.s]⁻¹ for Bentheimer, Berea, Sister Berea, and Bandera respectively. Additionally, the total relative mobility at S_{wr} is around 16, 369, 2755, 23 [Pa.s]⁻¹ for Bentheimer, Berea, Sister Berea, and Bandera respectively. Total relative mobility for Bentheimer, Berea, Sister Berea, and Bandera increases about 4, 18, 60, and 3 times between $S_{w,shock}$ and S_{wr} . The extent to which gas mobility in the foam bank increases depends on a combination of $epdry$ and $fmmob$ parameters. For the Sister Berea layer, the manner at which the total relative mobility increases from the shock front to residual water saturation at the wellbore allows it to receive more flow than the other layers as displayed in **Figure 23**. **Figure 24** shows that the total dimensionless pressure $P_{D_{total}}$ as function of total pore volume injected rises to about 26, indicating low injectivity. **Figure 25** shows that the relative time to inject 1 PV_{total} of gas in this scenario is about 25 times longer than it would take to inject the same volume of water in single-phase flow.

In case (II.B), for the Namdar Zanganeh et al. modification, where all layers are filled with surfactants, the results are different than those predicted by the STARS model. In **Figure 26**, injectivity decreases less than that predicted by the STARS model (86% vs. 50%) after 1 PV_{total} of gas injection. This is due to the fact that the model allows for foam breakage at S_{wr} . In this case, the predicted total relative mobilities at the shock front are slightly higher than those predicted by the STARS model as shown in **Table 5** and **Table 6**. However, the modified model of Namdar Zanganeh et al. predicts that the total relative mobility at S_{wr} is equivalent to the total gas relative mobility at S_{wr} without surfactant as shown in **Table 4** and **Table 6**.

Figure 26 shows that the individual pore volume intake t_{D_j} for the Bentheimer and Sister Berea layers is almost equivalent. **Figure 28** shows that the rise in $P_{D_{total}}$ as a function of $t_{D_{total}}$ is significantly lower than that predicted by STARS model; $P_{D_{total}}$ rises up to around 17 (almost 30% lower than case II.A). **Figure 29** shows that the relative time to inject 1 PV_{total} of gas in this scenario is about 14 times (almost 45% lower than case II.A) longer than it would take to inject a single total pore volume of water in single-phase flow. For cases (III.A and III. B), the diversion performance of different surfactant slug sizes, injected prior to gas, is evaluated in order to determine the optimum surfactant slug size. For both models, the injectivity ratio changes significantly as the surfactant slug size changes as shown in **Figure 30** through **Figure 39** and **Figure 52** through **Figure 61**. However, for the modified model of Namdar Zanganeh et al., the injectivity in all layers tends to rise after the highest mobility reduction is reached as displayed in **Figure 52** through **Figure 61**. As highlighted earlier, this is the main difference between cases A and B; the effect of foam coalescences is observed when using the Namdar Zanganeh et al. modification. A better diversion is achieved as the surfactant slug size increases until the optimal size is reached. The optimal surfactant slug size for a single-cycle SAG process in order to divert gas away from the highest permeability layer is about 1.0^{-7} PV_{total} (≈ 0.003 m³) for the STARS model and 1.0^{-4} PV_{total} (≈ 3 m³) for the modified model by Namdar Zanganeh et al. as shown in **Figure 41** and **Figure 66** respectively. The optimal slug size, for both cases, is small. The difference in the optimal slug size between the two cases indicate that the slug size heavily depends on whether and how foam breaks as it dries out during gas injection. Additionally, the actual slug would be larger since the models used do not account for adsorption and dispersion. For the same surfactant slug size, the STARS model show higher total dimensionless pressure $P_{D_{total}}$ rise as shown in **Figure 50** and **Figure 72**. The trends in the two graphs indicate that injectivity decreases as the surfactant slug size increases. This is also reflected in the relative injection time as it takes longer to inject gas as the surfactant slug size increases as shown in **Figure 51** and **Figure 73**. For the optimal volumes in the two cases, the relative injection time for 1 PV_{total} of gas is less than the time it would take to inject a single pore volume of water in single-phase flow. This indicates that the suggested slug sizes are feasible and do not raise concerns with regard to fracturing the near wellbore region.

In case IV, zonal isolation is used during surfactant injection to isolate the lowest permeability layer (Bandera). The STARS model suggests that diversion toward the 6-md layer is feasible if all layers are filled with surfactants as displayed in **Figure 74**. Since the dimensionless pressure P_D is very high in the other layers, the 6-md layer receives the highest volume of gas as shown in **Figure 75**. However, the model predicts that the total dimensionless pressure $P_{D_{total}}$ is around 20 and injecting 1 PV_{total} takes 12 times longer than it takes to inject single phase water for the same volume. For the same scenario, the modified model of Namdar Zanganeh et al. also shows that diversion toward the Bandera layer is also feasible when all layers are filled with surfactants as displayed in **Figure 78**. Gas intake is almost uniform for the Bentheimer, Sister Berea, and the Bandera Gary layers, while the Berea layer receives the lowest volume of injected gas. The total dimensionless pressure $P_{D_{total}}$ is around 15 and the time it takes to inject 1 PV_{total} is about 10 times longer than water injection for the same volume in single-phase flow as shown in **Figure 80** and **Figure 81** respectively.

The STARS model for case IV where discrete surfactant slug sizes are injected, into all layers except Bandera, indicates that injectivity for the Bandera layer improves as the surfactant slug size increases as shown in **Figure 82** through **Figure 91**. The larger the surfactant slug, the larger the dimensionless pressure P_D build up in the other layers. A better diversion is achieved as the surfactant slug size increases until the optimal size is reached. This suggests that the larger the permeability contrast, the larger the surfactant slug

size needed for optimal diversion. The gas intake curves, **Figure 92** through **Figure 100**, show that the gas intake into the Bandera layer is almost equivalent to that in the Bentheimer layer when 1.0^{-4} PV_{total} of surfactant is used. For this surfactant slug size, the total dimensionless pressure $P_{D_{total}}$ rises to about 17 and the relative injection time is about 2.5 as shown in **Figure 102** and **Figure 103** respectively. The pattern that the total dimensionless pressure $P_{D_{total}}$ and relative time increase as the surfactant slug size increases remains similar to the previous cases.

Case IV, the modified model of Namdar Zanaganeh et al., where discrete surfactant slug sizes are used, indicates that injectivity for the Bandera layer improves much more slowly as the surfactant slug size increases compared to that predicted by the STARS model as shown in **Figure 104** through **Figure 113**. The intake curves for this case, **Figure 114** through **Figure 123**, show a similar trend. The gas intake into the Bandera layer becomes similar to that of the Bentheimer layer when 1.0^{-1} PV_{total} of surfactant is used as shown in **Figure 121**; this is about 10^3 larger than the volume predicted by the STARS model when the flow between the two layers is almost equivalent. For this surfactant slug size, the total dimensionless pressure $P_{D_{total}}$ rises to about 15 and the relative injection time is about 6.5 as shown in **Figure 124** and **Figure 125** respectively. The results in Case IV show that it is very challenging to overcome extreme permeability differences with foam. In a SAG process, if one can introduce sufficiently strong foam (highly viscous) to divert flow away from high permeability layers, injectivity is very poor.

The diversion in Kapatras et al. (2015) is modeled for linear flow as shown in **Figure 1**. For co-injection, the results are comparable to radial flow if all the layers are assumed to be filled with foam. In Kapatras et al., only 3 layers are used. The results show that superficial velocity in the Bentheimer layer is higher for all pressure gradients and for all foam qualities. Here, we show that a single-cycle SAG has much better diversion capacity as we have shown that the other layers can receive more flow than the Bentheimer, i.e. higher superficial velocities.

The goal of any EOR process is to improve the overall recovery of the field in an economically and technically feasible manner. In layered reservoirs where gas injection is implemented as a development strategy, the goal is to enhance vertical conformance by directing gas flow toward lower-permeability layers. The redistribution of gas injection improves sweep efficiency deep in the reservoir leading to higher recovery factors. However, the volumetric sweep efficiency is an overall result that depends on the injection pattern selected, off-pattern wells, fractures in the reservoir, position of gas-oil and oil/water contacts, reservoir thickness, permeability and areal and vertical heterogeneity, mobility ratio, density difference between the displacing and the displaced fluid, and flow rate.

In general, there are two mechanisms that give SAG superior performance over other foam injection methods. First, the injected surfactant slug goes into each layer according to the kh -ratio. This mechanism places larger surfactant slugs in higher-permeability zones leading to larger foam banks in these layers. However, in radial flow the near wellbore region influences flow behaviour, and this advantage decreases as the size of the slug increases. Therefore, there is an optimum slug size in our results. Second, foam is generally stronger in high-permeability zones. This allows foam to partially restrict flow in high permeability-zones resulting in gas-flow diversion toward lower-permeability zones.

One needs to keep in mind that the 1D layered radial reservoir model discussed here is highly ideal. The proposed model is not predictive. However, it is intended to give qualitative insight into the optimal design of SAG processes in layered reservoirs and highlight certain issues in the current STARS model. For foam EOR processes, the mobilities in the crucial near-well region greatly affect injectivity (Leeftink et al, 2013; Rossen and Boeije, 2015). Therefore, understanding the manner at which foam dries out during gas injection

is very crucial for correctly modelling SAG processes. In this thesis, we show how different model fits would differ from each other in their prediction of injectivity.

Field data (Ocampo et al., 2013; Rossen et al., 2014) suggest that foam behaviour for S_w close to S_{wr} is not fully captured by either model. The STARS model does not show foam collapse at S_{wr} . Additionally, the modified model of Namdar Zanganeh et al. overestimates foam collapse, leading to weaker foam and higher injectivity. We expect that foam behaviour in the field would lie in between and closer to the predicted behaviour by the modified model of Namdar Zanganeh et al. than the STARS model.

5 Conclusion and Recommendations

5.1. Conclusion

The application of real data for similar sandstone formations of different permeability to hypothetical case of four non-communicating layers, at conditions in which foam properties were measured in the lab, illustrates strengths and weaknesses of different injection methods. The effect of permeability on foam bank's mobility is different when using SAG or co-injection. Diversion in SAG depends on mobility behind shock front, which depends on foam model parameters $fmmob$, $fmdry$, $epdry$, etc. The total relative mobilities behind shock front in the four layers are different due to difference in foam model parameters. Furthermore, SAG processes have two advantages. First, prior to gas injection, the surfactant slug goes into each layer according to the kh -ratio. This places more surfactant into the high-permeability layers, leading to larger foam banks there, which improves diversion. In radial flow, since the region near wellbore becomes filled in all layers, this advantage decreases as the size of the slug increases. Therefore, there is an optimal surfactant slug size in our results. Second, foam is generally stronger in high-permeability layers, which partially restricts flow there allowing for diversion toward lower-permeability formations.

SAG process has much greater injectivity over foam injection. In SAG processes, foam effectiveness, in a given layer, decreases once gas breaks through the foam bank. The extent to which gas mobility increases depends on a combination of " $epdry$ " and " $fmmob$ " parameters. For example, the Sister Berea formation has a considerably large $epdry$ is (2nd largest) and a small $fmmob$ (the smallest). This allows the Sister Brea formation to receive higher flow than the other layers. In co-injection, greater foam strength (lower total relative mobility) in high-perm layers diverts flow toward other layers. In radial flow, this effect decreases as time goes on and foam fills near-well region in all layers.

The optimal surfactant slug size needed for diversion, in the envisaged reservoir setting, is small. The predicted optimum slug size for the modified model of Namdar Zanganeh et al. is about 10^3 times larger than that for the STARS model. The results show that injectivity is not an issue for both models when using the optimal slug size. The STARS model and the modified model by Namdar Zanaganeh et al. give different prediction for the optimal slug size due to the fact that the predicted foam behavior for the two models is radically different at saturations close to S_{wr} . Whether foam completely collapses at S_{wr} is still under research.

Flow diversion in a layered reservoir against high permeability contrast is feasible using SAG injection method. However, the needed surfactant slug size is larger and injectivity is poor. To optimize the use of surfactants and improve injectivity in low-permeability layers, it is best to isolate these zones during surfactant injection.

5.2. Recommendations

One of the major issues in the current STARS model is that foam does not collapse at residual water saturation S_{wr} . To model foam behavior appropriately, the issue of whether foam breaks at high capillary pressure needs to be resolved. Additionally, the model parameters used here were taken for foam scans conducted at room temperature. For the model to be representative, it is recommended that the scans are taken at reservoir conditions. Furthermore, the use of different initial conditions can highly affect diversion in a SAG process and should be further investigated.

Nomenclature

Φ	Potential	[Pa]	S_{gr}	Residual gas saturation	[-]
ϕ	Porosity	[%]	S_w^*	Critical water saturation	[-]
μ_α	Viscosity of phase α	[Pa.s]	S_{wc}	Connate water saturation	[-]
A	Area	[m ²]	t_D	Dimensionless time	[-]
CMC	Critical micelle concentration	[mol/L]	u_α	Superficial velocity of phase α	[m/s]
F_1	Effect of surfactant concentration	[-]	u_t	Total superficial velocity	[m/s]
F_2	Effect of water saturation	[-]	v_s	volume of surfactant slug	[m ³]
F_3	Effect of oil saturation	[-]	λ_{rt}	Total relative mobility	[-]
F_4	Effect of gas superficial velocity	[-]	λ_{rt}^f	Total relative mobility (foam)	[-]
F_5	Effect of capillary number	[-]	$\lambda_{r\alpha}$	Relative mobility phase α	[-]
f_g	Gas fractional-flow (quality)	[-]	λ_α	Mobility phase α	[Pa.s] ⁻¹
f_g^*	Transition foam quality	[-]	ρ	Density	[kg/m ³]
F_j	Volume fraction of layer 'j'	[-]	FM	Foam mobility reduction modifier	[-]
f_w	Water fractional-flow	[-]	<i>epcap</i>	Controls non-Newtonian behavior in the low quality regime	
g	Gravitational constant	[m ² /s]	<i>epdry</i>	controls abruptness of foam collapse	
h	Height	[m]	<i>fmdry</i>	Water saturations around which foam weakens	
k_{rge}	Gas relative permeability at S_{wc}	[-]	<i>fmmob</i>	Reference mobility reduction factor	
k_{rwe}	Water relative permeability at S_{gr}	[-]	IT	Implicit Texture	
$k_{r\alpha}$	Relative permeability of phase α	[-]	I.C.	Initial condition	
k_α	Absolute permeability of phase α	[m ²]	B.C.	Boundary conditions	
M	Mobility ratio	[-]	J	Injection Condition	
n_α	Corey parameter for phase α	[-]	j	Layer counter	
P	Pressure	[Pa]	LE	Local equilibrium	
P_c	Capillary pressure	[Pa]	M	Number of characteristics (saturation increments)	
P_c^*	Critical capillary pressure	[Pa]	n	Increment counter of total dimensionless time	
P_D	Dimensionless Pressure	[-]	N	Number of total dimensionless time increments	
PV	Pore volume	[m ³]	ODE	Ordinary Differential Equations	
Q_α	Volumetric flow of phase α	[m ³ /s]	PDE	Partial Differential Equations	
R	Cumulative Injectivity Ratio	[-]	PB	Population balance	
r	Radius	[m]			
r_e	External reservoir radius	[m]			
r_f	Radius of foam bank	[m]			
r_w	Wellbore radius	[m]			
S_α	Saturation of phase α	[-]			

Bibliography

- Alvarez, J.M., Rivas, H.J., and Rossen, W.R. (2001). A Unified Model for Steady-State Foam Behavior at High and Low Foam Qualities. SPE J. 6 (3): 325–333. SPE-74141-PA.
- Ashoori, E., D. Marchesin and W. R. Rossen (2011). "Roles of transient and local equilibrium foam behavior in porous media: Traveling wave." Colloids and Surfaces A: Physicochemical and Engineering Aspects 377(1–3): 228-242.
- Ashoori, E., van der Heijden, T.L.M., and Rossen, W.R., (2010). "Fractional-Flow Theory of Foam Displacements with Oil," SPE Journal 15 260-273
- Bertin, H. J. (2000). "Foam Diversion Modeling Using a Bubble-Population Correlation." SPE/DOE Improved Oil Recovery Symposium, Tulsa, OK, April 3-5. SPE-59366.
- Boeije, C. S., & Rossen, W. (2014, February 1). Gas-Injection Rate Needed for SAG Foam Processes To Overcome Gravity Override. Society of Petroleum Engineers. doi:10.2118/166244-PA
- Buckley, S. E., and M. C. Leverett, (1942). Mechanism of fluid displacement in sands, Trans. Am. Inst. Min. Metall. Pet. Eng., 146, 107–116.
- Chabert, M., L. Nabzar, V. Beunat, E. Lacombe and A. Cuenca (2014). Impact of Surfactant Structure and Oil Saturation on the Behavior of Dense CO₂ Foams in Porous Media, Society of Petroleum Engineers. SPE-169116.
- Chen, Q., M. Gerritsen and A. R. Kovscek (2010). "Modeling Foam Displacement With the Local-Equilibrium Approximation: Theory and Experimental Verification." SPE Journal 15(1): pp. 171-183.
- Cheng, L., A. B. Reme, D. Shan, D. A. Coombe and W. R. Rossen (2000). Simulating Foam Processes at High and Low Foam Qualities. SPE/DOE Improved Oil Recovery Symposium. Tulsa, Oklahoma. 3-5 April 2000. Society of Petroleum Engineers. SPE-59287
- Cheng, L., Kam, S. I., Delshad, M., & Rossen, W. R. (2001, January 1). Simulation of Dynamic Foam-Acid Diversion Processes. Society of Petroleum Engineers. doi:10.2118/68916-MS
- Computer Modeling Group Ltd. CMG-STARS User's Guide (2012). Calgary, Alberta, Canada.
- Darcy, H. (1856). Les Fontaines Publiques de la Ville de Dijon, Dalmont, Paris.
- Ettinger, R. A. and C. J. Radke (1992). "Influence of Texture on Steady Foam Flow in Berea Sandstone." SPE Reservoir Engineering 7(1): 83-90.
- Faisal, A., Bisdorn, K., Zhumabek, B., Zadeh, A. M., & Rossen, W. R. (2009, January 1). Injectivity and Gravity Segregation in WAG and SWAG Enhanced Oil Recovery. Society of Petroleum Engineers. doi:10.2118/124197-MS
- Falls, A.H., Musters, J.J., Ratulowski, J., (1989). The apparent viscosity of foams in homogeneous bead packs. SPE Reserv.Eng.4, 155–164.

- Farajzadeh, R., A. Andrianov, R. Krastev, G. Hirasaki and W. R. Rossen (2012). Foam-Oil Interaction in Porous Media: Implications for Foam Assisted Enhanced Oil Recovery, Society of Petroleum Engineers. SPE-154197.
- Farajzadeh, R., M. Lotfollahi, A. A. Eftekhari, W. R. Rossen and G. J. Hirasaki (2015). "Effect of permeability on foam-model parameters and the limiting capillary pressure." TIPM.
- Farajzadeh, R., R. M. Muruganathan, R. Krastev and W. R. Rossen (2010). Effect Of Gas Type On Foam Film Permeability And Its Implications For Foam Flow In Porous Media, Society of Petroleum Engineers. SPE-131297.
- Fisher, A. W., R. W. S. Foulser and S. G. Goodyear (1990). Mathematical Modeling of Foam Flooding, Society of Petroleum Engineers. SPE-20195.
- Hirasaki, G.J., Lawson, J.B., (1985). Mechanisms of foam flow through porous media –apparent viscosity in smooth capillaries. SPE J.25, 176–190
- Islam, M. R. and Farouq-Ali, S. M., (July-Aug. 1990). "Numerical Simulation of Foam Flow in Porous Media," J. Canadian. Pet. Tech. 47-51.
- Kam, S. I., Q. P. Nguyen, Q. Li and W. R. Rossen (2007). "Dynamic Simulations With an Improved Model for Foam Generation." SPE Journal 12(1): pp. 35-48.
- Kapetas, L., S. Vincent-Bonnieu, R. Farajzadeh, A.A. Eftekhari, S.R. Mohd-Shafian, R.Z. Kamarul Bahrim and W.R. Rossen (2015, 14-16 April). "Effect of Permeability on Foam-model parameters - An Integrated Approach from Coreflood Experiments through to Foam Diversion Calculations," 18th European Symposium on Improved Oil Recovery, Dresden, Germany.
- Kapetas, L., S. Vincent-Bonnieu, S. Danelis, W. R. Rossen, R. Farajzadeh, A. A. Eftekhari, S. R. Mohd-Shafian and R. Z. Kamarul-Bahrim (2015). "Effect of temperature on foam flow in porous media." 19th MEOS conference, Bahrain, SPE 172820
- Khatib, Z. I., Hirasaki, G. J. and Falls, A. H., (1988). "Effects of Capillary Pressure on Coalescence and Phase Mobilities in Foams Flowing through Porous Media", SPE Reser. Eng. 3, 919-926.
- Kibodeaux, K. R., & Rossen, W. R. (1997, January 1). Coreflood Study of Surfactant-Alternating-Gas Foam Processes: Implications for Field Design. Society of Petroleum Engineers. doi:10.2118/38318-MS
- Kloet, M. B., Renkema, W. J., and Rossen, W. R., "Optimal Design Criteria for SAG Foam Processes in Heterogeneous Reservoirs," SPE 121581 presented at the 2009 SPE EUROPEC/EAGE Annual Conference and Exhibition, Amsterdam, The Netherlands, 8–11 June.
- Kovscek, A. R. and Radke, C. J., "Fundamentals of Foam Transport in Porous Media," in Foams: Fundamentals and Applications in the Petroleum Industry, L.L. Schramm (ed.) ACS Advances in Chemistry Series, Am. Chem. Soc., Washington, D.C. (1994) 3, No. 242.
- Kovscek, A. R., T. W. Patzek and C. J. Radke (1995). "A mechanistic population balance model for transient and steady-state foam flow in Boise sandstone." Chemical Engineering Science 50(23): 3783-3799.

- Kovscek, A. R., W. P. Tadeusz and C. J. Radke (1995). "Mechanistic Foam Flow Simulation in Heterogeneous and Multidimensional Porous Media." *SPE Journal*, Volume 2, December 1997: 511-526.
- Kuhlman, M. I. (1990). "Visualizing the Effect of Light Oil on CO₂ Foams." Society of Petroleum Engineers. SPE-17356
- Kular, G. S., Lowe, K., and Coombe, D., "Foam Application in an Oil Sands Steam Flood Process," SPE 19690 presented at the 1989 SPE Annual Tech. Conf. and Exhibition, San Antonio, TX, Oct. 8-11.
- Lake, L.W., Johns, R.T., Rossen, W.R., Pope, G.A., (2014). *Fundamentals of Enhanced Oil Recovery*. Society of Petroleum Engineers, Richardson, TX.
- Lau, H. C., Oapos and S. M. Brien (1988). "Effects of Spreading and Nonspreading Oils on Foam Propagation Through Porous Media." Society of Petroleum Engineers. SPE-15668
- Law, D. H. S. (1989). An Optimization Study For A Steam-Foam Drive Process In The Bodo Reservoir, Alberta, Canada, Petroleum Society of Canada. PETSOC-SS-89-17
- Le, V. Q., Nguyen, Q. P. and Sanders, A. W., "A Novel Foam Concept with CO₂ Dissolved Surfactants," SPE 113370 presented at the 2008 SPE/DOE Symposium on Improved Oil Recovery, Tulsa, Oklahoma, USA, 20-23 April.
- Liu, Y., R. B. Grigg and B. Bai (2005). Salinity, pH , and Surfactant Concentration Effects on CO₂-Foam, Society of Petroleum Engineers. SPE-93095.
- Ma, K., Ren, G., Mateen, K., Morel, D., & Cordelier, P. (2014, April 12). Literature Review of Modeling Techniques for Foam Flow Through Porous Media. Society of Petroleum Engineers. doi:10.2118/169104-MS
- Ma, K., Ren, G., Mateen, K., Morel, D., & Cordelier, P. (2014, April 12). Literature Review of Modeling Techniques for Foam Flow Through Porous Media. Society of Petroleum Engineers. doi:10.2118/169104-MS
- Mannhardt, K., L. L. Schramm and J. J. Novosad (1993). "Effect of Rock Type and Brine Composition on Adsorption of Two Foam-Forming Surfactants." SPE-20463
- Mohammadi, S., and Coombe, D. A., "Characteristics of Steam-Foam Drive Process in Massive Multi-Zone and Thin Single-Zone Reservoirs," SPE 24030, presented at the 1992 SPE Western Regional Meeting, Bakersfield, CA, March 30-April 1.
- Nikolov, A.D., Wasan, D.T., Huang, D.W. and Edwards, D.A. (1986), 'The Effect of Oil on Foam Stability: Mechanisms and Implications for Oil Displacement by Foam in Porous Media', Paper Presented at of the 61st Annual Technical Conference and Exhibition of Society of Petroleum Engineers, October 5-8, 1986. New Orleans, LA, USA, SPE 15443.
- Ocampo, A., Restrepo, A., Cifuentes, H., Hester, J., Orozco, N., Gil, C., Gonzalez, C. (2013, March 26). Successful Foam EOR Pilot in a Mature Volatile Oil Reservoir Under Miscible Gas Injection. International Petroleum Technology Conference. doi:10.2523/16984-MS

- Osterloh, W. T. and M. J. Jante Jr. (1992). Effects of Gas and Liquid Velocity on Steady-State Foam Flow at High Temperature. SPE/DOE Enhanced Oil Recovery Symposium. Tulsa, Oklahoma. 22- 24 April 1992. Society of Petroleum Engineers. SPE-24179
- Patzek, T. W. (1988). Description of Foam Flow in Porous Media by the Population Balance Method. Surfactant-Based Mobility Control, American Chemical Society. 373: 326-341.
- Patzek, T. W. (1988). Description of Foam Flow in Porous Media by the Population Balance Method. Surfactant-Based Mobility Control, American Chemical Society. 373: 326-341.
- Patzek, T. W. and N. A. Myhill (1989). Simulation of the Bishop Steam Foam Pilot, Society of Petroleum Engineers. SPE-18786
- Pope, G. A. (1980, June 1). The Application of Fractional Flow Theory to Enhanced Oil Recovery. Society of Petroleum Engineers. doi:10.2118/7660-PA
- Rossen, W. R., & Wang, M. W. (1999, June 1). Modelling Foams for Acid Diversion. Society of Petroleum Engineers. doi:10.2118/56396-PA
- Rossen, W. R., Ocampo-Florez, A. A., Restrepo, A., Cifuentes, H. D., & Marin, J. (2014, October 27). Long-Time Diversion in SAG Foam Enhanced Oil Recovery From Field Data. Society of Petroleum Engineers. doi:10.2118/170809-MS
- Rossen, W. R., van Duijn, C. J., Nguyen, Q. P., Shen, C., and Vikingstad, A. K., "Injection Strategies to Overcome Gravity Segregation in Simultaneous Gas and Water Injection Into Homogeneous Reservoirs," SPE Journal 15, 76-90 (2010).
- Rossen, W., & Boeije, C. S. (2015, May 1). Fitting Foam-Simulation-Model Parameters to Data: II. Surfactant-Alternating-Gas Foam Applications. Society of Petroleum Engineers. doi:10.2118/165282-PA
- Schramm, L. L. (1994). Foams: Fundamentals and Applications in the Petroleum Industry, American Chemical Society. 242.
- Shan, D. and Rossen, W. R., "Optimal Injection Strategies for Foam IOR," SPE Journal 9, 132-150 (2004).
- Simjoo, M. and P. L. J. Zitha (2013). Effects of Oil on Foam Generation and Propagation in Porous Media, Society of Petroleum Engineers. SPE-165271.
- Simjoo, M., M. N. Mahmoodi and P. L. J. Zitha (2009). Effect of Oil Saturation on Foam for Acid Diversion, Society of Petroleum Engineers. SPE-122152.
- Stone, H. L. (2004, January 1). A Simultaneous Water and Gas Flood Design with Extraordinary Vertical Gas Sweep. Society of Petroleum Engineers. doi:10.2118/91724-MS
- Stone, H. L.: "A Simultaneous Water and Gas Flood Design with Extraordinary Vertical Gas Sweep," SPE 91724 presented at the 2004 SPE International Petroleum Conference in Mexico, Puebla Pue., Mexico, 7-9 Nov. Xu, Q., and Rossen, W. R., "Experimental Study of Gas Injection in Surfactant-Alternating
- Tang, G.Q., Kovscek, A.R., 2006. Trapped gas fraction during steady-state foam flow. Transp. Porous Med. 65, 287–307.

- Tsau, J.-S., Syahputra, A.E., and Grigg, R.B. 2000. Economic Evaluation of Surfactant Adsorption in CO₂ Foam Application. Presented at the SPE/DOE Improved Oil Recovery Symposium, Tulsa, Oklahoma, 3-5 April 2000. SPE-59365-MS.
- W. R. Rossen, "Foams in Enhanced Oil Recovery," in R. K. Prud'homme and S. Khan, ed., *Foams: Theory, Measurements and Applications*, Marcel Dekker, New York, 1996, pp. 413-464.
- Walsh, M.P. and Lake, L.W., 1989. Applying fractional flow theory to solvent flooding and chase fluids. *J. Pet. Sci. Eng.*, 2: 281-303.
- Xu, Q., Rossen, W.R., 2003. Effective viscosity of foam in periodically constricted tubes. *Colloids Surf. A: Physicochem. Eng. Asp.* 216, 175–194.
- Zanganeh, M. N., Kam, S. I., LaForce, T., & Rossen, W. R. (2011, March 1). The Method of Characteristics Applied to Oil Displacement by Foam. Society of Petroleum Engineers. doi:10.2118/121580-PA
- Zhou, Z. H., & Rossen, W. R. (1994, February 1). Applying Fractional-Flow Theory to Foams for Diversion in Matrix Acidization. Society of Petroleum Engineers. doi:10.2118/24660-PA
- Zhou, Z., & Rossen, W. R. (1995, March 1). Applying Fractional-Flow Theory to Foam Processes at the "Limiting Capillary Pressure." Society of Petroleum Engineers. doi:10.2118/24180-PA
- Zitha, P. L. J. (2006). A New Stochastic Bubble Population Model for Foam in Porous Media. SPE/DOE Symposium on Improved Oil Recovery. Tulsa, Oklahoma, USA, Society of Petroleum Engineers. SPE-98976.

Appendix A: Tables

Layer		$fmmob$	$epdry$	$fmdry$
1	Bentheimer	47,700	400	0.271
2	Berea	869,000	19,600	0.336
3	Sister Berea	30,700	8,890	0.396
4	Bandera	68,200	152	0.549

Table 1: Foam Model Parameters (Kapetas et al., 2015)

Layer		k_{rwe}	n_w	k_{rge}	n_g
1	Bentheimer	0.39	2.86	0.59	0.70
2	Berea	0.39	4.09	0.99	1.97
3	Sister Berea	0.14	5.25	0.47	1.22
4	Bandera	1.00	3.56	0.73	2.43

Table 2: Corey Relative Permeability Parameters

Layer		k_i [md]	ϕ [-]	h_i [m]	$\frac{k_i h_i}{\sum k_i h_i}$
1	Bentheimer	1900	0.24	1.000	0.8648
2	Berea	90	0.20	1.200	0.0492
3	Sister Berea	160	0.21	1.143	0.0832
4	Bandera Gray	6	0.23	1.043	0.0028

Table 3: Permeability, Porosity, Height, and kh -ratio

Layer	$S_{w,shock}$	$\left(\frac{df_w}{dS_w}\right)_{S_{w,shock}}$	$(\lambda_{rt})_{S_{w,shock}}$	S_{wr}	$(\lambda_{rt})_{S_{wr}}$
Bentheimer	0.78	4.06	3,195	0.25	29,500
Berea	0.79	3.94	1,268	0.23	49,500
Sister Berea	0.71	3.18	1,132	0.25	23,500
Bandera Gray	0.88	5.82	1,391	0.46	36,500

Table 4: Shock Saturation, Total Relative Mobilities and Velocities (gas without surfactant)

Layer	$S_{w,shock}$	$\left(\frac{df_w}{dS_w}\right)_{S_{w,shock}}$	$(\lambda_{rt})_{S_{w,shock}}$	S_{wr}	$(\lambda_{rt})_{S_{wr}}$
Bentheimer	0.26603	1.35719	4.10101	0.25	16.4
Berea	0.32820	1.47577	19.96683	0.23	369.0
Sister Berea	0.39294	1.63988	43.43829	0.25	2755.3
Bandera Gray	0.50728	1.98985	8.77428	0.46	22.8

Table 5: Shock Saturation, Total Relative Mobilities and Velocities for SAG Injection

Layer	$S_{w,shock}$	$\left(\frac{df_w}{dS_w}\right)_{S_{w,shock}}$	$(\lambda_{rt})_{S_{w,shock}}$	S_{wr}	$(\lambda_{rt})_{S_{wr}}$
Bentheimer	0.26634	1.35856	5.10093	0.25	29,500
Berea	0.32827	1.47670	21.32684	0.23	49,500
Sister Berea	0.39295	1.64003	44.31117	0.25	23,500
Bandera Gray	0.51139	2.01160	13.49425	0.46	36,500

Table 6: Shock Saturation, Total Relative Mobilities and Velocities for SAG Injection – Namdar Zanganeh et al. Modified Model

Layer	$(M)_{Gas\ w/o\ surf.}$	$(M)_{SAG-STARS}$	$(M)_{SAG-N.Z.\ et\ al.}$
Bentheimer	3.195	0.004	0.005
Berea	1.268	0.020	0.021
Sister Berea	1.132	0.043	0.044
Bandera Gray	1.391	0.009	0.013

Table 7: Mobility Ratio at Flood Front for all Formations

Layer	$(\lambda_{rt})_{shock}$	$k_{rw}(fmdry)$	$fmdry$	$epdry$	$fmmob$
Bentheimer	4.1	3.43E-05	0.271	400	47,700
Berea	20.0	2.34E-04	0.336	19,600	869,000
Sister Berea	43.4	2.18E-04	0.396	8,890	30,700
Bandera Gray	8.8	1.60E-03	0.549	152	68,200

Table 8: Total Relative Mobility at the Shock for the STARS Model, Water Relative Permeability at $fmdry$, and Foam Model Parameters

Formation	Permeability [md]	
	SCAL	Foam Scan
Bentheimer	773	1900
Berea	137	90
Sister Berea	116	160
Bandera Gray	13	6

Table 9: Differences in Permeability between Cores used for SCAL Measurements and Foam Scans

	V_1	V_2	V_3	V_4	V_5	V_6	V_7	V_8	V_9	V_{10}
	1.0^{-8}	1.0^{-7}	1.0^{-6}	1.0^{-5}	1.0^{-4}	1.0^{-3}	1.0^{-2}	1.0^{-1}	1.0^0	10.0^1
	$r_s(V_1)$	$r_s(V_2)$	$r_s(V_3)$	$r_s(V_4)$	$r_s(V_5)$	$r_s(V_6)$	$r_s(V_7)$	$r_s(V_8)$	$r_s(V_9)$	$r_s(V_{10})$
Bentheimer	1.02E-01	1.16E-01	2.11E-01	5.97E-01	1.86E+00	5.88E+00	1.86E+01	5.88E+01	1.00E+02	1.00E+02
Berea	1.00E-01	1.01E-01	1.09E-01	1.72E-01	4.55E-01	1.41E+00	4.44E+00	1.40E+01	4.43E+01	1.00E+02
Sister Berea	1.00E-01	1.02E-01	1.15E-01	2.08E-01	5.86E-01	1.83E+00	5.77E+00	1.82E+01	5.77E+01	1.00E+02
Bandera Gray	1.00E-01	1.00E-01	1.01E-01	1.06E-01	1.46E-01	3.52E-01	1.07E+00	3.38E+00	1.07E+01	3.38E+01
	$r_f(V_1)$	$r_f(V_2)$	$r_f(V_3)$	$r_f(V_4)$	$r_f(V_5)$	$r_f(V_6)$	$r_f(V_7)$	$r_f(V_8)$	$r_f(V_9)$	$r_f(V_{10})$
Bentheimer	1.06E-01	1.51E-01	3.71E-01	1.13E+00	3.57E+00	1.13E+01	3.57E+01	1.00E+02	1.00E+02	1.00E+02
Berea	1.00E-01	1.04E-01	1.31E-01	2.87E-01	8.58E-01	2.70E+00	8.52E+00	2.69E+01	8.52E+01	1.00E+02
Sister Berea	1.01E-01	1.06E-01	1.49E-01	3.64E-01	1.11E+00	3.51E+00	1.11E+01	3.50E+01	1.00E+02	1.00E+02
Bandera Gray	1.00E-01	1.00E-01	1.02E-01	1.19E-01	2.28E-01	6.56E-01	2.05E+00	6.49E+00	2.05E+01	6.49E+01

Table 10: Radii of Surfactant Bank and Foam Bank for Different Surfactant Slug Sizes

Appendix B: Diagrams

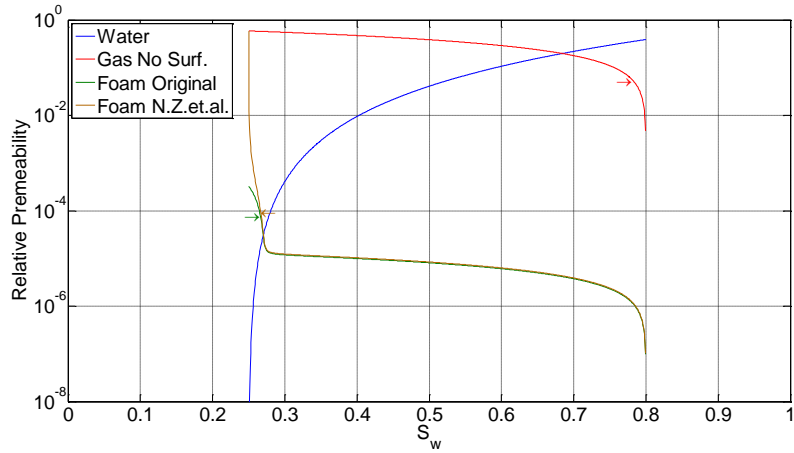


Figure 126: Relative Permeabilities vs. Water Saturation (Bentheimer)

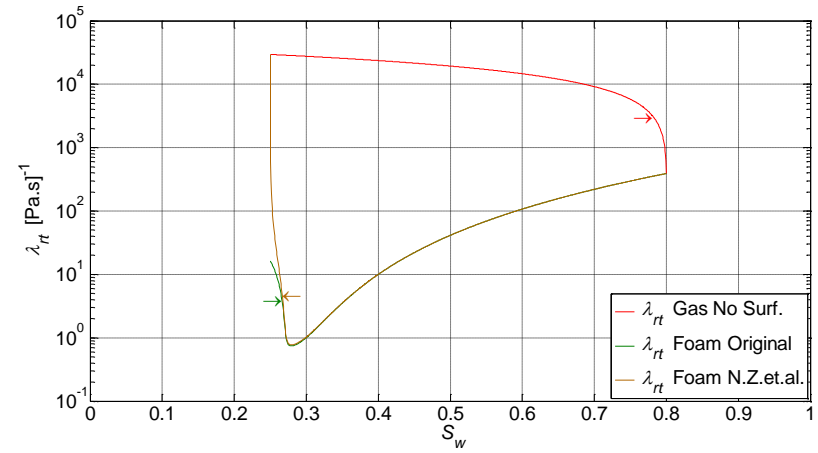


Figure 128: Total Relative Mobility vs. Water Saturation (Bentheimer)

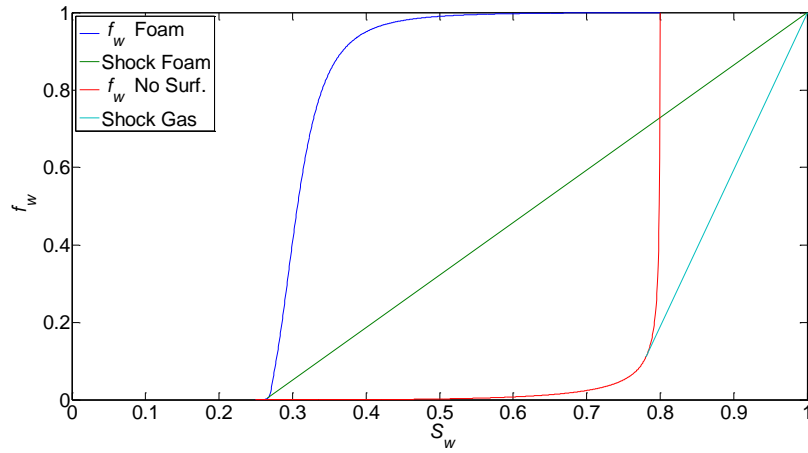


Figure 127: Fractional Flow Curves and Shocks (Bentheimer)

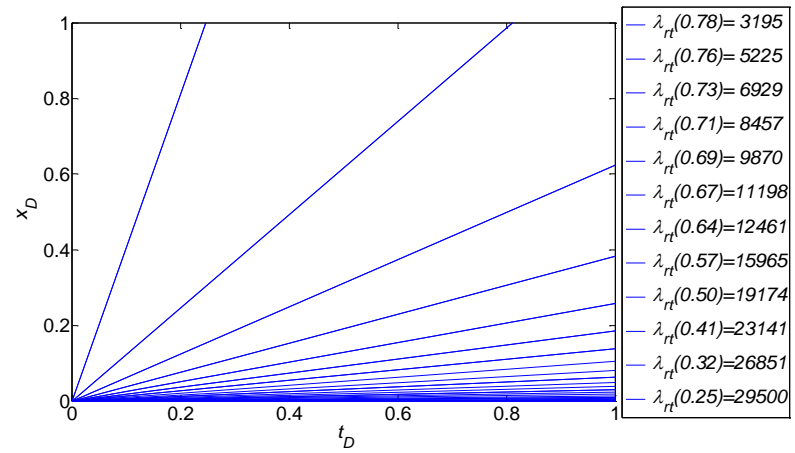


Figure 129: Time-Distance Diagram for Gas without Surfactant (Bentheimer)

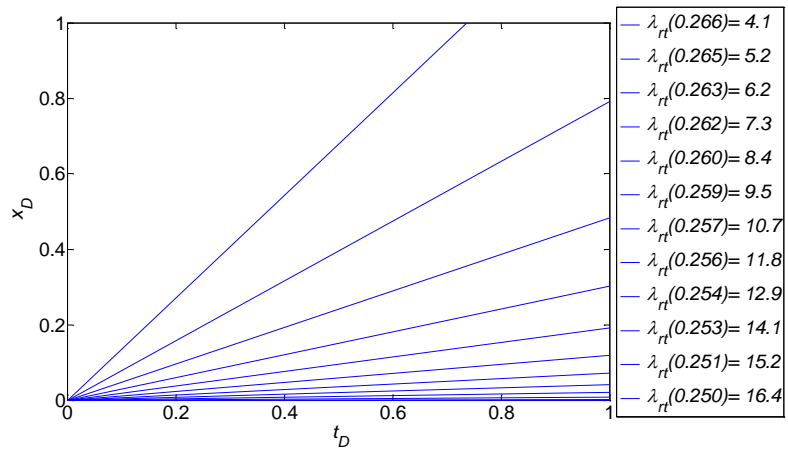


Figure 130: Time-Distance Diagram for SAG STARS Model (Bentheimer)

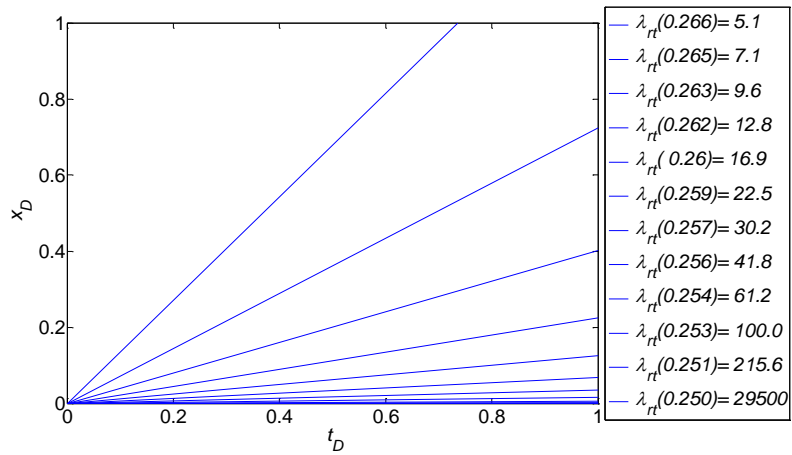


Figure 131: Time-Distance Diagram for SAG N.Z. et al. Modified Model (Bentheimer)

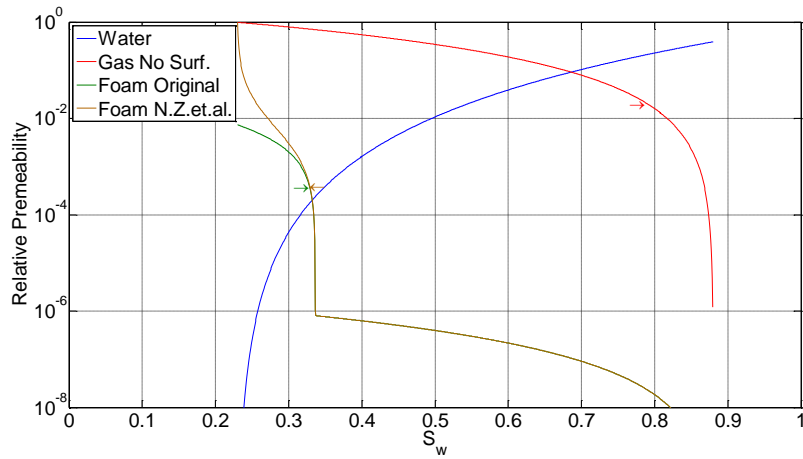


Figure 132: Relative Permeabilities vs. Water Saturation (Berea)

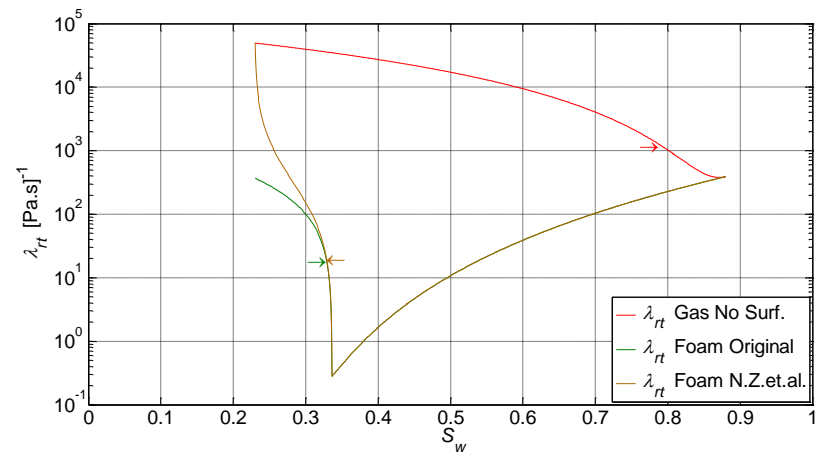


Figure 134: Total Relative Mobility vs. Water Saturation (Berea)

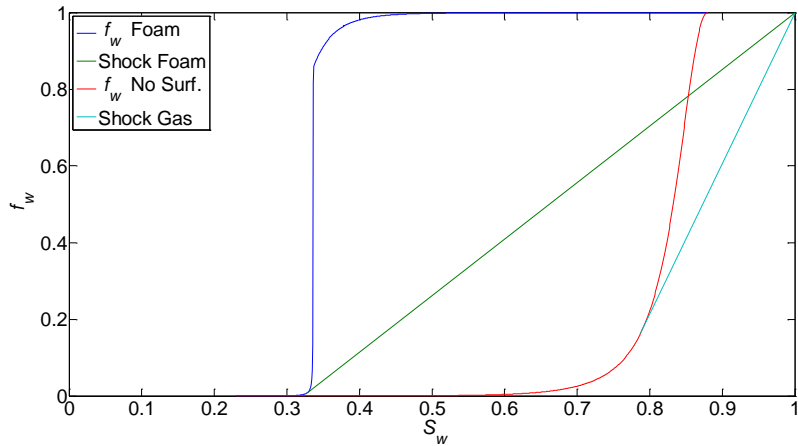


Figure 133: Fractional Flow Curves and Shocks (Berea)

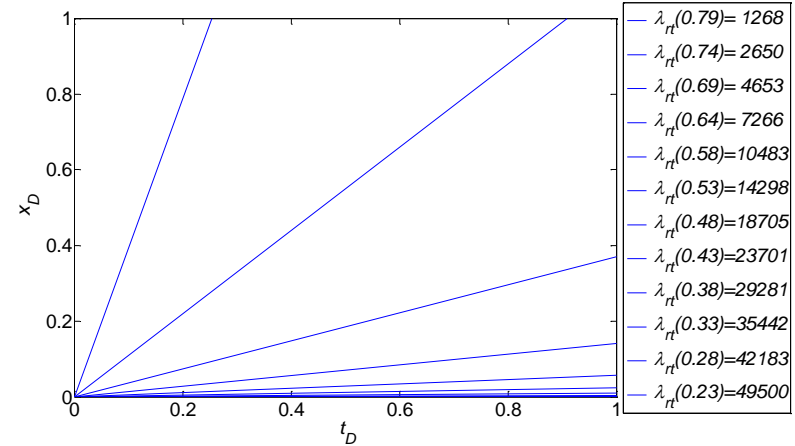


Figure 135: Time-Distance Diagram for Gas without Surfactant (Berea)

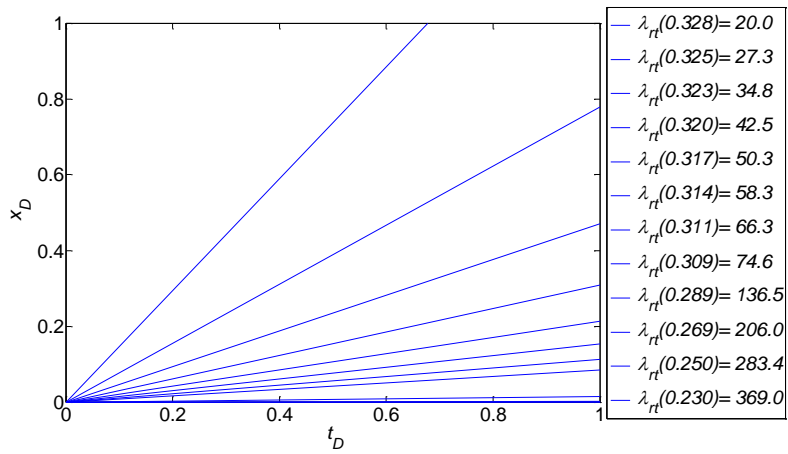


Figure 136: Time-Distance Diagram for SAG STARS Model (Berea)

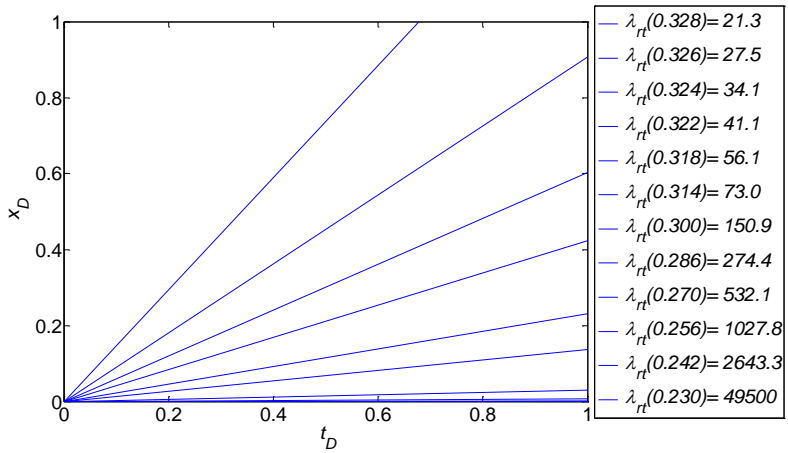


Figure 137: Time-Distance Diagram for SAG N.Z. et al. Modified Model (Berea)

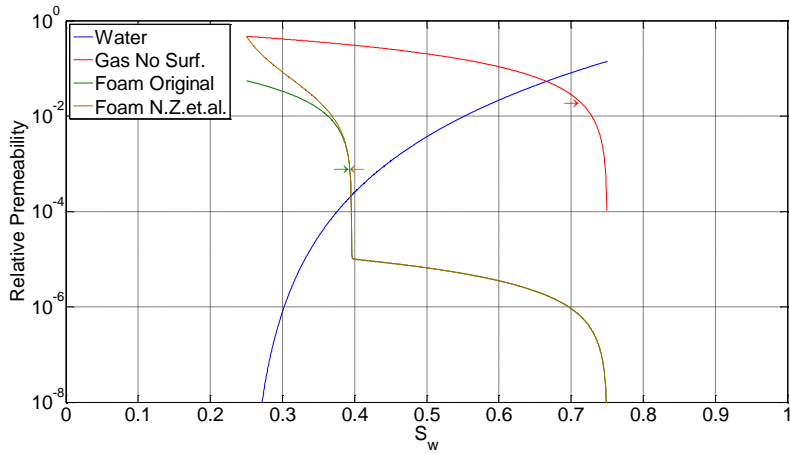


Figure 138: Relative Permeabilities vs. Water Saturation (Sister Berea)

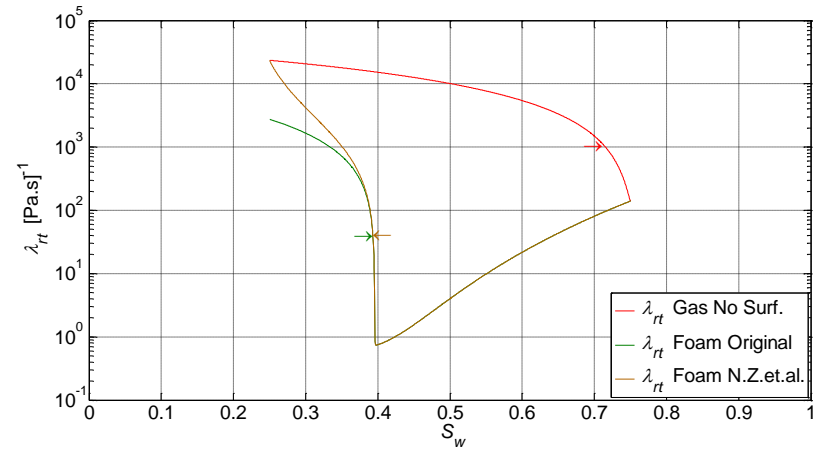


Figure 140: Total Relative Mobility vs. Water Saturation (Sister Berea)

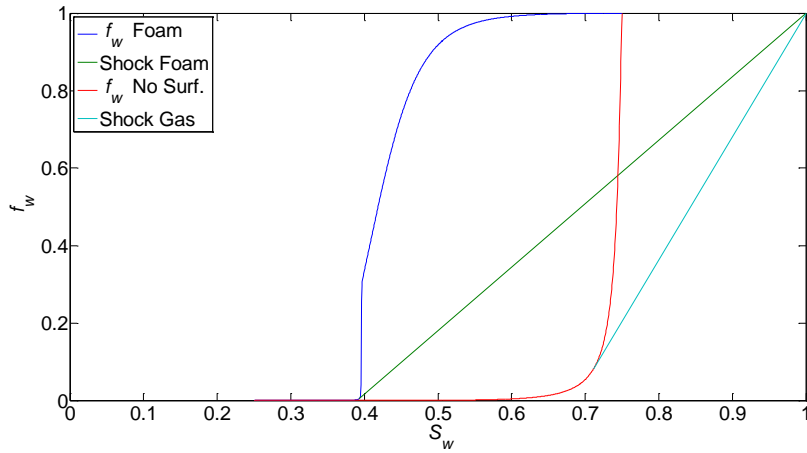


Figure 139: Fractional Flow Curves and Shocks (Sister Berea)

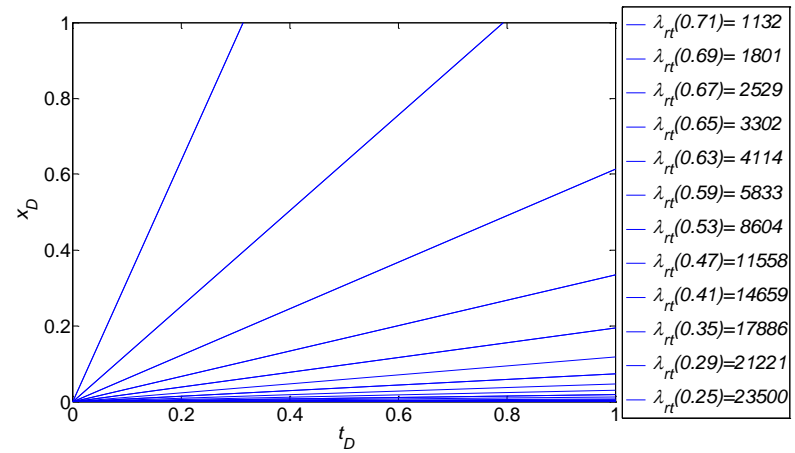


Figure 141: Time-Distance Diagram for Gas without Surfactant (Sister Berea)

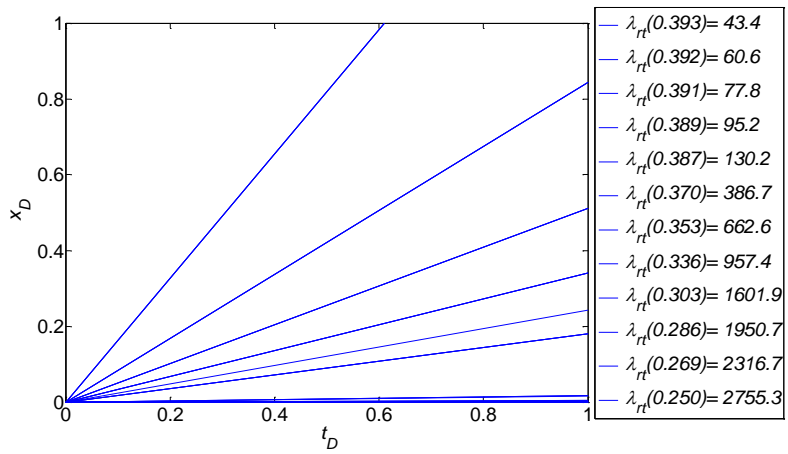


Figure 142: Time-Distance Diagram for SAG STARS Model (Sister Berea)

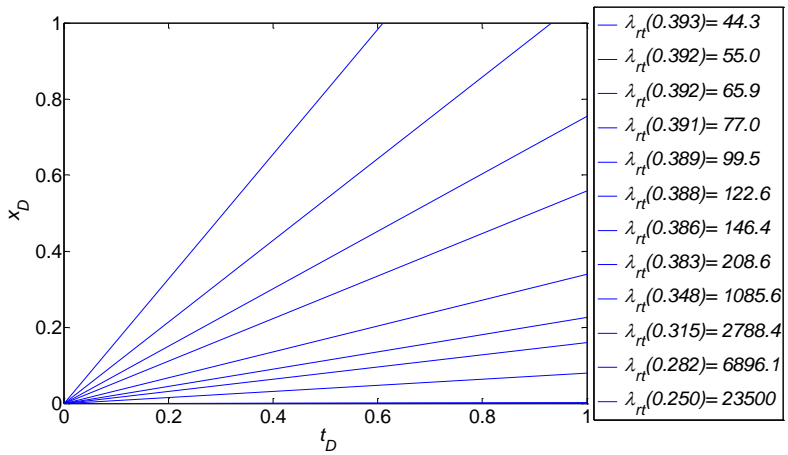


Figure 143: Time-Distance Diagram for SAG N.Z. et al. Modified Model (Sister Berea)

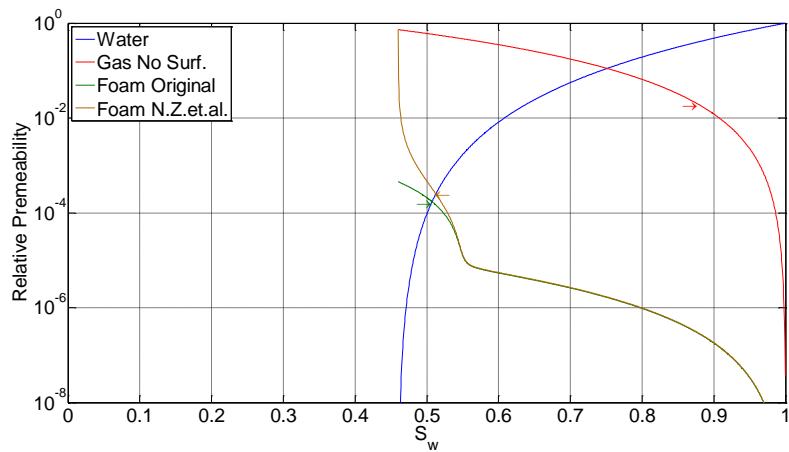


Figure 144: Relative Permeabilities vs. Water Saturation (Bandera Gray)

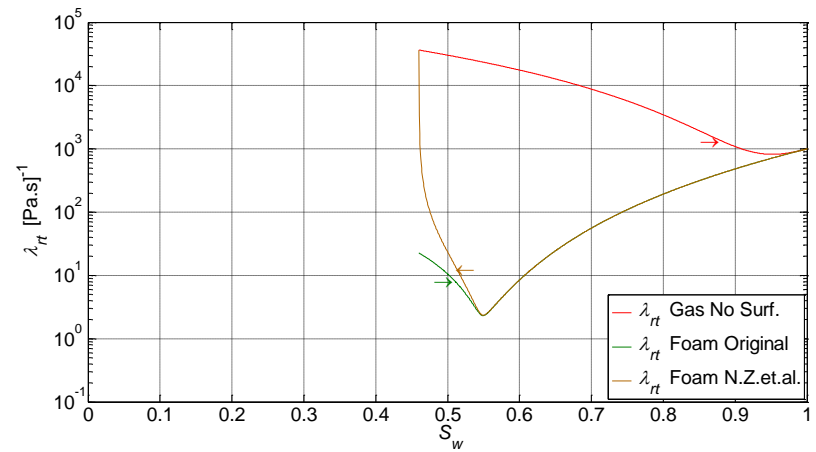


Figure 146: Total Relative Mobility vs. Water Saturation (Bandera Gray)

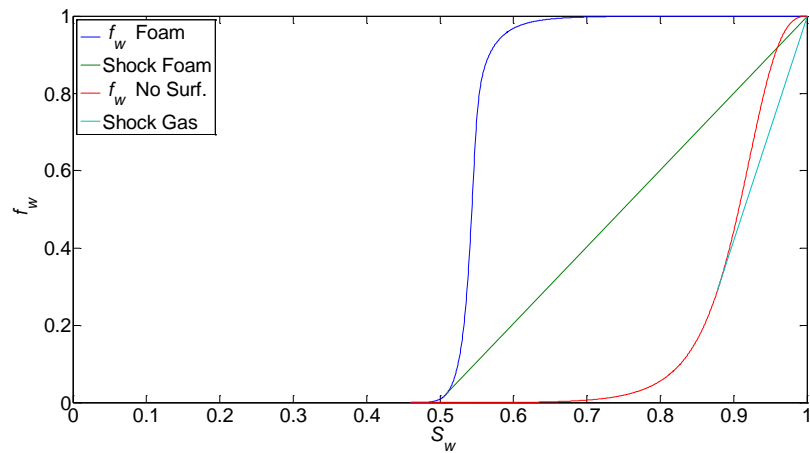


Figure 145: Fractional Flow Curves and Shocks (Bandera Gray)

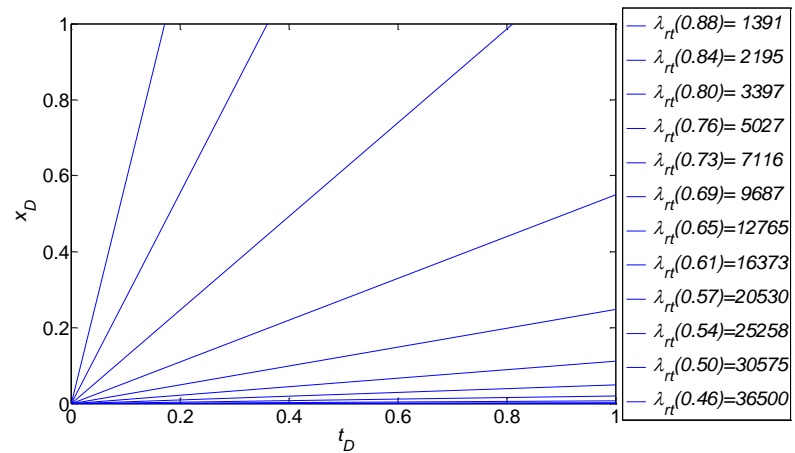


Figure 147: Time-Distance Diagram for Gas without Surfactant (Bandera Gray)

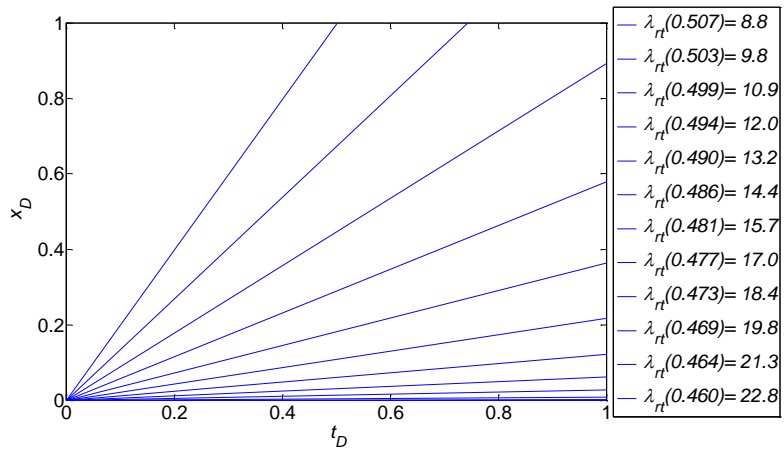


Figure 148: Time-Distance Diagram for SAG STARS Model (Bandera Gray)

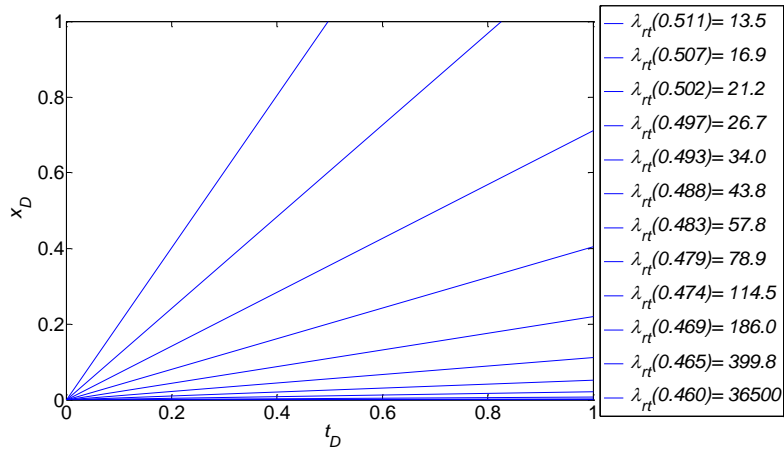
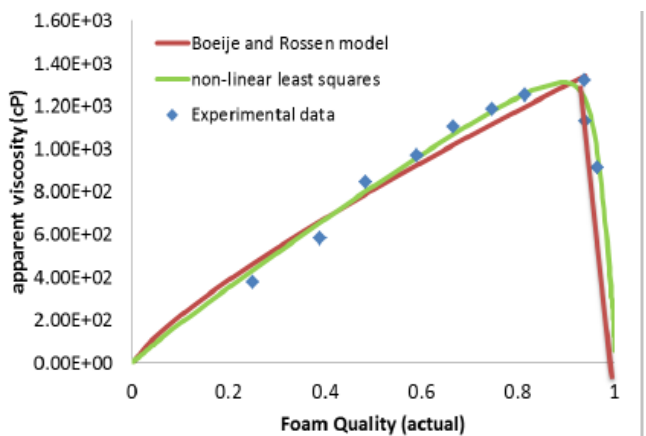
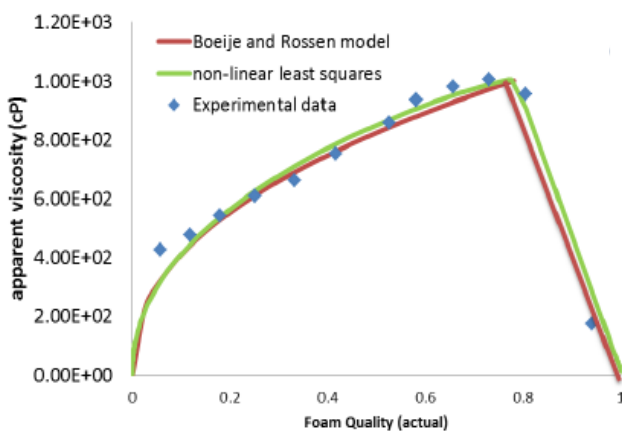


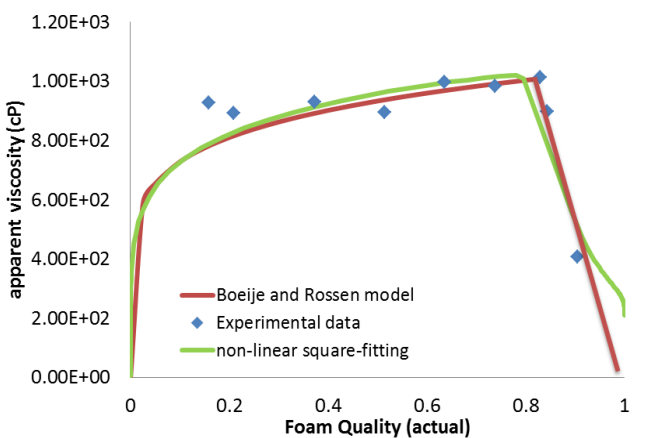
Figure 149: Time-Distance Diagram for SAG N.Z. et al. Modified Model (Bandera Gray)



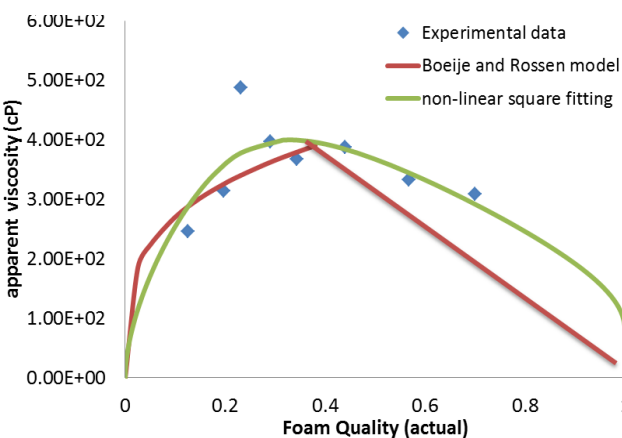
Bentheimer, 1900 mD, $u_f = 4.24$ ft/day



Berea, 90 mD, $u_f = 0.671$ ft/day



Sister Berea, 160mD, $u_f = 0.769$ ft/day



Bandera Grey, 6 mD, $u_f = 0.0716$ ft/day

Figure 150: Steady-State Foam Scans for Cores Taken from all Formations at Different Total Superficial Velocities Kapetas et al. (2015)

Appendix C: Matlab Code

Function I: Dimensionless Pressure Estimation for Gas Injection without surfactant

```
function [ PD ] = F1(tD,krwe,nw,krge,ng,swr,sgr,re,rw,j)
mug = 2e-5;
muw = 1e-3;
swe = @(sw) (sw-swr)/(1-swr-sgr); % effective water saturation
krw = @(sw) (krwe*swe(sw).^nw); % water relative permeability
lambda_w = @(sw) (krw(sw)./muw); % water relative mobility
krg = @(sw) (krge*(1-swe(sw)).^ng); % gas relative permeability
lambda_g = @(sw) (krg(sw)./mug); % gas relative mobility
% fractional Flow of Water for Gas Injection
fw2 = @(sw) (1./(1+(lambda_g(sw))./(lambda_w(sw))));
% derivative of water relative permeability
dkrw = @(sw) ((nw*krwe*swe(sw).^(nw-1))./(1-swr-sgr));
% derivative of water relative mobility
dlambda_w = @(sw) (real(dkrw(sw)./muw));
% derivative of gas relative permeability
dkrg = @(sw) (-(krge*ng*(1-swe(sw)).^(ng-1))./(1-swr-sgr));
% derivative of gas relative mobility
dlambda_g = @(sw) (dkrg(sw)./mug);
% derivative of the fractional flow curve for gas (dfw,g/dSw)
dfw2 = @(sw) ((lambda_g(sw).*dlambda_w(sw) -
lambda_w(sw).*dlambda_g(sw))./(lambda_g(sw)+lambda_w(sw)).^2);
% total relative mobility for gas injection
lambda_rt2 =@(sw) (lambda_w(sw)+lambda_g(sw));
% shock saturation determination
F2 = @(sw) (fw2(sw)+ dfw2(sw).*(1-sw)-1);
% water saturation at the shock gas injection
sw_shock2 = fzero(F2, [swr+eps, 1-sgr-0.001]);
% range of water saturation experienced for gas injection
m2 = linspace(swr,sw_shock2(j),201);
N2 = length (m2);
i=1;
% dimensionless position gas injection
xD2 = @(sw) (min((tD).*dfw2(sw),1));
% radial position gas injection
r2 = @(sw) (sqrt(xD2(sw).*(re^2-rw^2)+rw^2));
% Pressure drop in the gas bank
P2(i:N2-1) = log(r2(m2(i+1:N2))./r2(m2(i:N2-1))).*(0.5*(1./lambda_rt2(m2(i+1:N2))+1./lambda_rt2(m2(i:N2-1))));
% Pressure drop in the water bank
P2(N2) = log(re./r2(m2(N2)))*muw;
```

```
% dimensionless pressure calculation
```

```
PD = (sum(P2))/(muw*log(re/rw));
```

```
end
```

Function II: Dimensionless Pressure Estimation for SAG Injection

```
function [ PD ] = F2(tD,krwe,nw,krge,ng,swr,sgr,fmmob,fmdry,epdry,rw,re,j)
```

```
%% fluid properties
```

```
muw = 1e-3;
```

```
mug = 2e-5;
```

```
swe = @(sw) (sw-swr)/(1-swr-sgr); % effective water saturation
```

```
krw = @(sw) (krwe*swe(sw).^nw); % water relative permeability
```

```
lambda_w = @(sw) (krw(sw)./muw); % water relative mobility
```

```
krge = @(sw) (krge*(1-swe(sw)).^ng); % gas relative permeability
```

```
lambda_g = @(sw) (krge(sw)./mug); % gas relative mobility
```

```
% foam Mobility Reduction Factor (STARS Model)
```

```
FM = @(sw) (1+fmmob*(0.5+ atan(epdry.*(sw-fmdry))/pi()));
```

```
% foam Mobility Reduction Factor (N.Z.et al. Model)
```

```
% FM = @(sw) (1+fmmob*((0.5+ atan(epdry.*(sw-fmdry))/pi())-(0.5+ atan(epdry.*(swr-fmdry))/pi())));
```

```
krgf = @(sw) (krge(sw)./FM(sw)); % foam relative permeability
```

```
lambda_f = @(sw) (real(krgf(sw)./mug)); % foam relative mobility
```

```
% fractional Flow of Water for SAG
```

```
fw = @(sw) (1./(1+(lambda_f(sw))./(lambda_w(sw))));
```

```
% derivative of water relative permeability
```

```
dkrw = @(sw) ((nw*krwe*swe(sw).^(nw-1))./(1-swr-sgr));
```

```
% derivative of water relative mobility
```

```
dlambda_w = @(sw) (real(dkrw(sw)./muw));
```

```
% derivative of gas relative permeability
```

```
dkrg = @(sw) (-(krge*ng*(1-swe(sw)).^(ng-1))./(1-swr-sgr));
```

```
% derivative of gas relative mobility
```

```
dlambda_g = @(sw) (dkrg(sw)./mug);
```

```
% derivative of foam mobility reduction factor
```

```
dFM = @(sw) ((fmmob*epdry)./(pi*(1+(epdry^2*(sw-fmdry).^2))));
```

```
% derivative of foam relative permeability
```

```
dkrgf = @(sw) ((dkrg(sw).*FM(sw)-dFM(sw).*krge(sw))./(FM(sw).^2);
```

```
% derivative of foam relative mobility
```

```
dlambda_f = @(sw) (dkrgf(sw)./mug);
```

```
% derivative of the fractional flow curve for foam (dfw,f/dSw)
```

```
dfw = @(sw) ((lambda_f(sw).*dlambda_w(sw) -  
dlambda_f(sw).*lambda_w(sw))./(lambda_f(sw)+lambda_w(sw)).^2);
```

```
% total relative mobility for SAG injection
```

```
lambda_rt = @(sw) (lambda_w(sw)+lambda_f(sw));
```

```
% determination of the shock saturations
```

```
F = @(sw) (fw(sw)+ dfw(sw).*(1-sw)-1);
```

```
% water saturation at the shock SAG injection
```

```

sw_shock = fzero(F, [swr+eps,0.6]);

% range of water saturation experienced for SAG injection
m = linspace(swr,sw_shock(j),101);
N = length (m);
i=1;
% dimensionless position for SAG
xD = @(sw) (min(tD.*dfw(sw),1));
% radial position for SAG
r = @(sw) (sqrt(xD(sw).*(re^2-rw^2)+rw^2));
% Pressure Drop in the foam bank
P(i:N-1) = log(r(m(i+1:N))./r(m(i:N-1))).*(0.5*(1./lambda_rt(m(i+1:N))+1./lambda_rt(m(i:N-1))));
% Pressure drop in the water bank
P(N) = log(re./r(m(N)))*muw;
% dimensionless pressure calculation
PD = sum(P)/(muw*log(re/rw));
end

```

Function III: Dimensionless Pressure Estimation for SAG Injection (Discrete Surfactant Slug Size)

```

function [ PD ] = F3(tD,krwe,nw,krge,ng,swr,sgr,fmmob,fmdry,epdry,rw,re,xDf,rf,tDf,j)
mug = 2e-5;
muw = 1e-3;
swe = @(sw) (sw-swr)/(1-swr-sgr); % effective water saturation
krw = @(sw) (krwe*swe(sw).^nw); % water relative permeability
lambda_w = @(sw) (krw(sw)./muw); % water relative mobility
krg = @(sw) (krge*(1-swe(sw)).^ng); % gas relative permeability
lambda_g = @(sw) (krg(sw)./mug); % gas relative mobility
% foam Mobility Reduction Factor (STARS Model)
FM = @(sw) (1+fmmob*(0.5+ atan(epdry.*(sw-fmdry))/pi()));
% foam Mobility Reduction Factor (N.Z.et al. Model)
% FM = @(sw) (1+fmmob*((0.5+ atan(epdry.*(sw-fmdry))/pi())-(0.5+ atan(epdry.*(swr-fmdry))/pi())));
krgf = @(sw) (krg(sw)./FM(sw)); % foam relative permeability
lambda_f = @(sw) (real(krgf(sw)./mug)); % foam relative mobility
% fractional Flow of Water during SAG
fw = @(sw) (1./(1+(lambda_f(sw))./(lambda_w(sw))));
% fractional Flow of Water during Gas Injection
fw2 = @(sw) (1./(1+(lambda_g(sw))./(lambda_w(sw))));
% derivative of water relative permeability
dkrw = @(sw) ((nw*krwe*swe(sw).^(nw-1))./(1-swr-sgr));
% derivative of water relative mobility
dlambda_w = @(sw) (real(dkrw(sw)./muw));
% derivative of gas relative permeability

```

```

dkrg = @(sw) (-(krge*ng*(1-swe(sw)).^(ng-1))./(1-swr-sgr));
% derivative of gas relative mobility
dlambda_g = @(sw) (dkrg(sw)./mug);
% derivative of foam mobility reduction factor
dFM = @(sw) ((fmmob*epdry)./(pi*(1+(epdry^2*(sw-fmdry).^2))));
% derivative of foam relative permeability
dkrgf = @(sw) ((dkrg(sw).*FM(sw)-dFM(sw).*krge(sw))./FM(sw).^2);
% derivative of foam relative mobility
dlambda_f = @(sw) (dkrgf(sw)./mug);
% derivative of the fractional flow curve for foam (dfw,f/dSw)
dfw = @(sw) ((lambda_f(sw).*dlambda_w(sw) -
dlambda_f(sw).*lambda_w(sw))./(lambda_f(sw)+lambda_w(sw)).^2);
% derivative of the fractional flow curve for gas (dfw,g/dSw)
dfw2 = @(sw) ((lambda_g(sw).*dlambda_w(sw) -
lambda_w(sw).*dlambda_g(sw))./(lambda_g(sw)+lambda_w(sw)).^2);
% total relative mobility for SAG injection
lambda_rt = @(sw) (lambda_w(sw)+lambda_f(sw));
% total relative mobility for gas injection
lambda_rt2 = @(sw) (lambda_w(sw)+lambda_g(sw));
% determination of the shock saturations
F = @(sw) (fw(sw) + dfw(sw) .* (1-sw)-1);
F2 = @(sw) (fw2(sw)+ dfw2(sw) .* (1-sw)-1);
% water saturation at the shock SAG injection
sw_shock = fzero(F, [swr+eps,0.6]);
% water saturation at the shock gas injection
sw_shock2 = fzero(F2, [swr+eps, 1-sgr-0.001]);
% range of water saturation experienced for SAG injection
m = linspace(swr,sw_shock(j),201);
N = length (m);
% range of water saturation experienced for gas injection
m2 = linspace(swr,sw_shock2(j),201);
N2 = length (m);
i=1;
% dimensionless position SAG
xD = @(sw) (min(tD.*dfw(sw),xDf));
% radial position SAG
r = @(sw) (sqrt(xD(sw).*(re^2-rw^2)+rw^2));
% dimensionless position gas injection
xD2 = @(sw) (min(xDf+(tD-tDf).*dfw2(sw),1));
% radial position gas injection
r2 = @(sw) (sqrt(xD2(sw).*((re-rf)^2-rw^2)+rw^2));
xD = @(sw) (min(tD.*dfw(sw),1)); %Dimensionless position of the shock
rr = @(sw) (sqrt(xDD(sw).*(re^2-rw^2)+rw^2)); % Radius of the shock
R = rr(sw_shock(j)); %Radius of the shock

```

```

if R<=rf
    % Pressure Drop in the foam bank
    P(i:N-1) = log(r(m(i+1:N))./r(m(i:N-1)))
    .* (0.5*(1./lambda_rt(m(i+1:N))+1./lambda_rt(m(i:N-1))));
    P(N) = log(re./r(m(N)))*muw;% Pressure drop in the water bank
    PD = sum(P)/(muw*log(re/rw)); % dimensionless pressure calculation
else
    % Pressure Drop in the foam bank
    P(i:N-1) = log(r(m(i+1:N))./r(m(i:N-1)))
    .* (0.5*(1./lambda_rt(m(i+1:N))+1./lambda_rt(m(i:N-1))));
    % Pressure drop in the gas bank
    P2(i:N2-1) = log(r2(m2(i+1:N2))./r2(m2(i:N2-1)))
    .* (0.5*(1./lambda_rt2(m2(i+1:N2))+1./lambda_rt2(m2(i:N2-1))));
    % Pressure drop in the water bank
    P2(N2) = log((re)./(r2(m2(N2))))*muw;
    % dimensionless pressure calculation
    PD = (sum(P)+sum(P2))/(muw*log(re/rw));
end
end

```

Main File (Driver)

```

close all
clear all
clc

Layer = {'Bentheimer', 'Berea', 'Sister Berea', 'Bandera'};
%% Corey Model Paramters
krwe = [0.39 0.39 0.14 1];
nw = [2.86 4.09 5.25 3.56];
krge = [0.59 0.99 0.47 0.73];
ng = [0.7 1.97 1.22 2.43];
%% Petrophysical Model Parameters
swr = [0.25 0.23 0.25 0.46];
sgr = [0.2 0.12 0.25 0];
phi = [0.24 0.20 0.21 0.23];
k = [1900e-15 90e-15 160e-15 6e-15];
%% Foam Model Parameters
fmmob = [4.77e4 8.69e5 3.07e4 6.82e4];
fmdry = [0.271 0.336 0.396 0.549];
epdry = [4.0e2 1.96e4 8.89e3 1.52e2];
%% Fluid Property Parameters
muw = 1e-3; % water viscosity
mug = 2e-5; % gas viscosity
%% Inner and Outer Radii

```



```

rw = 0.1; % Wellbore radius [m]
re = 100; % Reservoir outer radius [m]
%% Height Calculation
h      = phi(1)./phi;
kh     = k.*h;
%% Pore Volume Calculation
PV = pi()*phi.*h.*(re^2-rw^2); % Pore Volumes of all layers
PVt = sum(PV); % Total Pore Volume
%% calculate the fraction of pore volumes to the total 'reservoir' pore volume (Fi)
F1 = (h(1)*phi(1))/(h(1)*phi(1)+h(2)*phi(2)+h(3)*phi(3)+h(4)*phi(4));
F2 = (h(2)*phi(2))/(h(1)*phi(1)+h(2)*phi(2)+h(3)*phi(3)+h(4)*phi(4));
F3 = (h(3)*phi(3))/(h(1)*phi(1)+h(2)*phi(2)+h(3)*phi(3)+h(4)*phi(4));
F4 = (h(4)*phi(4))/(h(1)*phi(1)+h(2)*phi(2)+h(3)*phi(3)+h(4)*phi(4));
%% Define Simulation Time and Surfactant Slug Sizes
V = logspace(-8,1,10); % Relative Volume of Surfactant Slugs
TD = logspace(-8,1,1e5); % Define the time
dTD = diff(TD); % Define the Time increments
TDplot = cumsum(dTD); % the cumulative sum of time increments
%% Pre-allocation of the calculated parameters
%Dimensionless Pressure
PD1 = zeros (length(V),length(dTD));
PD2 = zeros (length(V),length(dTD));
PD3 = zeros (length(V),length(dTD));
PD4 = zeros (length(V),length(dTD));
PDtot = zeros(length(V), length(TD)-1); % total dimensionless Pressure
% Dimensionless Time
tD1 = zeros (length(V),length(dTD));
tD2 = zeros (length(V),length(dTD));
tD3 = zeros (length(V),length(dTD));
tD4 = zeros (length(V),length(dTD));
v = zeros (length(V),length(krwe)); % volume of surfactant slug into each layer
rf = zeros (length(V),length(krwe)); % radius of the foam bank into each layer
rs = zeros (length(V),length(krwe)); % radius of the surfactant bank
xDf = zeros (length(V),length(krwe)); % dimensionless position of the foam bank
tDf = zeros (length(V),length(krwe)); % dimensionless time of the foam bank
%% Initializing Dimensionless Pressure (I.C.)
PD1(:,1)=1; PD2(:,1)=1; PD3(:,1)=1; PD4(:,1)=1;
%% Calculating the Dimensionless Time at (I.C.)
tD1(:,1)=
(kh(1)./PD1(1,1))./(kh(1)./PD1(1,1)+kh(2)./PD2(1,1)+kh(3)./PD3(1,1)+kh(4)/PD4(1,1))*(dT
D(1)/F1);
tD2(:,1)=
(kh(2)./PD2(1,1))./(kh(1)./PD1(1,1)+kh(2)./PD2(1,1)+kh(3)./PD3(1,1)+kh(4)/PD4(1,1))*(dT
D(1)/F2);

```

```

tD3(:,1)=
(kh(3)./PD3(1,1))./(kh(1)./PD1(1,1)+kh(2)./PD2(1,1)+kh(3)./PD3(1,1)+kh(4)/PD4(1,1))*(dT
D(1)/F3);
tD4(:,1)=
(kh(4)./PD4(1,1))./(kh(1)./PD1(1,1)+kh(2)./PD2(1,1)+kh(3)./PD3(1,1)+kh(4)/PD4(1,1))*(dT
D(1)/F4);

%% Calculatio for the various parameters for each relative volume of the surfactant
slug
for i= 1:length(V);
    v(i,:) = [kh(1)/sum(kh) kh(2)/sum(kh) kh(3)/sum(kh) kh(4)/sum(kh)]*V(i)*PVt;
    rs(i,:) = sqrt(v(i,)./(pi()*phi.*h)+rw^2);
    rf(i,:) = sqrt(v(i,)./(pi()*phi.*h.*fmdry)+rw^2);
    xDf(i,:) = ((sqrt(v(i,)./(pi()*phi.*h.*fmdry)+rw^2)).^2-rw^2)/(re^2-rw^2);
end
rs(rs > re) = re; % Maximum radius of the surfactant bank
rf(rf > re) = re; % Maximum radius of the foam bank
xDf(xDf > 1) = 1; % Maximum Dimesnionless Position

for i= 1:length(V);
    tDf(i,:) = (rf(i,).^2-rw^2)./(re^2-rw^2).*(1-fmdry); %dimensionless time of the
foam bank calculation
end
% Dimensionless Pressure and time calculation
for i =1:length(V)
    for t= 1:length(dTD)-1
        [ PD1(i,t+1) ] =
F3(tD1(i,t),krwe(1),nw(1),krge(1),ng(1),swr(1),sgr(1),fmmob(1),fmdry(1),epdry(1),rw,re,
xDf(i,1),rf(i,1),tDf(i,1),1);
        [ PD2(i,t+1) ] =
F3(tD2(i,t),krwe(2),nw(2),krge(2),ng(2),swr(2),sgr(2),fmmob(2),fmdry(2),epdry(2),rw,re,
xDf(i,2),rf(i,2),tDf(i,2),2);
        [ PD3(i,t+1) ] =
F3(tD3(i,t),krwe(3),nw(3),krge(3),ng(3),swr(3),sgr(3),fmmob(3),fmdry(3),epdry(3),rw,re,
xDf(i,3),rf(i,3),tDf(i,3),3);
        [ PD4(i,t+1) ] =
F3(tD4(i,t),krwe(4),nw(4),krge(4),ng(4),swr(4),sgr(4),fmmob(4),fmdry(4),epdry(4),rw,re,
xDf(i,4),rf(i,4),tDf(i,4),4);
        tD1(i,t+1)=
(kh(1)./PD1(i,t+1))./(kh(1)./PD1(i,t+1)+kh(2)./PD2(i,t+1)+kh(3)./PD3(i,t+1)+kh(4)/PD4(i
,t+1))*(dTD(t+1)/F1)+tD1(i,t);
        tD2(i,t+1)=
(kh(2)./PD2(i,t+1))./(kh(1)./PD1(i,t+1)+kh(2)./PD2(i,t+1)+kh(3)./PD3(i,t+1)+kh(4)/PD4(i
,t+1))*(dTD(t+1)/F2)+tD2(i,t);
        tD3(i,t+1)=
(kh(3)./PD3(i,t+1))./(kh(1)./PD1(i,t+1)+kh(2)./PD2(i,t+1)+kh(3)./PD3(i,t+1)+kh(4)/PD4(i
,t+1))*(dTD(t+1)/F3)+tD3(i,t);
        tD4(i,t+1)=
(kh(4)./PD4(i,t+1))./(kh(1)./PD1(i,t+1)+kh(2)./PD2(i,t+1)+kh(3)./PD3(i,t+1)+kh(4)/PD4(i
,t+1))*(dTD(t+1)/F4)+tD4(i,t);

```

```

    end
end

% Flow Ratio Calculation
for i=1:length(V)
    R1(i,:)=tD1(i,:)./(tD1(i,:)+tD2(i,:)+tD3(i,:)+tD4(i,:));
    R2(i,:)=tD2(i,:)./(tD1(i,:)+tD2(i,:)+tD3(i,:)+tD4(i,:));
    R3(i,:)=tD3(i,:)./(tD1(i,:)+tD2(i,:)+tD3(i,:)+tD4(i,:));
    R4(i,:)=tD4(i,:)./(tD1(i,:)+tD2(i,:)+tD3(i,:)+tD4(i,:));
end

% Total Dimensionless Pressure calculation
for i=1:length(V)
    PDtot(i,:)=
sum(kh)./(kh(1)./PD1(i,:)+kh(2)./PD2(i,:)+kh(3)./PD3(i,:)+kh(4)./PD4(i,:));
end

% Relative time calculation
for i=1:length(V)
    I(i,:) = PDtot(i, :).*dTD;
    RT(i,:) = cumsum(I(i, :));
end

```